Effects of membrane shape and lipid composition in extracellular vesicle and platelet biology

by

Noah Kastelowitz-Lieberman

B.A., University of Utah, 2010

A thesis submitted to the

Faculty of the Graduate School of the

University of Colorado in partial fulfillment

of the requirement for the degree of

Doctor of Philosophy

Department of Chemistry and Biochemistry

2016

This thesis entitled:
Effects of membrane shape and lipid composition in extracellular vesicle and platelet biology
written by Noah Kastelowitz-Lieberman
has been approved for the Department of Chemistry and Biochemistry

_____
Prof. Hang Yin

_____
Prof. Amy Palmer

Date_____

The final copy of this thesis has been examined by the signatories, and we find that both the content and the form meet acceptable presentation standards of scholarly work in the above mentioned discipline.

Kastelowitz-Lieberman, Noah (Ph.D., Biochemistry)

Effects of membrane shape and lipid composition in extracellular vesicle and platelet biology

Thesis directed by Prof. Hang Yin

In this work, I examine the importance of fundamental properties of lipid membranes, such as membrane curvature or lipid composition, in the context of extracellular vesicle and platelet biology. Although differing in biologic function, both extracellular vesicles and platelets are comparatively small in size, anucleate, and expose phosphatidylserine on their outer membrane leaflet. Phosphatidylserine is an anionic lipid that is generally sequestered to the inner leaflet of bilayer membranes. The exposure of phosphatidylserine on the outer membrane leaflet of extracellular vesicles appears necessary for their signaling, and the exposure of phosphatidylserine on platelets facilitates the assembly of enzymatically active coagulation protein complexes. I first highlight the basic biology of extracellular vesicles and address biochemical and biophysical detection methods that depend on the lipid composition and particle size of the extracellular vesicles. Next, I use all-atom molecular dynamics simulations to show that increasing the lateral density of lipids can induce a bilayer membrane to form a curved shape. These membranes provide a model system for studying interactions in curved membranes, as well as demonstrate that curved membranes display an increased number of lipid packing defects. Next, I adapt theoretical models of membrane-membrane interactions to examine the interaction energies between extracellular vesicles and cells. These estimates show that smaller vesicles such as

exosomes are more likely to signal via endocytosis, while larger vesicles like microvesicles are more likely to signal via receptor-ligand interactions. Finally, I examine the effects of phosphatidylserine-targeting peptides on the platelet procoagulant response. I show that these peptides can compete with coagulation factors for phosphatidylserine binding sites and target phosphatidylserine exposed on activated platelets *in vitro* and *in vivo*. Together, this work supports a broader understanding of how membrane shape and lipid composition influences, and is a potential target for modulation of, the biology of extracellular vesicles and platelets.

Dedication

To Emily for who is to come.

To my Parents for their boundless support.

Acknowledgements

A major theme of my thesis is collaboration; across disciplines and institutions. I would not have been to able undertake these projects without the support of my advisor, Prof. Hubert Yin. Thank you Hubert, for providing an environment of guidance and intellectual freedom that allowed me to undertake a variety of projects, and provided an excellent training experience. Thank you to Prof. Jorge Di Paola, for the tireless support of my research and career development. Thank you to Dr. Deanne Sammond, I learned a great deal from your training, collaboration, and enthusiasm for science. To my thesis committee members, Profs. Natalie Ahn, Arthur Gutierrez-Hartmann, Karolin Luger, and Amy Palmer, thank you for your direction, feedback, and encouragement. I am grateful to have worked with Kim Kelly, and thank her and Pamela Williamson for navigating me through the requirements of graduate school. Thank you to everyone in the CU Medical Scientist Training Program for the support and advice throughout my training. To all the past and present members of the Yin group, thank you for the friendship, discussion, and levity. Things that seemed trivial, like puzzles, dog food jelly beans, football, and competitions of athletic prowess, among others, were absolutely important. Thank you also to all the members of the Di Paola lab for the collaboration and friendship. To my parents and all of my family, thank you for supporting my long journey as a student. To Emily, thank you for continuing to teach me the many meanings of strength.

Contents

Chapters

Tables

Figures

Chapter 1

Introduction and background - Exosomes and microvesicles: identification and targeting by particle size and lipid chemical probes

This chapter has been published as Kastelowitz, N. & Yin, H. Exosomes and Microvesicles: Identification and Targeting By Particle Size and Lipid Chemical Probes. *Chembiochem* **15**, 923–928 (2014).

1.1 Introduction

1.1.1 Ferrying cargo with extracellular vesicles

Microvesicles and exosomes, collectively referred to as extracellular vesicles in this review, are submicron sized lipid containers released by cells. Both types of extracellular vesicles have an aqueous, cargo-containing core surrounded by a roughly spherical bilayer membrane. Arrival of the vesicles at a distant site and fusion with targeted cells allows transport of cargo as diverse as nucleic acids (DNA, mRNA, and microRNA), proteins, and lipids, facilitating important cell-cell communications.[1,2] Packaging the cargo in lipid vesicles protects the contents from extracellular degradation and allows for more precise targeting of the contents.[1,3] Packaging also

provides temporal signaling control through the simultaneous delivery of an array of signaling molecules. Binding of vesicles to target cells is a specific interaction that is likely dependent on receptor mediated association, e.g., microvesicles originating from platelets interact with monocytes but not neutrophils.[4,5] A recent increase in understanding of the role extracellular vesicles play in normal, and pathologic, intercellular communication processes has made them a topic of intense interest.[6-11] The list of normal physiologic roles for microvesicles and exosomes continues to grow: microvesicles and exosomes have already been implicated in horizontal genetic transfer, cytokine release, angiogenesis, transfer of receptors between cells, and metalloproteinase release.[4]

1.1.2 Extracellular vesicle release, lipid composition, and shape

Although microvesicles and exosomes are structurally similar, they differ in cellular origin, lipid composition, and size. At present, precise definitions of the distinctions and the terminology used to describe these extracellular vesicles are still developing.[12] For example, the hematology research community often uses the term microparticles instead of microvesicles.[13,14] In general, microvesicles are described as being formed by outward budding and fission of the plasma membrane, and as having a particle diameter of 100 – 1000 nm.[15] The lipid composition of microvesicles is by and large similar to that of the cell membrane, but lacks the asymmetric distribution of lipids normally seen across the two leaflets of the plasma membrane. In particular, the aminophospholipids, phosphatidyl-serine and -ethanolamine, are no longer sequestered

to the inner leaflet of the membrane, and are instead homogenously distributed across the microvesicle bilayer membrane.[16,17]

Unlike microvesicles, exosomes are produced within the cell and are released through an exocytosis event. Exosome production begins when the bilayer membrane of late endosomes buds inward, filling the luminal space of the endosome with small luminal vesicles or exosomes.[18,19] The vesicle filled endosome, now called a multivesicular body (MVB), then fuses with the plasma membrane through a calcium dependent mechanism, releasing the exosomes into the extracellular space (Fig. 1.1).[20] Similar to microvesicles, exosome membranes also contain an increased level of aminophospholipids compared to the outer leaflet of the plasma membrane.[21] In addition, exosome membranes also contain the lipid ceramide. Ceramide is produced by the hydrolysis of sphingomyelin by sphingomyelinases within the endosome, and its production is an essential step in the sorting and production of exosomes.[22] Exosomes are smaller and more homogenously distributed in size than microvesicles, commonly being described as having a particle diameter of 30 – 100 nm.[22,23] When prepared for and viewed with an electron microscope, exosomes typically display a cup-like shape.[24]

A significant feature of extracellular vesicles is their highly curved membrane surface. Highly curved membrane shapes, where curvature is defined as the reciprocal of the membrane radius, are commonly found within cells.[25] These membranes organize and compartmentalize organelles of complex shape such as the Golgi, and are the cargo of intracellular motor proteins like kinesin. In the extracellular space, highly curved membranes are less common. As most cells have diameters > 8 μm, submicron sized extracellular vesicles represent uniquely curved lipid surfaces.[10] Curvature affects

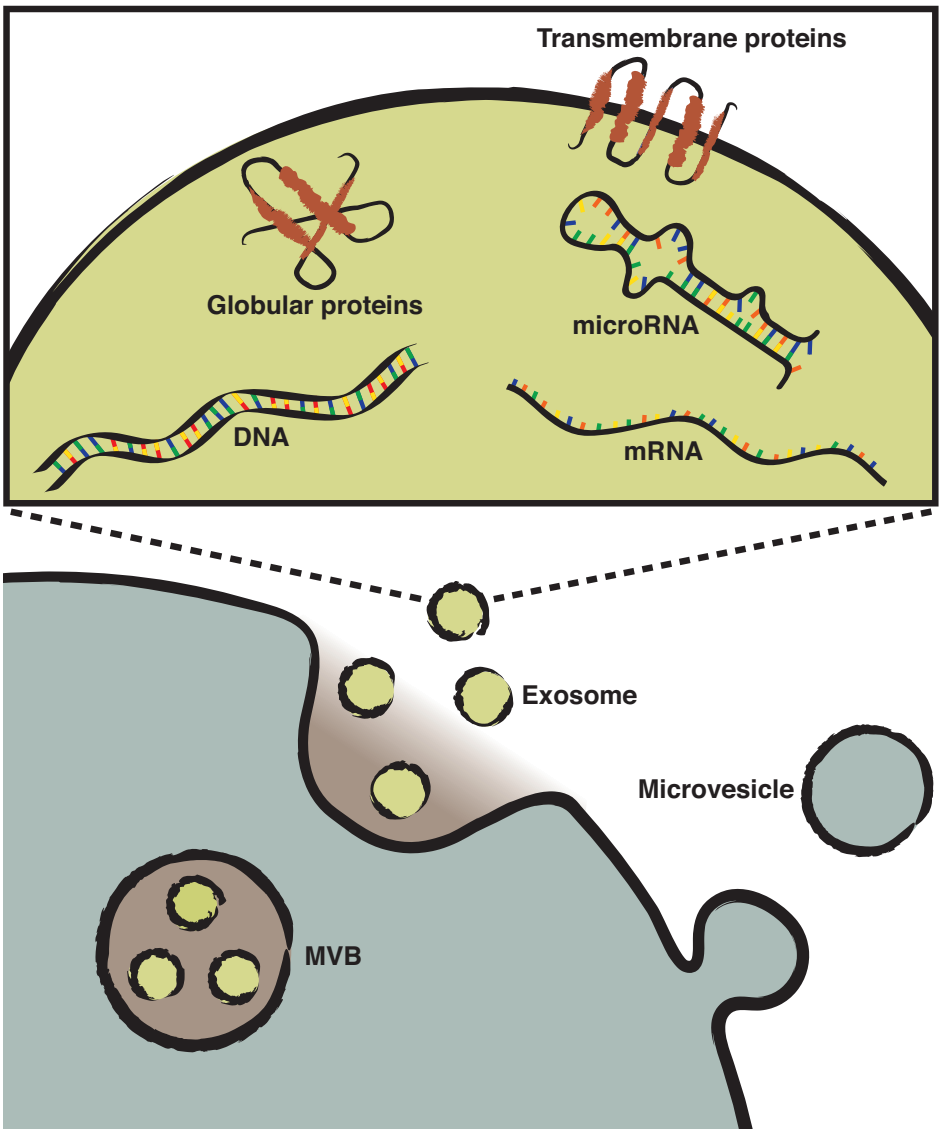

Figure 1.1. Extracellular vesicle release and contents. Microvesicles bud directly from the plasma membrane. Exosomes, formed by inward budding of late endosomes, are held in multivesicular bodies (MVB) within the cell. Fusion of the MVBs with the cell membrane releases the exosomes into the extracellular space. Microvesicles and exosomes contain a diverse array of cargo, including lipids, transmembrane and globular proteins, DNA, mRNA, and microRNA. All represented membranes are phospholipid bilayers.

lipid ordering within the membrane. Mismatch between the curvature of the membrane and the shape, or spontaneous curvature, of the lipids induces lipid-packing defects.[26-28] The holes created by the lipid-packing defects expose the hydrophobic core of the bilayer membrane to the aqueous phase (Fig. 1.2). The defects are short-lived, but result in a net reduction of lipid density in the curved region. Along with absolute size, these membrane-packing defects are a characteristic feature of exosomes and microvesicles in the extracellular space, and one that will be further explored as a targetable or detectable feature in this review.

1.1.3 Extracellular vesicles promote cancer progression

Cancer cells have long been known to gain a competitive advantage by releasing factors that modulate the extracellular environment to promote cancer growth and metastasis. There is growing evidence that these factors are released via extracellular vesicles. Cultured glioblastoma multiforme, melanoma, and breast cancer cells have all shown significantly elevated release of microvesicles or exosomes.[29,30] Exosomes released from melanoma cells have been shown to promote angiogenesis, matrix remodeling, and anergy in lymph nodes, creating an optimal environment for metastatic cancer cells.[31] Colorectal cancer cells have been shown to shed Fas ligand laden vesicles that reduce the ability of T-cells to induce cancer cell apoptosis.[32]

Increased microvesicle and exosome levels have also been found in the blood of cancer patients. Elevated levels of microRNA-containing microvesicles have been found in the serum of patients with prostate cancer, and increased exosome levels were found in the plasma of patients with lung adenocarcinoma and melanoma.[33-35] Higher levels of

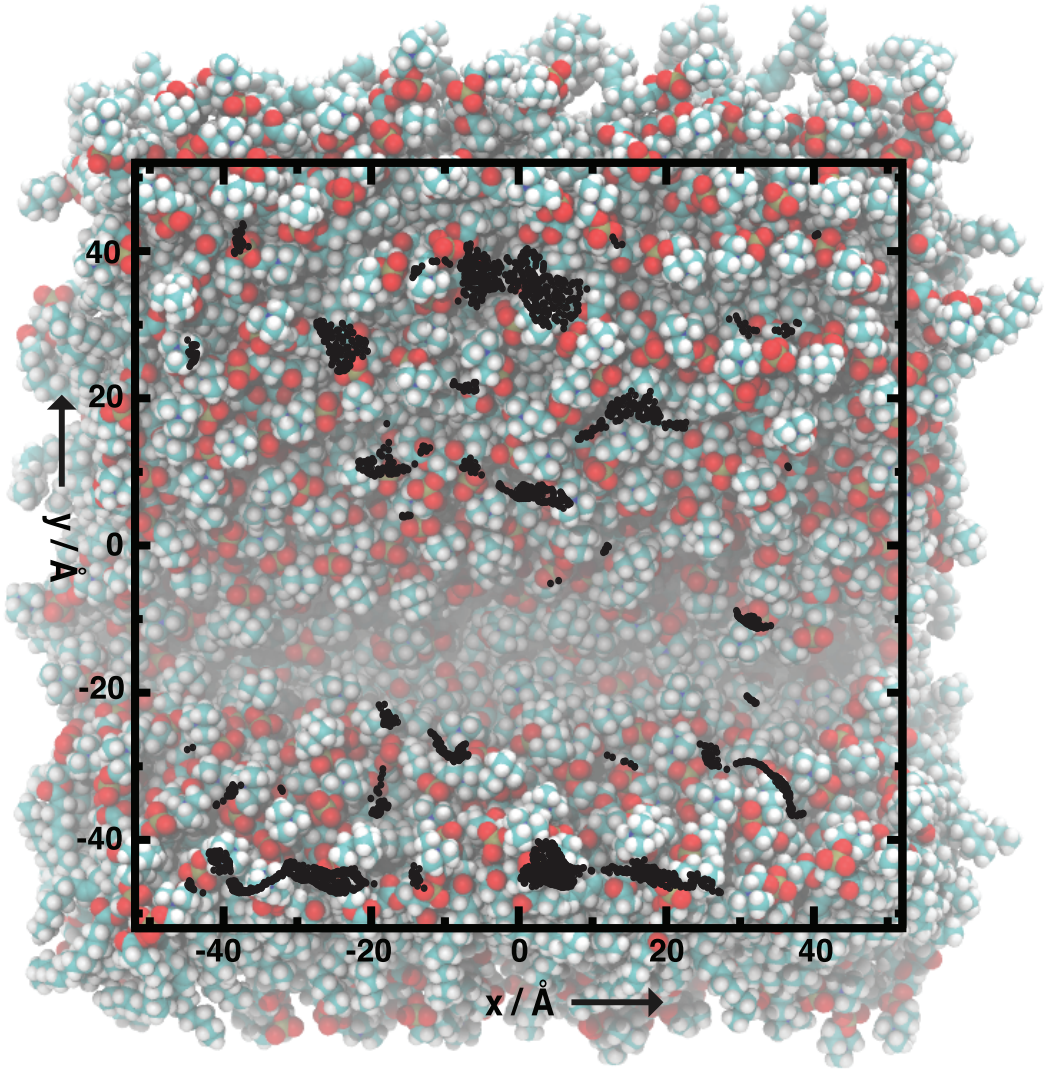

Figure 1.2. Membrane curvature induces lipid-packing defects in regions of positive curvature. Top view of a 1-palmitoyl-2-oleoyl-*sn-glycero*-3-phosphatidylcholine (POPC) bilayer membrane induced to curve by gradual lateral compression during molecular dynamics simulation. Lipid packing defects, as measured by solvent accessible surface area, are mapped to the surface as black dots. Lipid head groups are shown in orange and red, and hydrocarbon tails in white and blue. The region of negative curvature, in the area of $y \approx -20$, shows few packing defects. Figure adapted with permission.[27]

circulating vesicles have also been correlated with a poorer prognosis in patients with gastric cancer.[36] Increasing evidence of the role of extracellular vesicles in the progression of cancer suggests that methods to detect, quantify, and modulate exosomes and microvesicles may potentially have prognostic, diagnostic, and therapeutic value. With this goal in mind, we discuss here current methods used to detect and target extracellular vesicles, and address the applicability of the emerging field of membrane curvature and lipid sensing peptides to this function.

1.2 Sensing the submicroscopic

1.2.1 Methods for detecting extracellular vesicles

Widely applied technologies used for detection of ultramicroscopic particles like exosomes and microvesicles include electron microscopy, flow cytometry, dynamic light scattering (DLS), and nanoparticle tracking analysis (NTA). Depending on the method used, the reported absolute number of extracellular vesicles in a liter of blood can vary by as much as five orders of magnitude.[37]

Each method mentioned above has advantages and drawbacks when used to detect extracellular vesicles. Electron microscopy can directly show that vesicles exist in a sample, but cannot provide quantitative data, and the fixation process can alter vesicle shape and size.[38] Flow cytometry is typically limited to the identification of particles greater than 300 nm, preventing the detection of smaller microvesicles and all exosomes.[39] Recently developed flow cytometry protocols have lowered this limit, but the detection of sub 100 nm particles, like exosomes, still remains an outstanding problem.[40] Challenges of detecting extracellular vesicles with DLS include: 1) the low

refractive index of vesicles, and 2) a bias towards detection of larger particles when used with heterogeneous solutions.[38] This makes it problematic to distinguish between microvesicles (>100 nm) and exosomes (<100 nm) in mixed solution.[41] NTA is perhaps the most promising method because it can identify both microvesicles and exosomes and is not dependent on the refractive index of the vesicles. However, without a fluorescently labeled antibody directed towards a vesicle surface marker, or without use of a vesicle isolation method to reduce polydispersity of the sample, there can be considerable intra-assay count variability.[38,42]

1.2.2 Brownian motion of extracellular vesicles

Both DLS and NTA rely on the relationship between particle size and diffusion coefficient to determine the size of the extracellular vesicles in solution. This is described quantitatively for a spherical particle in a low Reynolds number fluid by the Stokes-Einstein equation

$$D = \frac{k_B T}{6\pi\eta r}$$

where D is the diffusion coefficient, k_B is Boltzmann's constant, T is the temperature, η is viscosity of the fluid, and r is the radius of the particle. The estimated diffusion coefficients for microvesicles and exosomes in the extracellular environment are shown in Fig. 1.3A. It is important to note that the relative differences in the diffusion coefficient between different vesicle sizes becomes more difficult to resolve as the vesicles become larger. For example, going from a vesicle 30 nm in diameter to 130 nm in diameter changes the diffusion coefficient by ~12 $\mu m^2/s$, but from 900 nm to 1000 nm the diffusion coefficient changes by only ~0.05 $\mu m^2/s$. For experiments using NTA, it is

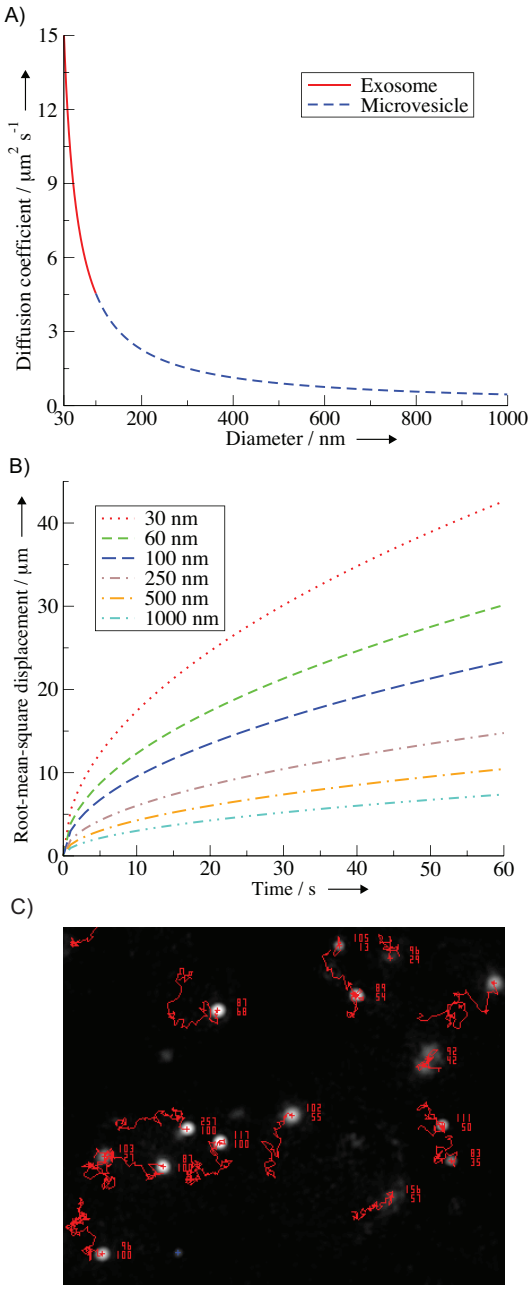

Figure 1.3. Extracellular vesicle size dependent diffusion and displacement. **A**) Diffusion coefficients of exosomes (solid red) and microvesicles (dashed blue) as given by the Stokes-Einstein equation. **B**) Root-mean-square displacement of exosomes (dashed only lines) and microvesicles (dashed with dotted lines) through an aqueous extracellular environment. **C**) Representative image of ~100 nm particles visualized using a NTA instrument (NanoSight LM14). Red lines are the diffusional displacement of the particles tracked by the NTA software. Each particle is associated with two numbers, the upper number represents the particle size as calculated using the Stokes-Einstein equation and the lower number represents the particle's track length.

therefore important to consider if the minimum track length (how long a particle must be followed before the diffusion coefficient is calculated) is long enough to properly resolve such differences in vesicle diffusion coefficients. In general, and depending on the settings of the NTA instrument, particles with diameters in the range of 1 μm or greater move too slowly to be accurately sized using NTA.[38]

The calculated diffusion coefficients can also be used to estimate the average distance a vesicle diffuses from its origin in a given time. The root-mean-square displacement (x_{rms}) for diffusion in the absence of an external force is given by

$$x_{rms} = \sqrt{2Dt}$$

where t is time.[43] The behavior and presence of exosomes and microvesicles is arguably best studied in blood.[44] Vesicles in the blood are subjected to large external forces from the pulsatile flow of the circulation system that trump in scale any diffusive processes. Cases of smaller external forces, where we can make the approximation of using the root-mean-square displacement equation, do exist, such as paracrine signaling between nearby cells or in the sample chamber of an NTA instrument (Fig. 1.3C). For these cases, Fig. 1.3B illustrates that smaller exosomes are able to diffuse greater distances in a given time, making them the faster traveling and equilibrating vesicle.

1.2.3 Protein markers of extracellular vesicles

Up to this point, we have focused on identifiable biophysical characteristics of extracellular vesicles. In addition to fundamental properties such as diffusion coefficient, exosomes and microvesicles also display surface markers that can be used for

quantification and detection. The distinction between markers specific to exosomes or microvesicles is muddled by variations in literature terminology previously mentioned, and challenges isolating and identifying the separate populations of vesicles. Universal markers commonly used to identify exosomes are better characterized, and include transmembrane proteins like tetraspanins (CD9, CD63, CD81, and CD82) and MHC class I and II, and cytosolic proteins like heat shock proteins (HSP-70 and HSP-90).[18,45,46] Source specific markers that represent the proteome of the cell of origin can also be used for exosome identification. For example, urinary exosomes of patient's with non-small cell lung cancer were found to carry proteins representative of their primary tumor.[47]

Detection of extracellular vesicle proteins is relatively straight forward using analytical techniques like western blot or ELISA. However, soluble antigens may also be detected, and it is not possible to distinguish vesicle sizes or concentrations with these techniques.[38] Additionally, interindividual differences in exosome tetraspanin expression levels, in particular CD63, may reduce the value of comparative studies.[48]

1.2.4 Targeting extracellular vesicle lipids

The final component of the extracellular vesicle surface is the bilayer lipid membrane. As discussed earlier, the membranes of exosomes and microvesicles both contain rare lipids (e.g. ceramide and aminophospholipids) and have highly curved surfaces that contain lipid-packing defects. In the extracellular environment, these are unique traits that can be targeted by membrane binding proteins. Here we will briefly discuss these proteins and their applications to extracellular vesicle detection. For a

broader and more comprehensive summary of membrane binding proteins, see these other excellent reviews.[49-51]

Membrane binding proteins encompass a variety of proteins, from random coils to those with complex secondary structures. Compared to a protein-protein binding interface that can have complex three-dimensional tertiary and quaternary structure, the membrane-protein interface can be thought of as planar regions of discrete interaction regimes: the hydrophobic core, the electrostatically charged phosphate and lipid head groups, and the hydrophilic solvent. Three interaction regime regions, and two interfaces between them, leave open the possibility for many membrane recognition mechanisms.

The most conventional protein-membrane interaction mechanism is the recognition of rare lipid head groups by a folded protein domain in a lock and key like mechanism.[50,52] A well known example is annexin V, which recognizes the lipid phosphatidylserine using folded domain repeats that bind the lipid head group through coordinated Ca^{2+} ions.[52] Membrane binding through coordinated divalent cations, Ca^{2+} or Zn^{2+}, is a common mechanism for folded protein domains.[52] Among the lipids found in the extracellular environment, phosphatidylserine carries an uncommon net negative charge. Although most other lipids have ionic character, they are zwitterionic and do not have a net charge.[21] Fluorescently labeled annexin V is commonly used to detect the exposure of phosphatidylserine on the outer membrane leaflet of apoptotic cells.[53] As discussed earlier, extracellular vesicles also contain phosphatidylserine in their outer membrane leaflet. Annexin V has been used in methods to quantify exosome and microvesicle phosphatidylserine levels, for a filtration and flow cytometry based

microvesicle counting assay, and to inhibit exosome signaling by blocking exosome-cell membrane fusion.[18,54,55]

1.2.5 Probes for extracellular vesicle membrane curvature

The next examples include proteins that can sense membrane curvature. Membrane curvature sensors are proteins that bind the membrane with varying affinity based on the membrane's shape. Curvature sensing occurs through many motifs, including, but not limited too: electrostatic interaction with clustered anionic lipids, well structured protein-membrane shape matching, insertion of hydrophobic residues or loops into membrane defects, and curved membrane induced protein folding.[49,51] Proteins/peptides can also actively induce membrane curvature, altering the shape of the membrane. The distinction between a protein that induces membrane curvature and one that senses it is likely as dependent on the concentration of the protein as it is on its physical properties.[50] The outer membrane of extracellular vesicles is positively curved, or convex, so we focus here on examples of sensors for these surfaces.

Three recent cases show how truncation or structural modification of a known membrane binding protein can lead to a curvature sensing peptide. Myristoylated alanine-rich C kinase substrate (MARCKS) is an intracellular protein that normally functions to sequester free PIP_2 lipids on the interior leaflet of the plasma membrane.[56] In its active form, the lysine rich effector domain of MARCKS binds PIP_2 through a non-specific electrostatic interaction.[56] Truncation of MARCKS to just its effector domain results in a 25 amino acid unstructured peptide.[57] This peptide, MARCKS-ED, preferentially binds phosphatidylserine enriched and exosome sized (< 100 nm

diameter) synthetic liposomes and isolated extracellular vesicles.[57] Electrostatic attraction between positively charged peptide lysine residues and negatively charged phosphatidylserine lipid head groups, as well insertion of five bulky hydrophobic phenylalanine residues into lipid-packing defects, likely explains this behavior.[57] Phenylalanine insertion would be entropically favorable; it would exclude the solvent from the membrane defect and remove the need for a solvation shell to form around the hydrophobic peptide residues.

Another example, C2BL3C, is a 12 amino acid long peptide that was cyclized using “Click” chemistry.[58] The peptide is based on a Ca^{2+} dependent membrane inserting loop of the membrane fusion protein synaptotagmin-I. Truncation and cyclization of the membrane inserting loop created a more rigid peptide that selectively binds highly curved synthetic liposomes and blood derived exosomes in a calcium independent manner.[58] Although the mechanism of its curvature sensing remains unknown, the low net charge of C2BL3C suggests a lipid-packing defect stabilization mechanism.[58] The final modification example is a derivative of the cationic peptide bradykinin. In this case, a truncated bradykinin monomer showed modest curvature sensing; however, trimerization (conjugation of three monomers to a flexible linker backbone) significantly increased the peptides’ affinity for highly curved and charged surfaces.[59] A synergetic combination of electrostatic attraction and membrane structure scaffolding from the peptides’ claw-like shape may explain this curvature sensing behavior.[59]

These protein truncation, cyclization, and multimerization models illustrate how a simplified scaffold can maintain or gain new membrane curvature sensing properties

relevant to extracellular vesicle detection. Compared to annexin V, short, easily synthesized curvature sensing peptides such as these are advantageous because they allow for easier chemical modification, conjugation, and preparation. Future *in vivo* or *in vitro* applications will require consideration of the peptides' biological activity. For example, are the peptides present at concentrations sufficient to damage cells through induction of membrane curvature or other biological activity?

1.3 Outlook

In this review, we have touched on the basic biology of extracellular vesicles, their importance as a signaling entity in normal and pathologic processes, and addressed bio-physical and -chemical detection methods. Major barriers to our growing understanding of exosome and microvesicle biology include finding reliable methods for quantification, isolation, and modulation. Identifying universal characteristics of submicroscopic particles of heterogeneous origin and content is a challenging task. Outlined characteristics include lipid and protein composition and physical properties such as diffusion coefficient and membrane curvature. As physical properties represent a sum of the vesicle parts, they are arguably more universal. Membrane curvature sensing peptides are a unique class of molecules that can sense the physical state of the membrane. Along with the peptides mentioned, many potential future scaffolds exist for extracellular vesicle curvature sensing probes. These include naturally occurring proteins that sense, and in some cases induce, membrane curvature, such as the BAR domains, the ALPS motif of ArfGAP1, or α-synuclein.[60-63] The development of new tools for extracellular vesicle detection will help address basic questions, such as how

exosomes and microvesicles signal their target cells, and will also provide scaffolds for new biotechnological tools. Potential biomedical applications include quantifying circulating vesicles as a novel cancer biomarker and inhibiting the extracellular vesicle dependent signaling pathways that promote cancer growth and metastasis.

Chapter 2

Changes in lipid density induce membrane curvature

This chapter has been published as de Jesus, A. J.*, Kastelowitz, N*. & Yin, H. Changes in lipid density induce membrane curvature. *RSC Adv.* **3**, 13622 (2013). * These authors contributed equally to this work.

2.1 Abstract

Highly curved bilayer lipid membranes make up the shell of many intra- and extracellular compartments, including organelles and vesicles. Using all-atom molecular dynamics simulations, we show that increasing the density of lipids in the bilayer membrane can induce the membrane to form a curved shape.

2.2 Introduction

2.2.1 Membrane curvature within the cell

Membranes define the intra- from extracellular environment and compartmentalize the interior of the cell. Dynamic changes in membranes, such as budding, fission, and fusion, occur via alterations of membrane shape and curvature.

The shape of the membrane is driven by a combination of lipid composition, transmembrane and surface proteins, as well as forces from the cytoskeleton and extracellular matrix.[64-66] The molecular shape of the lipids in a membrane dictate the membrane's spontaneous curvature. For example, lysophospholipids, which have a large hydrophilic head group and small hydrophilic tail, form highly curved membrane structures.[67-69] In the cell, lipid flippases move lipids between the two leaflets of the bilayer, creating asymmetric distributions that can also cause the membrane to spontaneously form a curved shape.[26,64,70-74] The asymmetry between the two leaflets can be in absolute number of lipids or distributions of different lipid head groups.[65,67,69]

Both transmembrane and membrane surface proteins can induce a flat membrane to form more complex shapes.[26,70-75] The confinement of the cell membrane by a solid support, such as the extracellular matrix or cytoskeleton in the cell, restricts how the membrane can deform when subjected to perturbing forces.[65,76,77] The physical interplay between membrane and membrane protein is not unidirectional. For example, embedding a mechanosensitive transmembrane protein in a curved membrane can alter the structure of that protein.[10,75]

2.2.2 Membrane curvature in molecular simulations

Computational simulations provide a powerful tool to study membrane biophysics. The atomistic detail and temporal resolution available through simulations has made them a useful tool for investigating the dynamics of lipid membranes.[23,76,77] Membranes of different organelles and vesicles require different representations in simulations; *i.e.* lipid composition and membrane shape both need to be considered.

Most eukaryotic cells have diameters > 8 μm.[10,78] Typical computational simulations of the plasma membrane use a simulation box size on the scale of tens of nanometers and model the membrane as a planar surface with no defined curvature. This approximation is reasonable because on the scale that the membrane is being modeled, curvature does not have an appreciable effect on lipid organization or membrane shape. For example, a 100×100 nm^2 square plasma membrane represents only ~0.001% of the surface area of an 8 μm cell. Nonetheless, many membrane-bound compartments found either within or released by cells are submicroscopic in size. For example, exosomes—released into the extracellular environment by cells and thought to be mediators of intracellular communication—are highly curved vesicles 30 to 100 nm in diameter (curvature is defined as the reciprocal of the radius).[23,79] In this case, a 100×100 nm^2 membrane could represent as much as ~90% of an exosomal membrane surface area. In simulations modeling the bilayer membrane of submicroscopic particles such as exosomes, consideration of the effects of curvature on the shape of the membrane and lipid packing and ordering has the potential to more accurately represent the membrane and elucidate more biologically relevant lipid/protein interactions.

2.3 Results

2.3.1 Increased lipid density induces membrane curvature

Using molecular dynamics (MD) simulations, we describe here a method of inducing membrane curvature by increasing the density of lipids in a model bilayer membrane. The bilayer membrane was composed of 500 lipids (250 per leaflet) and

was a mixture of 1-palmitoyl-2-oleoyl-*sn*-glycero-3-phosphatidylcholine (POPC) and 1-palmitoyl-2-oleoyl-*sn*-glycero-3-phosphatidylserine (POPS). This lipid composition was chosen to approximately represent the charge distribution of a cellular membrane.[70,78,80] The POPS composition was varied between 0%, 5%, 10%, 15% and 20% of the total lipids. Variations in POPS concentration were introduced to explore whether changing the concentration of a negatively charged head group has an effect on the curvature of the model bilayers. Two independent simulations for each POPS concentration were performed. Initially, flat bilayers of these lipid mixtures were simulated using reported equilibrium lipid surface area values of POPC and POPS.[57,79] Curvature was induced by scaling the *x* and *y* coordinates of the system. The *z* coordinate was kept coupled to a pressure reservoir to maintain the pressure, which ensures very slight changes in the height of the box during the course of the simulation. The lateral area of the simulation box was maintained for both the flat and curved bilayer simulations. That is, every time there is a scaling of coordinates, the size of the primary simulation box is also changed so differently scaled systems have the same lateral area.

The scaling procedure involves a gradual compression of equilibrated flat bilayers. After equilibrating the flat membranes for 2 ns, the *x* and *y* coordinates of the systems were scaled by 2% (creating a 0.98 scale factor after the initial compression). This scaling of coordinates has the effect of moving the system components towards the center of the simulation box, increasing the density of the lipids. Likewise, the size of the simulation box was also scaled accordingly to maintain the density of the system. The system then underwent an energy minimization followed by a short dynamics run of 5 ps. These steps were repeated—scaling, energy minimization, and short dynamics—

successively until the resulting system reached a scale factor of 0.70 relative to the original box size. Snapshots of the resulting structures are shown in Fig. 2.1. As can be seen, even after only 5 ps of dynamics, curvature of the membrane can be readily observed. Representative videos showing the compression process are included in the Supplementary Information (Video S1, S2, and S3).

The selected structures resulting from these short, iterative scaling processes were then allowed to further evolve for an additional 4 ns simulation. The systems scaled to 0.84, 0.80, and 0.76 (labelled as sc0.84, sc0.80 and sc0.76) were chosen for further MD simulations. In total, 30 independent bilayer systems were simulated each of which responded to compression similar to that shown in Supplementary Videos A.1, A.2 and A.3, showing curvature as a response to lateral compression. Characteristics of the simulated systems are summarized in Table A.1 (Supplementary Information). Further details on the MD simulations can be also found in the Supplementary Information. The systems with 15% POPS were simulated for a total of approximately 10 ns and the time series of the radius of curvature is shown in Supplementary Fig. A.1. Here it can be observed that there are no major transitions occurring after ~2.5 ns. Supplementary Fig. A.2 shows the time series of the radius of curvature from the beginning of compression, showing the drop in the radius as curvature is induced and maintained.

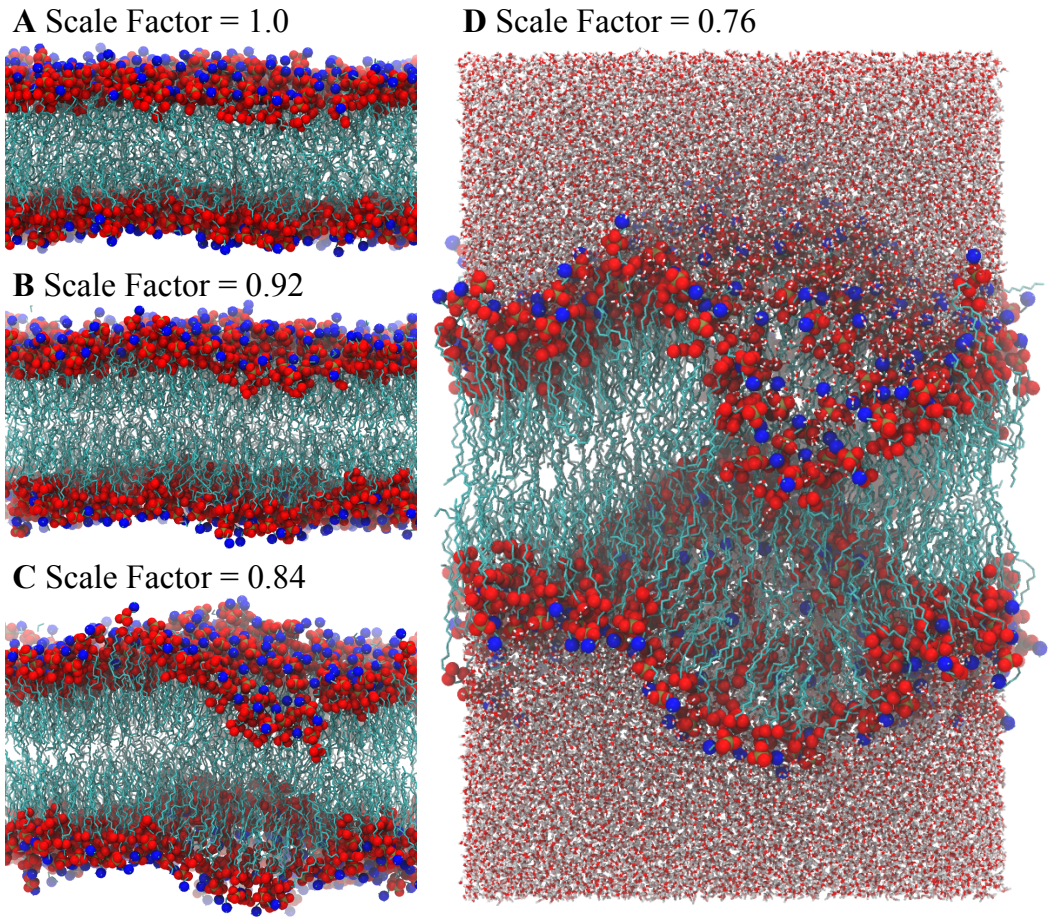

Figure 2.1. (**A**-**C**) Side views of the bilayer membranes showing increased curvature formation with increasing compression (no compression, scale factor = 1.0). Phosphate atoms are shown in red, nitrogen atoms in blue, and lipid hydrocarbon tails in teal. Waters are not shown for clarity. (**D**) Side view showing the entire simulation box including waters.

2.3.2 Membrane radius of curvature is a product of initial lipid density

To characterize the compressed bilayers, a single value was used to describe the bilayer curvature in the primary simulation box. In particular, we chose the leaflet that represents the convex or exterior side of the membrane. Computing the radius of the localized curvature found in the primary simulation box involves extracting coordinates of the phosphorus atoms from the simulation trajectories. From these, a distribution of *z*-coordinates can be constructed along an *x*-*y* surface. A sample distribution is shown in Fig. 2.2A. The crest of the resulting distribution, via periodic boundary conditions, was centered within the primary simulation box. The distribution, containing the average P atom positions over 3 ns, is then fitted to a sphere to obtain a radius of curvature. Fig. 2.2B shows the membrane curvature measures for the different simulated systems. It is expected that the smaller the scaling factor, or more compressed the system is, the more the resulting membrane would be curved. This trend is clearly demonstrated in Fig. 2.2B. Except for the sc0.84/sc0.80 scaled bilayers of the 20% POPS systems, it can be observed that the curvature increases with increased compression of the system. The anomalous points are perhaps due to insufficient equilibrium in a ~ns timescale.

The range of curvature radii obtained in this study is in good agreement with the literature reports.[57,70,80,81] Such range of curvature values obtained indicate that, for the systems used in this study, the scaling factors 76% to 84% may be used to produce bilayers to model exosomes that are sensed by curvature-binding peptides or proteins (e.g. the MARCKS-ED peptide).[57,80]

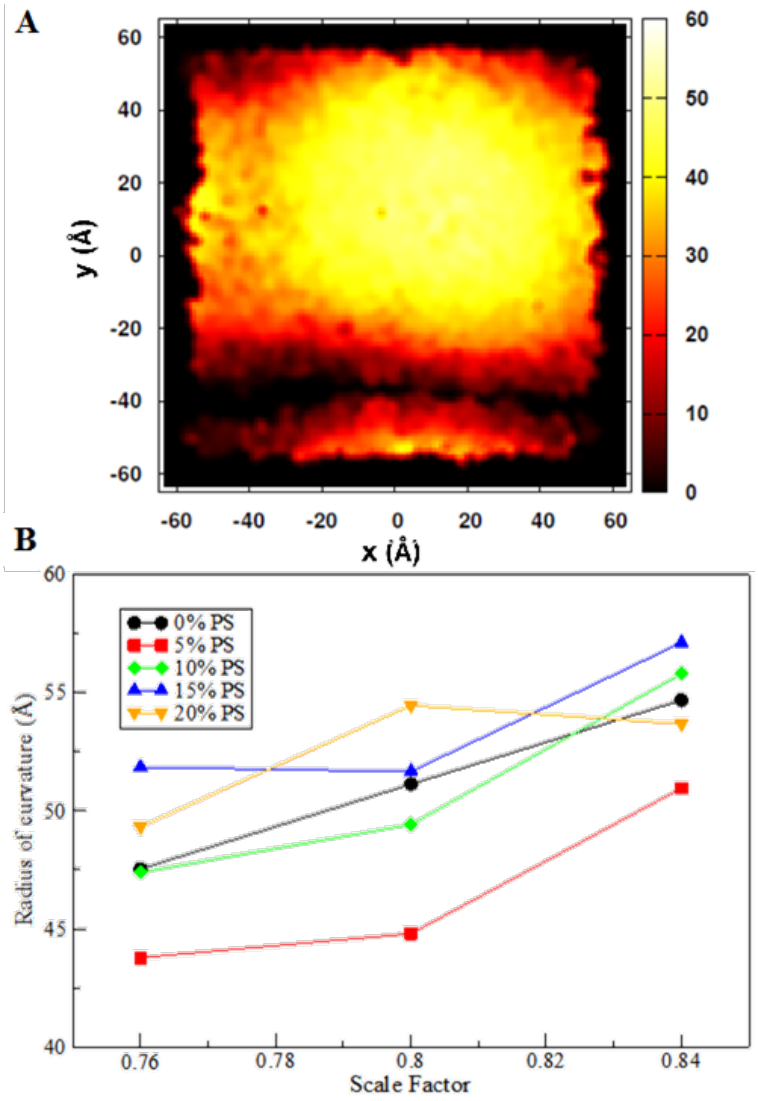

Figure 2.2. Quantification of membrane curvature. (**A**) Top view of averaged 15% POPS sc0.80 system coordinates. Coordinates in the *z* dimensions are represented by color. The color scale in Å is shown at the right. (**B**) Radii of curvature of the different lipid bilayer systems compressed by scaling the *x* and *y* coordinates (no compression, scale factor = 1.0). The labels refer to the concentration of POPS in the bilayer. Each point represents the average of two separate scaling and simulation dynamics.

As shown in Supplementary Fig. A.1 and by the movies (Video. A.1, A.2 and A.3), after undergoing the lateral compression procedure, the induced curvatures in the different bilayer systems do not disappear. Importantly, these results further emphasize that the compressed membrane bilayers are not metastable and are not likely to return to a flat state. As can also be observed from the movies, the chains are not aligning to transition to the gel phase but appear to stay in the fluid phase. With the fluid phase being more stable relative to the gel phase by ~1 kJ/mole at 10 K above the phase transition temperature (James Kindt, Emory University, personal correspondence), the fluid phase exhibited in the simulations are an expected observation.

It can also be observed from Fig. 2.2 that the effect of varying the concentration of POPS is not well defined. At high POPS concentrations, we initially expected that there should be considerable electrostatic repulsion between the negatively charged POPS lipid head groups that would lead to greater membrane curvature. The lack of a clear result may be at least in part due to insufficient equilibrium or another yet to be explained phenomenon. Increased simulation time could potentially answer this question, but with an excess of 150,000 atoms in these simulations, such studies would be quite computationally expensive. As a comparison, the simulations presented in this paper represent in excess of 2 million processor hours. We leave the question of the effect POPS lipid composition on membrane curvature open for future investigation.

2.3.3 Curved membranes have increased solvent accessible surface area (SASA)

One effect that curvature can be expected to produce in a membrane is defects in the convex surface of a curved bilayer.[57,81] The presence of defects on the surfaces

of curved membranes has been suggested to be important in curved bilayer-protein interactions.[80] As a measure of the defects produced, the solvent-accessible surface area (SASA) was determined for the convex surface of the curved bilayer using a solvent probe approximating the size of a water molecule. Fig. 2.3 shows the SASA for the different curved bilayers simulated. Except for the sc0.80 scaled bilayers of the 0% and 15% POPS systems, it can be observed that as the bilayer becomes more curved, the SASA also increases. Following the previously reported method by Cui and co-workers, defects determined via SASA calculations were mapped onto a 2D grid.[81] Representative defect maps from a single trajectory frame of the 0% PS system are shown in Figs. 2.3B and C. These figures likewise show the presence of more defects on the curved system. These results indicate that the simulated systems can provide the characteristic surface defects of curved membranes and thus, can be used for *in silico* studies of biologically relevant curved bilayer-protein interactions. As with the radius of curvature, the concentration of POPS does not appear to have a consistent effect on the extent of surface defect production.

2.4 Discussion

The biological role of submicroscopic particles, such as exosomes, is increasingly of interest. A main characteristic of these particles is a high degree membrane curvature. Through the use of MD simulations, we have devised a method for inducing curvature in lipid bilayers that can be used to investigate highly curved bilayers. Our method induces curvature by increasing the density of lipids through compression of the simulation box. We have found that curvature can be induced

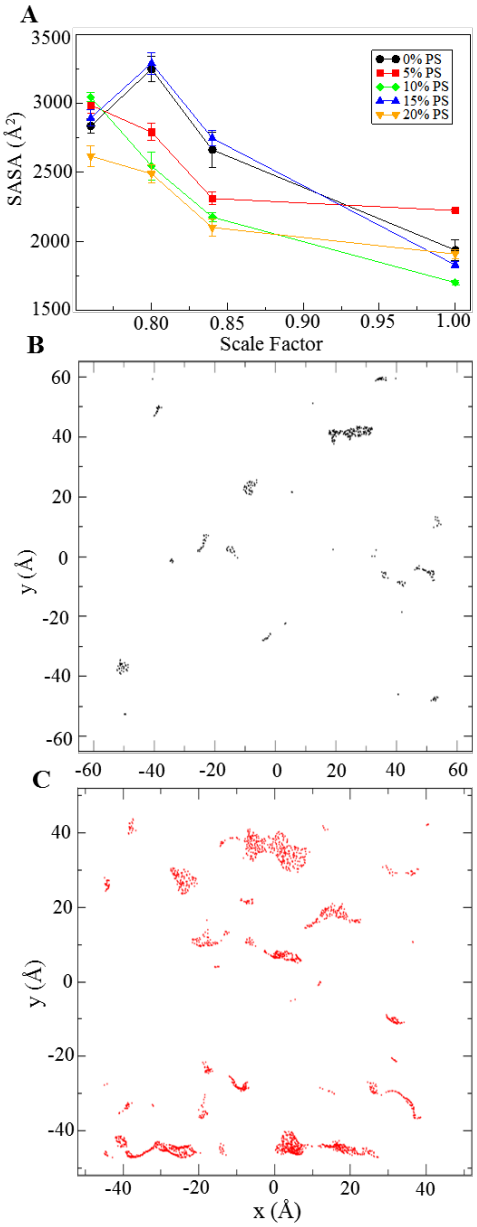

Figure 2.3. Solvent-accessible surface area (SASA) of the convex surface of the compressed bilayer systems. (**A**). Average SASA values. The labels refer to the concentration of POPS in the bilayer. Error bars represent standard errors of the mean. (**B** and **C**). 2D map of defect locations across the surface of a flat (**B**) and curved (**C**) bilayer.

relatively quickly (within 5 ps) in model bilayer systems. The degree of curvature of the bilayer is found to increase with elevated lipid density. Cellular processes such budding off of highly curved vesicles are likely to give rise to extremely curved regions which could be modelled by the range of curvatures observed in this work. Such range of curvatures are also observed in computational studies of tubulation and buckled bilayers.[70,80] Curvatures with greater radii may be induced in larger bilayers. For a fully atomistic study such described in this work, this will greatly add to the computational expense and thus, we leave the investigation of larger bilayers for future investigation. The amount of surface defects produced by membrane curvature also increases with lipid density. The bilayer membranes produced by this method can be used as models to study lipid-lipid and lipid-protein interactions in highly curved bilayers, providing a useful tool to investigate biologic processes that involve dynamic changes in membrane shape.

2.5 Methods

2.5.1 Modeled membrane bilayer systems

We have investigated a series of hydrated lipid bilayer systems containing varying amounts of 1-palmitoyl-2-oleoyl-sn-glycero-3-phosphatidylcholine (POPC) and 1-palmitoyl-2-oleoyl-sn-glycero-3-phosphatidylserine (POPS). The amount of POPS was varied as follows: 0% PS, 5% PS, 10% PS, 15% PS and 20% PS. Two independent systems for each POPS concentration were simulated for a total of ten model bilayers. The Membrane Builder module in CHARMM-GUI was used to construct the systems that are composed of a lipid bilayer, water and ions.[79] Each system was

composed of 250 lipids per leaflet and ~29,000 waters. Each simulation system contained on average ~150000 atoms. A 0.25-M concentration of KCl was used for all simulations. The system characteristics are summarized in Supplementary Table S1.

These ten systems were initially simulated as flat bilayers. Rectangular periodic boundary conditions were imposed with a variable box height of ~90 Å and xy-translation lengths of ~130 Å. The latter dimension was based on 68.3-Å^2 and 62-Å^2 area/lipid ratios for POPC and POPS, respectively.[79] The method used in building these systems also ensured that the correct density of water was used. During the scaling of the *x*- and *y*-coordinates to increase the lipid density, the box size along the *z*-direction was increased accordingly so that the volume of the simulation box was preserved and the water density was maintained.

2.5.2 Molecular dynamics procedure

The CHemistry at HARvard Macromolecular Mechanics (CHARMM) program was used for this study making use of the CHARMM36 lipid force field and the TIP3P model for water with bonds to hydrogen atoms fixed with the SHAKE algorithm.[82-85] The particle-mesh Ewald (PME) method was employed to calculate the electrostatics using a mesh size of ~1 Å for fast Fourier transformation, κ = 0.34/Å and a sixth-order B-spline interpolation.[86] Non-bond pair lists were constructed using a 16-Å cutoff distance and the Lennard-Jones potential was smoothly switched off at 10-12 Å using a force-switching function. Simulations were performed under constant temperature (330 K) and normal pressure (1.0 atm) with a fixed lateral area using Nosé-Hoover methods and the Langevin piston.[87-89]

2.5.3 Bilayer characterization

The radius of curvature of each bilayer system was computed based on the coordinates of the phosphorus atoms of the lipids. These coordinates of the phosphorus atoms were collected at regular intervals and a distribution of its *z*-coordinates across the *x*-*y* simulation box was calculated. From this distribution, the maximum point of the curvature was located and the surface was translated such that the maximum was centered on the origin. Periodic boundaries were used during the centering and translation. This distribution was fitted to a sphere to obtain the radius of curvature of the bilayer.

The solvent accessible surface area (SASA) of the bilayer surface was obtained via the coordinate manipulation facility of CHARMM. It uses the Lee and Richards method for computing the SASA of the selected atoms.[90]

Chapter 3

Theoretical models of lipid membrane biophysical forces provide predictions of extracellular vesicle behavior *in vivo* and in experiments

3.1 Introduction

Microvesicles and exosomes are submicron sized vesicles found in the extracellular space. The vesicles are made up of a bilayer lipid membrane, with the potential to carry signaling lipids and transmembrane proteins, and an aqueous core that can contain nucleic acids and globular proteins.[1] Packaging these molecules into a single vesicle creates a unique signaling mechanism that allows for the combined simultaneous temporal and spatial localization of multiple biochemical signals.

Microvesicles and exosomes differ in cellular origins and absolute vesicle size. Exosomes are released when late endosomal compartments called microvesicular bodies fuse with the cell membrane and are typically described as being 30 to 100 nm in diameter.[22,23] Conversely, microvesicles directly bud from the plasma membrane and are generally described as being 100 to 1000 nm in diameter.[15] There is a growing list of normal physiologic functions of microvesicles and exosomes including angiogenesis,

cytokine release, and transfer of cell receptors and genetic information, as well as pathophysiologic functions such as cancer immune suppression and metastasis.[4,31,32]

While our understanding of the remarkable complexity of exosome and microvesicles in normal and pathophysiologic processes is rapidly growing, very little is known about the fundamental biophysics of these vesicles. This is due in part to the many challenges of studying these vesicles experimentally, including: 1) they are submicroscopic in size and therefore cannot be detected with conventional optical methods, 2) their multifaceted physiologic functions and origins make antibody based detection problematic, and 3) isolation of the vesicles from media and body fluids is labor intensive and often results in samples of dubious purity. Basic questions such as how exosomes and microvesicles signal, fuse, or become endocytosed by their target cells are largely unanswered. To understand better some of the fundamental biophysical forces that occur between these vesicles and vesicle/cells, we can construct and examine theoretical estimates. Here we describe how quantitative theoretical estimates of these forces can provide insight into what may be occurring in biologic, as well as experimental, processes involving exosomes and microvesicles.

3.2 Results

3.2.1 A theoretical model for describing extracellular vesicle-cell membrane interactions

Theoretical estimates of the intermembrane forces that occur between exosomes and microvesicles, as well as between vesicles and the plasma membrane, can potentially provide insight into the vesicles' basic biophysical behavior *in vivo* and in

experiments. Estimating these forces requires consideration of the many ways that bilayer membranes can interact. Here we consider four distinct interactions: van der Waals (VDW), double layer (DL), protrusion (PRO) and undulation (UND) forces.[91] Forces due to water molecule ordering, such as hydration or hydrophobic interactions, are not included since the bilayer membranes that make up exosomes and microvesicles are relatively deformable and composed of lipids with hydrophilic head groups.

The van der Waals and the double layer force are the two components of the DLVO (Derjaguin, Landau, Verwey, and Overbeek) theory of colloid stability.[91] Except at molecular contact, the van der Waals interaction between two surfaces is an attractive interaction due to permanent or induced dipoles. The van der Waals interaction between two spherical particles is given by

$$F_{VDW} = \frac{-A}{6D^2}\left(\frac{R_1 R_2}{R_1 + R_2}\right)$$

$$E_{VDW} = \frac{-A}{6D}\left(\frac{R_1 R_2}{R_1 + R_2}\right)$$

where A is the Hamaker constant and is roughly equal to 0.8 x 10^{-20} J for lipid bilayers, D is the separation between the surfaces, and R_1 and R_2 are the radii of the vesicles.[92] The electric double layer interaction is an electrostatic interaction that is repulsive between like charged membranes. The double layer interaction between two spherical particles is given by

$$F_{DL} = \kappa\left(\frac{R_1 R_2}{R_1 + R_2}\right) Z e^{-\kappa D}$$

$$E_{DL} = \left(\frac{R_1 R_2}{R_1 + R_2}\right) Z e^{-\kappa D}$$

where at physiologic conditions, 0.15 M NaCl and 37 °C, $\kappa^{-1} \approx 0.8$ nm and the constant $Z \approx 1.20 \times 10^{-11}$ J m^{-1} at a membrane surface potential (Ψ_0) of -40 mV. [91]

The protrusion and undulation interactions are two major entropic forces unique to lipid membranes. The protrusion force describes the repulsive steric interaction between two membranes that occurs when lipid head groups are pushed up out of the plane of the bilayers.[93] Protrusion interaction between two vesicles (using the Derjaguin approximation) is given by

$$F_{PRO} = 2\pi\left(\frac{R_1 R_2}{R_1 + R_2}\right) 3\Gamma k_B T e^{-D/\lambda_0}$$

$$E_{PRO} = 2\pi\left(\frac{R_1 R_2}{R_1 + R_2}\right) 3\Gamma k_B T \lambda_0 e^{-D/\lambda_0}$$

where Γ is the surface density of the protruding molecules (roughly equal to 1x10^{18} m^{-2}) and λ_0 is the decay length (0.2 nm is used in this case).[93] The undulation force is also repulsive and arises from wave-like thermal ripples that occur when two lipid membranes approach each other.[94] The undulation interaction between two vesicles (again, using the Derjaguin approximation) is given by

$$F_{UND} = 2\pi\left(\frac{R_1 R_2}{R_1 + R_2}\right) \frac{[k_B T]^2}{2K_c D^2}$$

$$E_{UND} = 2\pi\left(\frac{R_1 R_2}{R_1 + R_2}\right) \frac{[k_B T]^2}{2K_c D}$$

where K_c is the bending modulus of the membrane (roughly equal to 1x10^{-19} J).[95]

The energy of the sum of these four interactions is given by

$$E_{Total} = E_{VDW} + E_{DL} + E_{PRO} + E_{UND}$$

$$E_{Total} = \left(\frac{R_1 R_2}{R_1 + R_2}\right)\left(\frac{-A}{6D} + Ze^{-\kappa D} + 2\pi 3\Gamma k_B T \lambda_0 e^{-D/\lambda_0} + 2\pi\frac{[k_B T]^2}{2K_c D}\right)$$

Fig. 3.1 shows how the potential energy of each interaction varies as a 100 nm exosome approaches an 8 μm cell. The net interaction is primarily repulsive with a barrier of 40 k_bT at D = 2 Å, the point at which a single layer of water molecules would exist between the two membranes.[91] An energy minimum of -1.5 k_bT at D = 4.9 nm is the effective "bond" strength and length between the vesicle and cell membranes. Table 3.1 summarizes the interactions of additional sizes of exosomes and microvesicles with an 8 μm cell. Fig. 3.2 shows how, for each vesicle size, the total potential energy varies with membrane separation.

3.2.2 Predicting extracellular vesicle signaling mechanisms

Three distinct mechanisms have been suggested for how vesicles might signal and interact with their target cell's plasma membrane. They are: 1) vesicle ligand-membrane receptor interactions, 2) vesicle-membrane fusion, and 3) vesicle endocytosis.[44] In order for a vesicle ligand-membrane receptor interaction to occur, the two membranes would need to form a stable "bond" at a small intermembrane separation. This bond would likely be facilitated by the interaction of transmembrane or membrane tethered proteins embedded in the vesicle and cell bilayers. This interaction would allow for signaling and would also stabilize the bond between the two membranes. The interaction energy between the vesicle and cell membranes could also potentially stabilize the bond. The theoretical energy minimums listed in Table 3.1 indicate that larger vesicles form more energetically favorable bonds with the plasma membrane. As these bonds would further stabilize a ligand-receptor interaction,

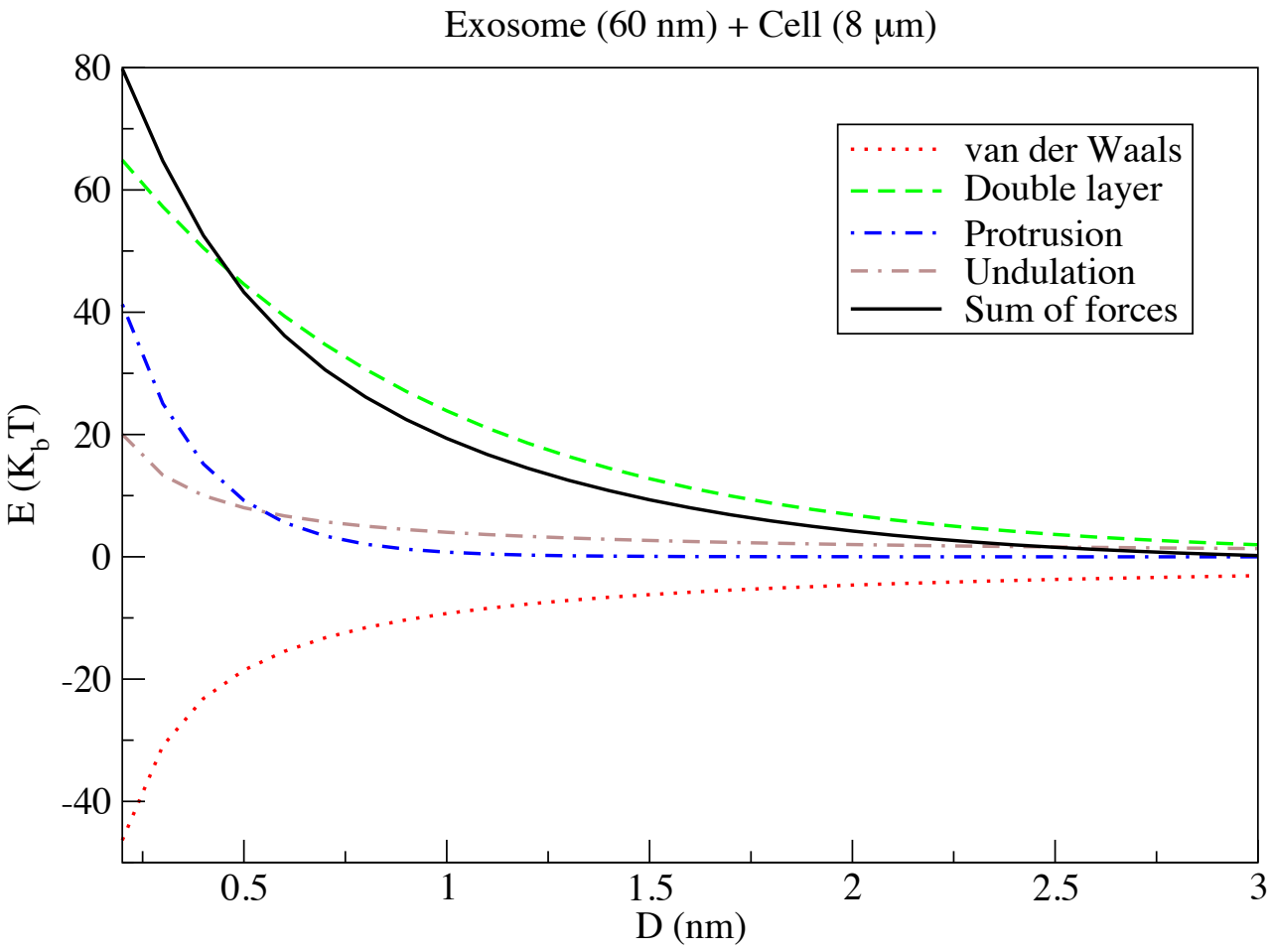

Figure 3.1. Contribution of relevant membrane - membrane forces to the potential energy of a 60 nm exosome approaching an 8 μm cell.

Diameter (nm)	Vesicle type	Energy at D = 2 Å (k_bT)	Energy minimum (k_bT)	Intrinsic bond lifetime (s)
30	Exosome	40	-0.45	2.4×10^{-7}
60	Exosome	80	-0.89	1.5×10^{-6}
100	Exosome	130	-1.5	6.4×10^{-6}
250	Microvesicle	330	-3.6	2.4×10^{-4}
500	Microvesicle	630	-7.1	2.2×10^{-2}
1000	Microvesicle	1200	-13	32

Table 3.1. Summary of interaction energies and intrinsic bond lifetimes between different sized extracellular vesicles and an 8 μm cell.

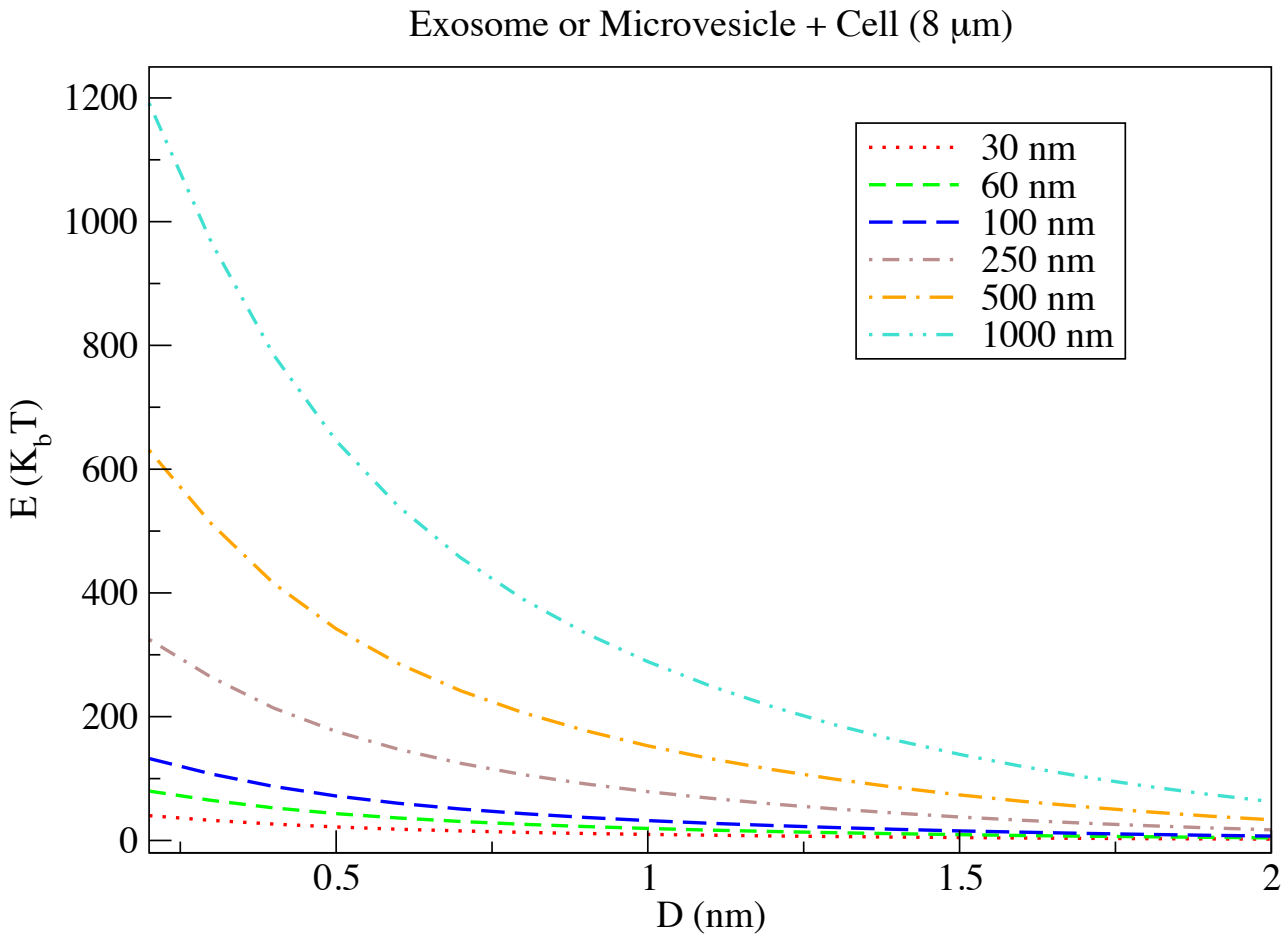

Figure 3.2. Potential energy of exosomes (dashed only lines) and microvesicles (dashed and dotted lines) approaching an 8 μm cell.

microvesicles are a far more likely candidate for vesicle ligand-membrane receptor signaling than exosomes.

The second suggested signaling mechanism is vesicle-membrane fusion. In this case, transmembrane proteins embedded in the vesicle would be incorporated into the cell membrane. Any globular proteins or nucleic acids contained in the aqueous core of the vesicles would be released into the cell cytosol. If an exosome or microvesicle were to signal by fusing with the plasma membrane, the two membranes would first need to be in very close (molecular) contact. Our theoretical estimates show that with increasing vesicle size the energy barrier for vesicle-cell membrane molecular contact grows. Recently, the free energy output of the neuronal SNARE complex that facilitates vesicle-membrane fusion has been reported to be ~65 k_bT.[96] This energy output is on the scale of what we predict would be required to induce exosome-cell membrane fusion. The estimated molecular contact energy barrier for microvesicle is much larger, suggesting different machinery would likely be needed to induce microvesicle-plasma membrane fusion. Given the size of the energy barrier, the more likely explanation is that exosomes signal via fusion, while microvesicles signal without fusing, via a vesicle ligand-membrane receptor interaction.

The theoretical vesicle-membrane bond energies can be also used to calculate the intrinsic bond lifetime (τ_0) of the interactions. Intrinsic bond lifetime is given by

$$\tau_0 = \frac{1}{\upsilon_0} e^{+E_{act}/_{k_B T}}$$

where υ_0 is the characteristic vibration frequency of the bond [91]. The characteristic bond frequency is related to the velocity of the particle and the width of the bond and can be estimated using

$$\upsilon_0 = \frac{Velocity_{vesicle}}{Width\ of\ bond} = \frac{\sqrt{\frac{k_B T}{Mass_{vesicle}}}}{Width\ of\ bond}$$

Here we estimate the mass of the vesicle with

$$Mass_{vesicle} = \frac{2(SA_{vesicle})(Mass_{lipid})}{SA_{lipid}} + Mass_{water\ core}$$

where $SA_{vesicle}$ is the surface area of a sphere with same diameter as the vesicle of interest, $Mass_{lipid}$ is the mass of single lipid molecule, SA_{lipid} is the surface area of a single lipid in an equilibrated planar membrane, and $Mass_{water\ core}$ is the mass of a spherical water core with a diameter 10 nm less than the vesicle diameter to account for the thickness of the bilayer. Multiplying by a factor of two accounts for the two lipid layers of the bilayer. Since DOPC is the most common lipid in exosomes, its surface area and weight were used in this estimation.[21,97]

The estimated intrinsic bond lifetimes for the microvesicles are multiple orders of magnitude longer than the exosomes. For the 1000 nm microvesicle, the bond lifetime is on the order of seconds. The large increase in intrinsic bond lifetime is due in part to a greater bonding energy, but also a lower characteristic vibration frequency because of the vesicle's greater mass. While the portion of exosomes or microvesicles in a body fluid or experimental sample that are in a "bonded" state will depend on their respective concentrations, these calculations indicate microvesicles form longer lasting bonds with the plasma membrane.

3.2.3 Polymer depletion attraction may drive extracellular vesicle aggregation

As discussed earlier, the proper isolation of the vesicles from media and body fluids is a challenging process. Many methods exist to isolate exosomes and

microvesicles. These methods include differential centrifugation and filtration, density gradient centrifugation, sucrose gradient flotation, and ExoQuick precipitation. [98,99] ExoQuick precipitation is one of the most widely used methods. The ExoQuick solution is composed of a proprietary polymer mixture of unknown composition that selectively precipitates exosomes. Electron microscopy imaging of ExoQuick precipitated exosomes has demonstrated interesting aggregations of small vesicles around the periphery of larger vesicles that do not appear when exosomes are isolated using other methods (unpublished observation Peter N. Brown). One possible explanation of this phenomenon is that the ExoQuick polymer is causing a depletion attraction that increases the binding energy of the vesicles.

The theoretical polymer induced depletion attraction between two vesicles (again, using the Derjaguin approximation) is given by

$$F_{DEP} = -2\pi\left(\frac{R_1 R_2}{R_1 + R_2}\right)\rho k_B T(R_g - D)$$

$$E_{DEP} = -2\pi\left(\frac{R_1 R_2}{R_1 + R_2}\right)\rho k_B T\left(DR_g - \frac{D^2}{2}\right)$$

where ρ is the number of polymer molecules in a unit volume and R_g is the radius of gyration of the specific polymer.[91] For example, what happens to the potential energy of an interaction between a 30 nm and 100 nm exosome when they are in water solution that is 30% by weight MW 5000 PEG? The radius of gyration (R_g) of the PEG can be estimated using

$$R_g = 0.2{M_w}^{0.58}$$

where M_w is the molecular weight of the polymer.[100] The density of the polymer is given by

$$\rho = 6.022\times10^{29}(C_w)/M_w$$

where C_w is the polymer weight percent in water. [91]

As shown in Table 3.2 and Fig. 3.3, the depletion attraction increases the binding energy of the 30 and 100 nm vesicles by ~9.6 k_bT and the relative intrinsic bond lifetime by four orders of magnitude. The depletion attraction has very little effect on the molecular contact energy barrier, suggesting it would not facilitate fusion between the exosomes. Although this estimate is particularly rough given the unknown composition of ExoQuick, a change in the bond energy between the vesicles of the magnitude described may explain the exosome aggregation seen on electron microscopy.

3.3 Discussion

In this work we have shown how theoretical estimates of membrane forces acting on exosomes and microvesicles can provide insight into vesicle biology and experimental results. The estimates can be predictive, such as microvesicles being more likely to signal via a vesicle ligand-membrane receptor interaction and exosomes being more likely to signal via vesicle-membrane fusion, or explanatory, such as ExoQuick potentially causing a depletion attraction that leads to aggregation of purified exosomes. We hope that these estimates can guide future experimental efforts to further define both the biophysical forces present in, and signaling mechanisms of, exosomes and microvesicles.

Diameter (nm)	Vesicle types	Energy at D = 2 Å (k_bT)	Energy minimum (k_bT)	Intrinsic bond lifetime (s)
30/100	Exosomes	31	-0.35 at D = 4.9 nm	2.2×10^{-7}
30/100+PEG	Exosomes	30	-10 at D = 2.8 nm	1.9×10^{-3}

Table 3.2. Effect of the addition of 30% by weight MW 5000 PEG to the interaction of a 30 nm and 100 nm exosome.

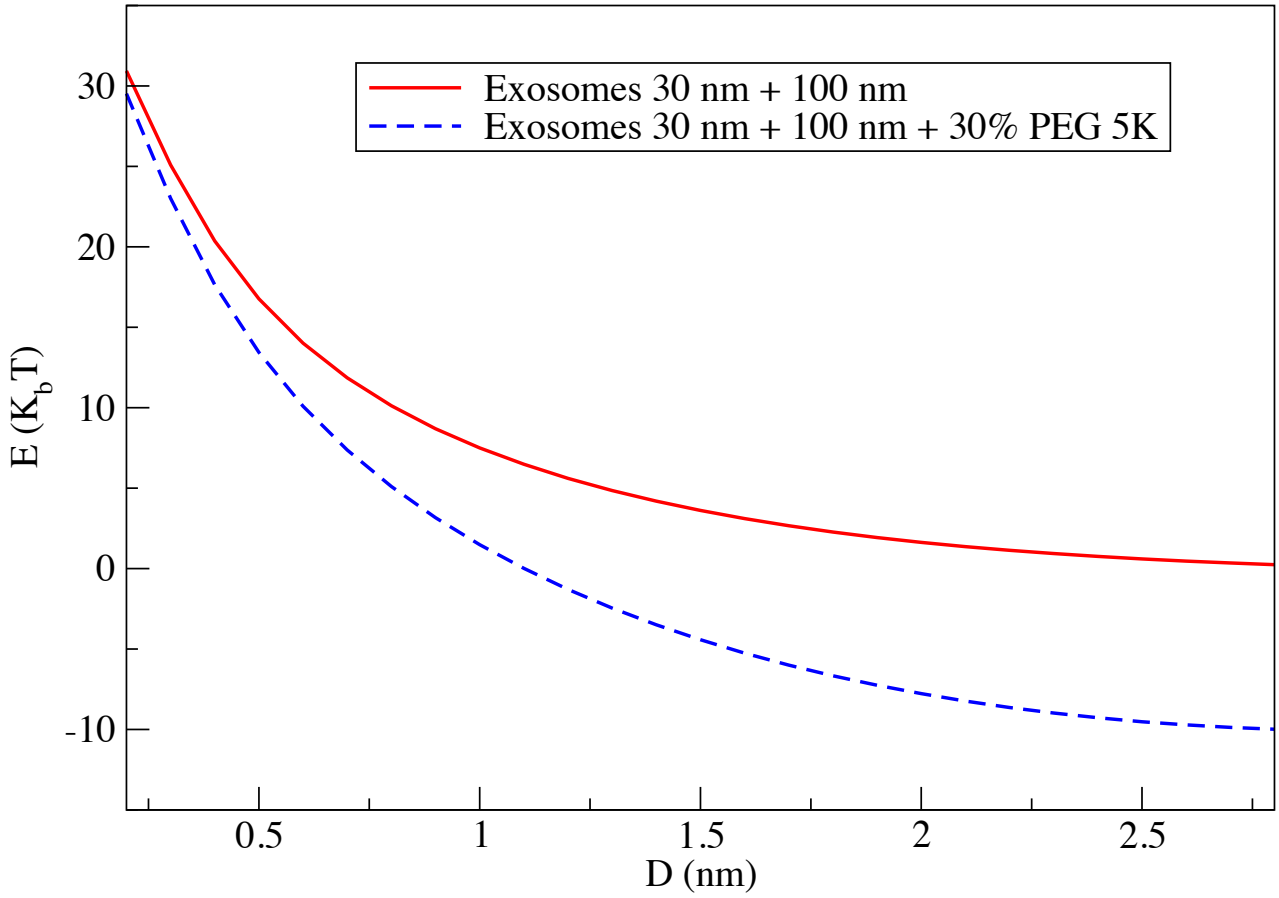

Figure 3.3. Polymer depletion forces decrease the potential energy of a 30 nm exosome approaching a 100 nm exosome. The dashed blue line represents the interaction after the addition of 30% by weight MW 5000 PEG.

Chapter 4

Peptides derived from MARCKS block coagulation protein complex assembly on phosphatidylserine and inhibit fibrin formation

4.1 Abstract

Blood coagulation involves activation of platelets and coagulation factors. At the interface of these two processes resides the lipid phosphatidylserine. Activated platelets expose phosphatidylserine on their outer membrane leaflet and activated clotting factors assemble into enzymatically active complexes on the exposed lipid, ultimately leading to the formation of fibrin. Here, we describe how small peptide and peptidomimetic probes derived from the lipid binding domain of the protein myristoylated alanine-rich C-kinase substrate (MARCKS) bind to phosphatidylserine exposed on activated platelets and thereby inhibit fibrin formation. The MARCKS peptides antagonize the binding of factor Xa to phosphatidylserine and inhibit the enzymatic activity of prothrombinase. In whole blood under flow, the MARCKS peptides colocalize with, and inhibit fibrin cross-linking, of adherent platelets. *In vivo*, we find that the MARCKS peptides circulate to remote injuries and bind to activated platelets in the inner core of developing thrombi.

4.2 Introduction

Phosphatidylserine (PS) is an essential cofactor of the coagulation proteins involved in hemostasis and thrombosis. PS is an anionic lipid that is normally sequestered to the inner leaflet of the plasma membranes and only exposed on the outer membrane surface during activated processes like apoptosis or platelet activation. During blood clotting, activated platelets undergo changes in membrane shape and expose PS on their outer membrane leaflet via calcium-dependent phospholipid scramblases.[101-103] Activated coagulation factors in the presence of calcium and PS assemble into enzymatically active complexes, e.g., prothrombinase, a complex of activated factor Xa (FXa) and Va (FVa).[104-106] The enzymatic activity of these coagulation protein complexes ultimately leads to the formation of fibrin, an insoluble polymer that forms an affixing crosslinking mesh around the hemostatic platelet plug.

In this work, we explore the effect of small PS-binding peptides on blood coagulation. The peptides are based on the protein myristoylated alanine-rich C kinase substrate (MARCKS), a 32 kDa protein that sits at the interface of many lipid-protein interactions. Full length MARCKS protein has two important known functional domains: a myristoylated N-terminus that inserts into, and localizes the protein to, the inner leaflet of the plasma membrane, and a highly basic effector domain that mediates its biologic functions by reversibly binding the plasma membrane.[107] Phosphorylation of the effector domain by protein kinase C, or binding by calmodulin in the presence of calcium, inhibit the domain's association to the plasma membrane, releasing sequestered phosphoinositides and disrupting the actin network around the

membrane.[108-112] The actions of the MARCKS protein have been implicated in neurodevelopment, cell motility, and endo- and exocytosis.[113-115]

We have previously demonstrated that peptides based on the effector domain of MARCKS (MARCKS ED) bind with increasing affinity to lipid membranes that are both highly curved and enriched in PS.[57] MARCKS ED does not adopt a secondary structure. Rather, the peptide forms a random coil conformation that selectively binds through electrostatic attraction between its 13 basic residues and the acidic phosphatidylserine lipid head groups, and the insertion of bulky phenylalanine residues into the hydrophobic membrane core (Fig. 4.1a).[116-118] The affinity of MARCKS ED for curved and PS enriched membranes is sequence specific, but independent of the amino acid stereo conformation.[117,118] MARCKS ED is less than a tenth of the molecular weight of PS binding proteins annexin V and lactadherin, and comparatively easy to synthesize and modify using solid phase peptide synthesis. Moreover, unlike annexin V, MARCKS ED does not require calcium to bind to PS.[57]

Having established the affinity of MARCKS ED for PS, we sought here to determine if the peptide could affect the binding of coagulation factors to PS. We hypothesized that MARCKS ED would bind to the curved membranes and exposed PS of activated platelets. We establish that the MARCKS ED peptide can antagonize the interaction between coagulation factors and PS, and that this activity significantly reduces coagulation factor enzymatic activity. We find that MARCKS ED only binds to platelets that are activated and, in whole blood, inhibits the formation of fibrin, the end product of the coagulation cascade. Finally, we show *in vivo* that MARCKS ED can circulate to a remote injury site and bind to activated platelets in the core of a

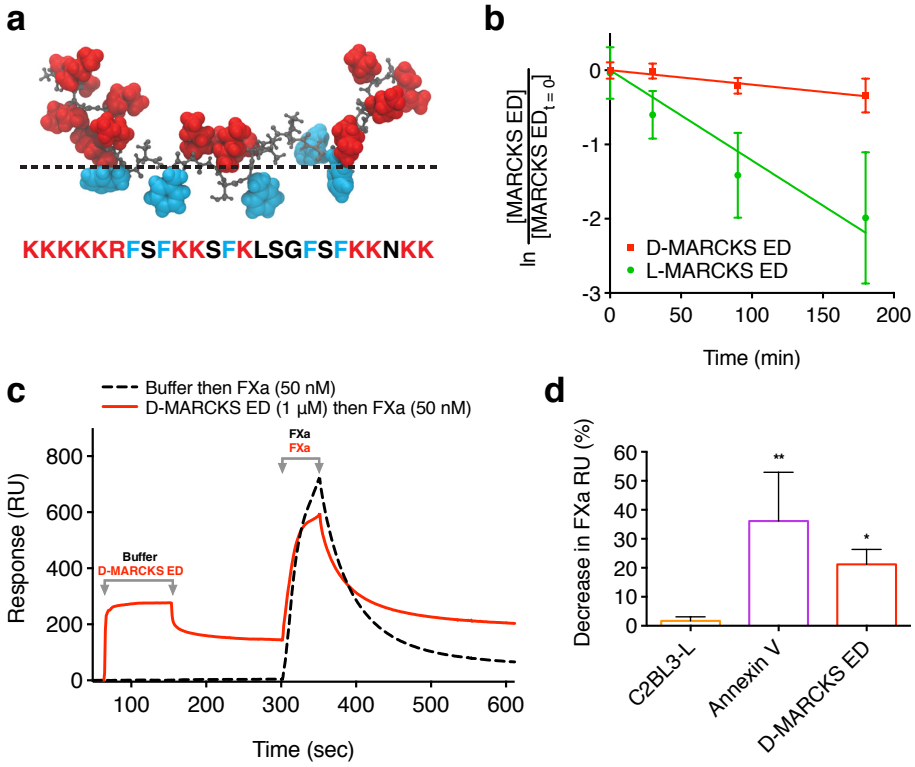

Figure 4.1. D-MARCKS ED is a protease resistant peptide that antagonizes the binding of FXa to PS. (**a**) Sequence and representative membrane bound conformation of the MARCKS ED peptide. Positively charged residues are shown in red and phenylalanine residues are shown in blue. Dashed line shows approximate location of the membrane lipid head groups. (**b**) Comparison of the human serum stability of L-MARCKS ED ($t_{1/2}$ = 57 min, 95% confidence interval (CI) 46 to 79 min) and D-MARCKS ED ($t_{1/2}$ = 356 min, 95% CI 252 to 606 min) peptides (n = 3, mean ± s.d.). (**c**) Representative reference corrected Biacore 3000 SPR sensogram showing D-MARCKS ED antagonizes the binding of FXa to lipid membrane surface containing PS. Dashed black line shows an injection of running buffer at t = 30 sec and an injection of 50 nM FXa at t = 300 sec. Following complete dissociation of FXa from the membrane surface, the solid red line shows an injection of 1 μM D-MARCKS ED at t = 30 sec and an injection of 50 nM FXa at t = 300 sec. (**d**) Quantification of FXa SPR binding inhibition with BiOptix 404pi instrument by negative control C2BL3-L, positive control annexin V, and D-MARCKS ED (n = 3 C2BL3-L and annexin V; n = 5 D-MARCKS ED, mean ± s.d.). * $P < 0.05$, ** $P < 0.01$ compared to C2BL3-L by one-way analysis of variance (ANOVA) and Dunnett's *post hoc* test (**d**).

developing thrombus. We establish that a peptide can antagonize a lipid-protein interaction, and that this activity can have significant effects in a complex multicomponent pathway like blood coagulation.

4.3 Results

4.3.1 D-MARCKS ED is protease resistant

Peptides in blood are exposed to an array of proteases that may reduce their biologic activity.[119] Since MARCKS ED binding is independent of amino acid chirality, the peptidomimetic D-amino acid form of MARCKS ED has the potential comparative advantage of increased resistance to protease degradation and reduced likelihood of native biologic recognition or activity.[117,118] We first sought to confirm that D-MARCKS ED is the more stable isoform to proteolysis. Separate incubation of the two peptides with human plasma resulted in pseudo-first-order degradation of the peptides (Fig. 4.1b). We observed the half-life of D-MARCKS ED to be roughly six times longer than that of L-MARCKS ED. Based on this result, we chose to use D-MARCKS ED for studies where only a single isoform could be reasonably tested.

4.3.2 D-MARCKS ED antagonizes binding of FXa to PS

To investigate if MARCKS ED could antagonize the binding of a coagulation factor to PS, we used surface plasmon resonance (SPR). Buffer or D-MARCKS ED was flowed over an immobilized lipid surface containing PS. After 160 seconds, FXa was then injected over the lipids and the binding response was recorded. Pretreatment of the same surface with D-MARCKS ED resulted in a 50% (± SD of 5%) mean

reduction in FXa membrane binding as compared to the buffer treatment using a Biacore 3000 instrument (Fig. 4.1c and Supplementary Fig. B.1a). We repeated this experiment on a BiOptix 404pi instrument. Compared to the Biacore 3000 instrument, the BiOptix 404pi instrument absorbed approximately six times more lipid reference units (RU) to the SPR HPP chip surface (not shown) and showed reduced FXa binding inhibition by D-MARCKS ED (Fig. 4.1d and Supplementary Fig. B.1b) with equivalent injection concentrations, association volumes, and flow rates. To validate these results, annexin V was also tested to serve as a positive control and C2BL3-L, a small peptide previously shown to have poor affinity for PS, was tested to serve as a negative control (Fig. 4.1d and Supplementary Fig. B.1c,d).[58]

The observed difference in FXa binding inhibition by D-MARCKS ED with the two instruments likely relates to the stoichiometry of the MARCKS ED/PS interaction and the resulting relative PS surface coverage of D-MARCKS ED in each experiment. Previous work investigating the interaction of D-MARCKS ED with the lipid phosphatidylinositol 4,5-bisphosphate (PIP_2) has shown that the stoichiometry of the interaction is determined by electrostatic complementarity between the peptide and lipids.[120,121] The D-MARCKS ED peptide has a net positive charge of 13 at physiologic pH, suggesting each D-MARCKS ED peptide could bind and block up to 13 PS lipids. Using this stoichiometry and the RU definition of both SPR instruments (1000 RU = 1 ng mm^{-2}), we make the approximation that D-MARCKS ED blocked 82% (± SD of 9%) of PS in the Biacore 3000 experiment and this resulted in a 50% (± SD of 5%) reduction in FXa binding. In comparison, with the increased lipid loading seen with the BiOptix 404pi, we approximate that D-MARCKS ED blocked 7% (± SD of 3%) of PS and this

resulted in a 23% (± SD of 5%) reduction in FXa binding in the BiOptix 404pi experiment. Since the injections of D-MARCKS ED and FXa are separated temporally, to resolve the binding response of each ligand, and spatially, by the continuous flow of buffer over the chip, both ligands cannot simultaneously saturate the membrane surface. We therefore cannot infer stoichiometry of the inhibition, but do observe that more D-MARCKS ED surface coverage results in reduced FXa binding, supporting our initial hypothesis that MARCKS ED could antagonize the binding of a coagulation factor to PS.

4.3.3 MARCKS ED binds to activated platelets and inhibits prothrombinase

To determine if antagonizing the binding of coagulation factors to PS with MARCKS ED resulted in reduced enzymatic activity, we used a platelet-dependent prothrombinase assay. In the presence of human platelets activated by convulxin and thrombin, L- and D-MARCKS ED both reduced prothrombinase activity by greater than 50% (Fig. 4.2a). Given the slight reduction in prothrombinase activity observed with our negative control peptide C2BL3-L, L-MARCKS ED FA (a MARCKS ED peptide where membrane affinity is reduced by replacing all phenylalanine residues with alanine) was added as an additional negative control and did not show any inhibition (Fig. 4.2a).[57] Interestingly, a dose response curve with D-MARCKS ED showed the peptide could not completely inhibit the formation of thrombin (Fig. 4.2b). It has been shown previously that activation of platelets by convulxin and thrombin generates a unique subpopulation of approximately 30% of activated platelets that express high levels of procoagulant proteins – including membrane surface bound FVa, likely originating in the platelet α

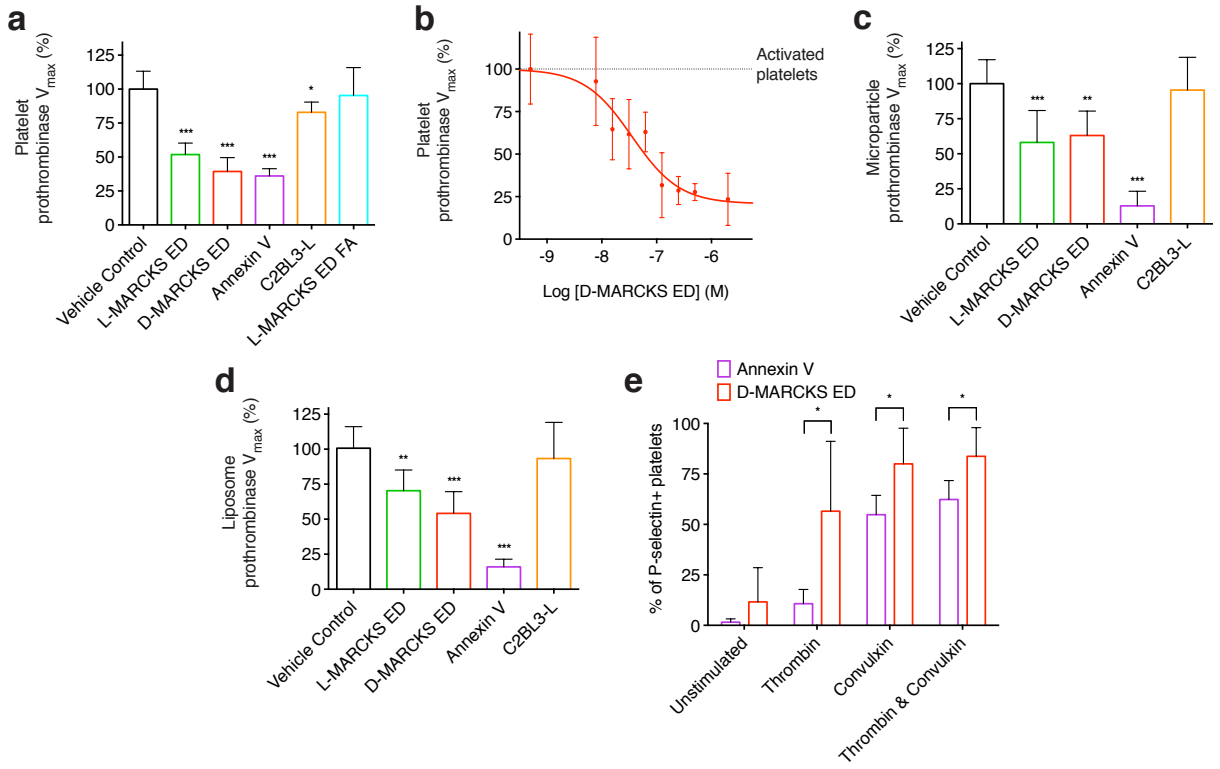

Figure 4.2. MARCKS ED inhibits prothrombinase enzymatic activity in the presence of PS containing membranes and only binds to activated platelets. (a) Prothrombinase activity of washed human platelets stimulated with thrombin and convulxin when pre-treated with vehicle control or 1 μM L-MARCKS ED, D-MARCKS ED, positive control annexin V, negative control C2BL3-L, or negative control L-MARCKS ED FA mutant (*n* = 8, mean ± s.d.). (**b**) Dose response of D-MARCKS ED pre-treatment on the prothrombinase activity of washed human platelets stimulated with convulxin and thrombin (*n* = 4, mean ± s.d.). (**c**) Prothrombinase activity of exosomes isolated from MDA-MB-231 cells when pre-treated with vehicle control or 1 μM L-MARCKS ED, D-MARCKS ED, annexin V, or C2BL3-L (*n* = 8, mean ± s.d.). (**d**) Prothrombinase activity of synthetic liposomes composed of POPC/POPS at a 19/1 ratio when pre-treated with vehicle control or 1 μM L-MARCKS ED, D-MARCKS ED, annexin V, or C2BL3-L (*n* = 8, mean ± s.d.). (**e**) The binding of annexin V (Brilliant Violet 605) and D-MARCKS ED (NBD) to P-selectin (Cy5) positive platelets was compared by flow cytometry when the platelets were left unstimulated or stimulated with thrombin, convulxin, or thrombin and convulxin (*n* = 6, mean ± s.d.). * $P < 0.05$, ** $P < 0.01$, *** $P < 0.001$ either by comparison to vehicle control by ANOVA followed by Dunnet's *post hoc* test (**a**,**c**,**d)** or two tailed Student's *t*-test (**e**).

granules.[122,123] As the binding of this membrane bound FVa cannot be antagonized, D-MARCKS ED may be unable to completely block prothrombinase assembly and activity resulting from this subpopulation.

We also examined the effect of MARCKS ED on prothrombinase activity in the presence of other PS-containing membranes. We repeated the prothrombinase assay, omitting the addition of platelet agonists convulxin and thrombin, using microparticles isolated from MDA-MB-231 human breast cancer cells as well as with similarly sized extruded synthetic liposomes containing PS (Supplementary Fig. B.2a,b). Microparticles were selected due to the proposed importance of PS exposure on tumor microparticles during cancer related venous thromboembolism.[124] L- and D-MARCKS ED both inhibited microparticle dependent prothrombinase activity (Fig. 4.2c). The membranes of platelets and microparticles both contain transmembrane proteins, most noteworthy for this study, tissue factor. Therefore, synthetic liposomes were used to provide an assembly surface free of any membrane proteins. The observed prothrombinase inhibition using the synthetic liposomes was similar to that seen with the microparticles (Fig. 4.2d). This result, along with the inhibition of FXa binding demonstrated by SPR, strongly suggests that MARCKS ED inhibits prothrombinase activity by directly blocking the binding of coagulation factors to PS.

4.3.4 D-MARCKS ED only binds to activated platelets

To determine if MARCKS ED bound only to activated platelets, we analyzed D-MARCKS ED and annexin V binding to platelets in the presence of a variety of activating agonists using flow cytometry. Neither D-MARCKS ED or annexin V labeled

unstimulated platelets (Fig. 4.2e and Supplementary Fig. B.3 and B.4). When platelets were activated, D-MARCKS ED labeled a greater percentage of the P-selectin positive platelets than annexin V (Fig. 4.2e). The combination of thrombin and convulxin activation resulted in the greatest percentage of P-selectin positive platelets labeled with D-MARCKS ED or annexin V (Fig. 4.2e). We observed a strong correlation between relative P-selectin positivity and D-MARCKS ED binding (Supplementary Fig. B.3). D-MARCKS ED fluorescence intensity was normally distributed and continuously increased with greater platelet activation (Supplementary Fig. B.4b). In contrast, annexin V fluorescence intensity showed a bimodal distribution that shifted into the more fluorescent population with greater platelet activation (Supplementary Fig. B.4a). This difference could be due to the membrane PS composition threshold required for annexin V binding, previously described as 2.5 to 8%, that is not required for MARCKS ED binding.[117,125]

4.3.5 MARCKS ED inhibits fibrin formation in whole blood

Next, we assessed the effects of the MARCKS ED peptides on fibrin formation in whole blood. Using a custom microfluidic device, whole human blood was flowed over an immobilized fibrilar collagen strip at a venous wall shear rate.[126] Treatment with a vehicle control resulted in the formation of a dense fibrin mesh on the adherent platelets (Fig. 4.3a and Supplementary Video B.1). When the blood was pre-incubated with L- or D-MARCKS ED peptide, no fibrin mesh formation was observed (Fig. 4.3a-c, Supplementary Fig. B.5a, and Supplementary Video B.2). Treatment with either

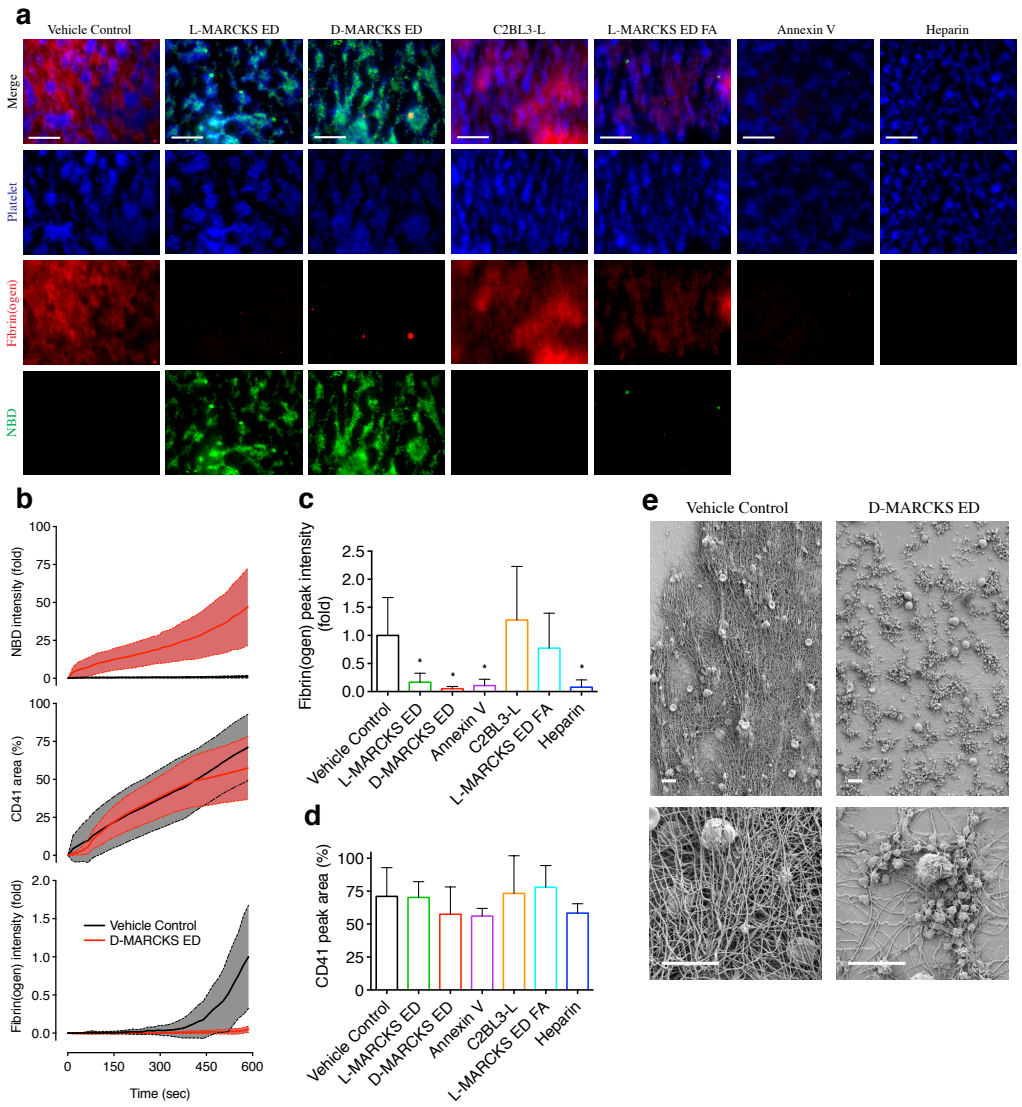

Figure 4.3. MARCKS ED inhibits fibrin formation in whole blood under physiologic flow conditions. (a) Representative images of platelet accumulation (blue, anti-CD41), fibrin(ogen) formation (red, Alexa Flour 647-fibrinogen), and peptide binding (green, NBD-peptide) in the whole blood microfluidic flow assay after 10 min at wall shear rate 100 s^{-1} when pre-treated with vehicle control or 1 μM L-MARCKS ED, D-MARCKS ED, negative control C2BL3-L, negative control L-MARCKS ED FA mutant, positive control annexin V, or positive control 15 USP ml^{-1} heparin (n = 6). Scale bar, 50 μm. (**b**) Time course of peptide NBD fluorescence intensity, platelet surface area coverage, and fibrin(ogen) intensity for the vehicle control and D-MARCKS ED treatment in the microfluidic flow assay (n = 6, mean ± s.d.). (**c**) Final fibrin(ogen) intensity values for each treatment in the microfluidic flow assay (n = 6, mean ± s.d.). (**d**) Final platelet surface coverage values for each treatment in the microfluidic flow assay (n = 6, mean ± s.d.). (**e**) Scanning electron micrographs of finals clots formed in microfluidic flow assay with vehicle control and D-MARCKS ED treatment (n = 3). Scale bar, 10 μm. * P < 0.05 compared to vehicle control by one-way analysis of variance (ANOVA) followed by Dunnet's *post hoc* test (**c**,**d**).

negative control peptide did not inhibit the formation of fibrin, while positive controls annexin V and heparin showed equivalent fibrin formation inhibition to that of the MARCKS ED peptides (Fig. 4.3a,c and Supplementary Fig. B.5b-e). No treatment appreciably changed the surface coverage percentage of the platelets, suggesting the peptides did not interfere with the interaction between platelets, von Willebrand factor, or collagen (Fig. 4.3d). Of the NBD labeled peptides, only L- and D-MARCKS ED showed significant fluorescence intensity and clear colocalization with the adherent platelets (Fig. 3e and Supplementary Fig. B.6). To confirm the fibrin formation inhibition visualized by fluorescence, the vehicle control and D-MARCKS ED final clots were fixed and visualized by scanning electron microscopy. Clots formed with vehicle control treatment showed the formation of dense fibrin mesh over the adherent platelets, while D-MARCKS ED treated samples exhibited exposed fibrillar collagen and platelet clumps, and no visible fibrin formation (Fig. 4.3e).

4.3.6 D-MARCKS ED binds to thrombi *in vivo*

To assess the *in vivo* localization of D-MARCKS ED, as well as its effects on the hemostatic response, we used a murine intravital laser-induced microvascular injury model.[127] Male mice were treated with 5 mg kg^{-1} C2BL3-L or D-MARCKS ED through a jugular vein cannula. 30 min later, fibrin and platelet deposition, as well as D-MARCKS ED fluorescence, were observed at a cremaster microcirculation injury. At the injury site, D-MARCKS ED localized primarily to the innermost area of the thrombus (Fig. 4.4a). This area is the core of thrombus, and the primary location of thrombin activity and fibrin formation.[127] Little or no C2BL3-L fluorescence was observed in the thrombi

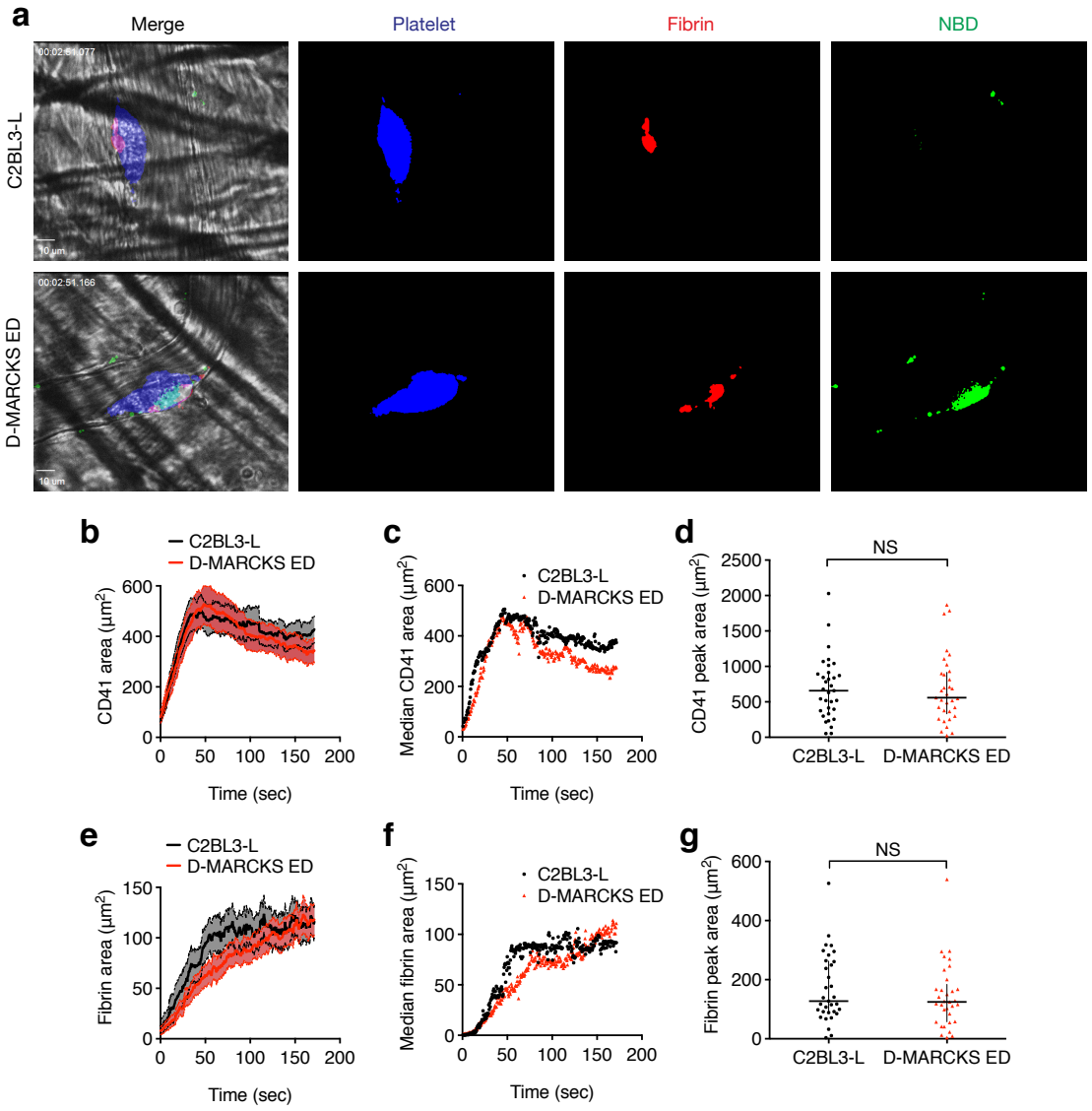

Figure 4.4. D-MARCKS ED binds to thrombi *in vivo*. (**a**) Representative fluorescence and bright field images of platelet accumulation (blue, anti-CD41), fibrin formation (red, anti-fibrin), and peptide binding (green, NBD-peptide) in the murine intravital laser-induced microvascular injury model when treated with 5 mg kg^{-1} negative control C2BL3-L or D-MARCKS ED. Scale bar, 10 μm. (**b**-**g**) Platelet and fibrin area accumulation following murine intravital microvascular injury when treated with 5 mg kg^{-1} C2BL3-L or D-MARCKS ED. Time course data is shown as mean ± s.e.m (**b**,**e**) and median (**c**,**f**) area values. Peak platelet and fibrin area values (**d**,**g**) are shown as mean ± s.e.m (*n* = 33 thrombi from 4 mice). NS, not significant when compared by the Mann-Whitney statistical test (**d**,**g**).

(Fig. 4.4a). The initial velocity of fibrin formation with D-MARCKS ED treatment appeared to be reduced, nonetheless, the difference in fibrin formation lag time, or peak platelet or fibrin area values was not statistically significant (Fig. 4.4b-g and Supplementary Fig. B.7).

4.4 Discussion

In this work we have explored how small lipid-binding peptide and peptidomimetic probes can bind to activated, PS-exposing platelets and affect the blood coagulation pathway. We found that D-MARCKS ED could antagonize binding of a coagulation factor to PS, and that this activity inhibited the enzymatic activity of coagulation factor complex prothrombinase in the presence of a variety of PS-containing membranes. In whole blood, we observed dramatic inhibition of fibrin formation during contact activation pathway-driven coagulation in a microfluidic flow assay. *In vivo*, we observed D-MARCKS ED binding to platelets in the thrombus core, but we did not see a significant effect on fibrin formation. Coagulation initiation in the laser-induced microvascular injury model is more complex and believed to be driven by the exposure of tissue factor at the injury site.[128] While it is possible that therapeutic concentrations of D-MARCKS ED did not reach the *in vivo* injury site, the initiation of the coagulation cascade through tissue factor and factor VIIa could also explain the differences in fibrin formation inhibition between the *ex vivo* and *in vivo* models. For example, inhibition of the PS-dependent assembly of coagulation protein complex intrinsic tenase (factor VIIIa and factor IXa) by D-MARCKS ED would further slow fibrin

generation in models dependent on the contact activation pathway, but have lesser effect on coagulation initiated through the tissue factor pathway.

Interwoven with coagulation cascade initiation is the concurrent activation of platelets through interaction with collagen. This creates a positive feedback loop where activated platelet PS exposure serves as a cofactor for thrombin generation, and the generated thrombin further activates platelets. The combination of collagen or convulxin, both of which bind the platelet GPVI receptor, with thrombin is the strongest physiologic activator of platelets and the most effective driver of platelet-dependent thrombin generation.[129] Strong activation causes the platelet membrane to balloon and bleb and exposes a high amount of PS, while weaker activation, e.g., only thrombin, leaves the platelet membrane comparatively intact and causes less PS exposure.[129-131] Unsurprisingly, D-MARCKS ED demonstrated the greatest degree of binding to those platelets that were activated by the combination of convulxin and thrombin. Similar activation conditions occur when platelets encounter the immobilized collagen in the microfluidic flow assay, and this resulted in D-MARCKS ED labeling of almost all adherent platelets and the inhibition of fibrin formation. Conversely, in the laser-induced microvascular injury model, only a small portion of the platelets in the thrombus core are bound by D-MARCKS ED. These are platelets directly proximal to the injury site and the most likely to be exposed to subendothelial collagen. These results suggest that the more robust platelet activation response that occurs from GPVI activation is the most favorable for D-MARCKS ED binding and potential fibrin formation inhibition.

Peptides derived from the full length MARCKS protein sequence have previously been shown to have a number of biomodulary effects. The MANS peptide, made up of

the myristoylated N-terminal sequence of MARCKS, interferes with mucus hypersecretion, cancer metastasis, and proinflammatory cytokine expression.[132-135] MARCKS ED has been shown to reduce platelet serotonin release, block monocyte tissue factor initiated coagulation, and also interfere with proinflammatory cytokine expression.[135-138] These activities have been suggested to occur through various mechanisms, including altering cytoskeleton dynamics and blocking phosphorylation of endogenous MARCKS protein.[133,134,137] We have shown here that the MARCKS ED peptide binds to physiologically exposed PS and antagonizes coagulation factor binding and enzymatic activity. We did not observe MARCKS ED labeling or internalization by unstimulated platelets, suggesting the peptide does not quickly penetrate the plasma membrane. It is possible that some of the previously described biologic effects of MARCKS-derived peptides are also due to binding of peptides to the outer membrane surface. It is also worth noting that endogenous full length MARCKS is expressed across most tissues in the body, including platelets.[136,139] MARCKS associated to the inner leaflet of platelet plasma membranes may also be localized to the outer membrane surface during platelet activation, and could potentially have a physiologic role of modulating the platelet procoagulant response. Future investigation will be needed to explore this hypothesis.

Modulation of lipid protein interactions remains a challenging task and an essentially unexplored drug target.[140] In addition to the lock and key-like interaction of lipid head groups with proteins, the lipid membrane also has colligative physical properties, such as lipid packing, bilayer thickness, or surface charge, that change the environment of the interaction. PS binding proteins, such as annexin V and lactadherin,

have previously been shown to compete with coagulation factors for PS binding sites leading to inhibition of coagulation protein complex enzymatic activity.[141-144] Compared to these proteins, the MARCKS ED peptide is significantly smaller in size, more readily chemically modified during solid phase peptide synthesis, and, in the D-amino acid form, more stable to proteolysis and likely less immunogenic.[145] Perhaps most unique, the interaction between MARCKS ED and PS is not based on secondary or tertiary structure, but a primary structure-based interaction that occurs through a unique combination of peptide charge and hydrophobicity.[116-118] Our work here shows that this comparatively simple interaction motif is sufficient to inhibit the interaction between a coagulation factor and PS, and also specific enough to localize to a remote intravascular injury *in vivo*.

4.5 Methods

4.5.1 Investigational peptides synthesis

Peptides were synthesized using standard solid phase Fmoc chemistry on a Liberty microwave-assisted peptide synthesizer (CEM, Matthews, NC). Fluorescently labeled peptides were produced by conjugating NBD (4-chloro-7-nitrobenzo-2-oxa-1,3-diazole) via an aminohexanoic acid linker to the peptide N-terminus. Crude peptide was purified by a 1200 Series reverse phase HPLC (Agilent Technologies, Santa Clara, CA) using a semi-prep C18 column and characterized using either a Voyager DE-STR MALDI-TOF mass spectrometer (Applied Biosystems, Grand Island, NY) or a Synapt G2 HDMS Q-TOF mass spectrometer (Waters, Milford, MA) fitted with an electrospray

ionization source. HPLC peptide eluates were collected, lyophilized to dryness, and stored at -20 °C.

4.5.2 Serum stability

The serum stability of L- and D-MARCKS ED was measured as in a previously described protocol.[146] Briefly, 100 μg ml^{-1} L- or D-MARCKS ED was incubated at 37 °C in RPMI 1640 medium (Fisher Scientific, Pittsburgh, PA) supplemented with 25% (v/v) pooled normal human serum (Innovative Research, Novi, MI). At specific time points, the reaction was subsampled and a trichloroacetic acid solution was added to a final concentration of 5% (w/v). Each subsample mixture was cooled for 15 min at 4 °C, then centrifuged at 16,000g for 4 min to precipitate the serum proteins. The resulting supernatant was analyzed with a 1200 Series reverse phase HPLC (Agilent Technologies) using a semi-prep C18 column. Non-degraded peptide was quantified by setting the UV-visible HPLC detection to 480 nm and integrating the chromatogram peaks with retention times matching that of the whole peptide (39 to 40 min). Peaks at 480 nm are due to the absorbance NBD fluorophore label. Subsamples from serum mixtures without added MARCKS ED showed no peaks in this retention time range.

4.5.3 Synthetic liposome preparation

Synthetic liposomes were prepared using a modified version of a previously described method.[147] Briefly, chloroform suspended 1-palmitoyl-2-oleoyl-sn-glycero-3-phosphocholine (POPC), 1-palmitoyl-2-oleoyl-sn-glycero-3-phosphoethanolamine (POPE), and 1-palmitoyl-2-oleoyl-sn-glycero-3-phospho-L-serine (POPS) (Avanti Polar

Lipids, Alabaster, AL) were combined to form lipid mixtures of the described molar ratios. Lipid solutions were then dried to a thin film under a slow N_2 flow and vacuum desiccated for 1 hour. Lipid films were resuspended in HBS buffer (10 mM HEPES, 0.15 M NaCl, pH 7.4) containing 2 mM $CaCl_2$. Homogenously sized liposomes were formed by extruding the lipid solutions through polycarbonate track etched membranes (GE Healthcare, Pittsburgh, PA) with pore sizes of 30, 100, and 400 nm using a LiposoFast FL-50 extruder (Avestin, Ottawa, Canada). Extruded liposome sizes were characterized by nanoparticle tracking analyses using a NanoSight LM14 (Malvern Instruments, Malvern, United Kingdom).

4.5.4 Surface plasmon resonance

The effect of D-MARCKS ED on FXa binding to phosphatidylserine was assessed by SPR with Biacore 3000 (GE Healthcare) and 404pi (BiOptix, Boulder, CO) instruments. All experiments were run with HPP (alkyl-SAM) sensor chips (XanTec, Duesseldorf, Germany) in HBS running buffer containing 2 mM $CaCl_2$. 500 μM liposome solutions were prepared and extruded through 100 nm pore size polycarbonate membranes as described above. After thorough flushing of the SPR instrument flow system and needles with 40 mM octyl glucoside (Sigma-Aldrich, St. Louis, MO) and running buffer, 150 μl of liposome solution was injected at a flow rate of 5 μl min^{-1} to coat the HPP sensor chip surface. Membrane surface formation was verified by injecting 50 μl of 0.1 mg ml^{-1} BSA at a flow rate of 5 μl min^{-1}, where accumulation of less than 100 response units (RU) of BSA indicated formation of a complete self-assembled lipid monolayer.[148] Liposomes composed of

POPC/POPS/POPE at a 3/5/2 molar ratio were used to form the experimental flow cell. The control flow cell, used for reference correcting, was formed with liposomes composed of only POPC. A flow cell coated only with BSA was used to verify that the peptides and proteins did not associate to the adsorbed BSA.

All subsequent injections were done at a flow rate of 60 μl min^{-1}. Each competition experiment followed the same injection series; a 90 μl injection of either running buffer or 1 μM D-MARCKS ED, C2BL3-L, or annexin V (BioVision, Milpitas, CA), a 160 sec wait, followed by a 50 μl injection of 50 nM FXa (Haematologic Technologies, Essex Junction, VT). Complete regeneration of the membrane surface after injection of FXa was achieved with 10 μl of 2.5 M NaCl. Regeneration of the membrane surface after injection of D-MARCKS ED was not possible without using more stringent regeneration conditions that also partially removed the lipid surface. We therefore completely stripped the surface with 40 mM octyl glucoside and formed the membrane surface anew after each injection series of investigational peptide or protein. The absolute FXa binding response varied with each new membrane surface. As a result, investigational peptide or protein FXa binding inhibition was only calculated as compared to the uninhibited FXa binding response over the same formed membrane surface. Sensograms were analyzed with Scrubber2 (BioLogic Software, Campbell, Australia) using either reference correction to the only POPC surface to show the complete injection sequence (Fig. 4.1c), or a double referencing procedure for analysis of FXa response (Fig. 4.1d and Supplementary Fig. B.1). Double referencing corrects the sensogram relative to both the response of the control flow cell and to buffer blank injections over the experimental flow cell.[149] In the case of these experiments, this

corrects for the change in surface response to the buffer when it is pretreated with an investigational peptide or protein. The maximum SPR response was determined by averaging over the last 5 sec of the FXa association in the double referencing corrected sensograms.

4.5.5 Whole blood collection and platelet preparation

Human whole blood was collected from healthy volunteers, as permitted by the Institutional Review Board at the University of Colorado Anschutz Medical Campus. Whole blood was collected by venipuncture into 3.2% sodium citrate. Washed platelets were prepared from whole blood collected by venipuncture into 3.8% sodium citrate and acid-citrate-dextrose (ACD). Platelet-rich plasma (PRP) was prepared by centrifugation of whole blood at 200*g* for 20 min. Platelets were isolated from the PRP by centrifugation at 1000*g* for 10 min with 0.1 μg ml^{-1} prostacyclin (PGI_2) (Sigma-Aldrich). The resulting pellet was resuspended with modified Tyrode's buffer (129 mM NaCl, 20 mM HEPES, 12 mM $NaHCO_3$, 2.9 mM KCl, 1.0 mM $MgCl_2$, 0.34 mM Na_2HPO_4, 5 mM glucose, pH 7.3), ACD, and 0.1 μg ml^{-1} PGI_2. Platelets were then washed by re-pelleting at 1000*g* for 10 min and re-suspending with modified Tyrode's buffer.

4.5.6 Cell culture and exosome isolation

Biologic exosomes were isolated from MDA-MB-231 human breast cancer cells. Cells were grown to approximately 80% confluency on a 10 cm tissue culture dish. Culture media was then replaced with unsupplemented Dulbecco's modified Eagle's medium (Life Technologies, Grand Island, NY) and incubated for 2 days in a 1%

oxygen environment. After incubation, exosomes were isolated from the cell media using Exoquick-TC (System Biosciences, Mountain View, CA) following the manufacturer's standard protocol. The concentration ($2.62 \pm 0.65 \times 10^{11}$ particles ml^{-1}) and mean size (187 ± 66 nm) of the isolated exosomes was determined by nanoparticle tracking analyses using a NanoSight LM14 (Malvern Instruments).

4.5.7 Prothrombinase assay

Effects on coagulation factor enzymatic activity were determined using a modification of a previously described prothrombinase assay.[129,150] Washed human platelets (8×10^5 reaction^{-1}) were incubated at 37 °C with either a buffer blank or 375 ng ml^{-1} convulxin (Centerchem, Norwalk, CT) and 5.0 nM thrombin (Haematologic Technologies) in modified Tyrode's buffer containing 2.9 mM $CaCl_2$ and 0.05% wt vol^{-1} fatty acid-free bovine serum albumin (BSA). After 7 min, 1 μM investigational peptide or protein, or a buffer blank, was added, followed 3 min later by bovine FXa (3 nM) and FVa (6 nM) (Haematologic Technologies). 1 min later, 4 μM bovine prothrombin (Enzyme Research Laboratories, South Bend, IN) was added. After 4 min, the reaction mixture was subsampled into a Tris EDTA stop buffer (0.05 M Tris-HCl, 0.12 M NaCl, 2 mM EDTA, pH 7.5). The V_{max} of the generated thrombin was determined chromogenically by adding 0.5 mM S-2238 substrate (DiaPharma, West Chester, OH) and measuring changes in absorbance at 405 nm over time using a Synergy 2 microplate reader (BioTek, Winooski, VT). Effects on the prothrombinase activity of liposomes (100 nM POPC/POPS at a 19/1 molar ratio) and MDA-MB-231 exosomes (7×10^7 reaction^{-1}) were examined with identical conditions omitting the addition of

convulxin and thrombin. At these concentrations, uninhibited thrombin generation by the liposomes and exosomes approximately matched that of the activated platelets. The half maximal inhibitory concentration (IC_{50}) was fit by plotting [peptide] as log values and fitting with a nonlinear least-squares best-fit analysis using the equation prothrombinase $V_{max} = V_{max}^{min} + (V_{max}^{max} - V_{max}^{min}) / (1 + 10^{[Peptide] - logIC50})$.

4.5.8 Flow cytometry

Washed platelets were obtained from the whole blood as described above. The platelets were resuspended in modified Tyrode's buffer containing 2 mM $CaCl_2$, counted, and diluted to $2x10^4$ platelets μL^{-1}. Platelets were stimulated with either 1 IU ml^{-1} thrombin (Chrono-log, Havertown, PA), 250 ng ml^{-1} convulxin (Centerchem), 1 IU ml^{-1} thrombin and 250 ng ml^{-1} convulxin, or left unstimulated for 10 min at room temperature. Platelets were then incubated for 30 min with Brilliant Violet 605 anti-human CD62P antibody (BioLegend, San Diego, CA), Cy5 annexin V (BD Biosciences, San Jose, CA), and 1 μM NBD labeled D-MARCKS ED peptide. The samples were then immediately fixed in 1% paraformaldehyde, diluted, and analyzed on a MoFlo Astrios EQ flow cytometer (Beckman Coulter, Brea, CA) with appropriate color compensation.

4.5.9 Whole blood microfluidic flow assay

Effects on whole blood platelet activation and accumulation, as well as fibrin formation, were examined using a modification of a previously described microfluidic flow assay.[126] A custom polydimethylsiloxane microfluidic flow device containing four

channels, each with a height of 100 μm and width of 500 μm, was vacuum mounted to a glass slide patterned with a type I fibrillar collagen strip (Chrono-log). The microfluidic flow device channels were oriented perpendicular to the patterned collagen strip, resulting in a 50 μm patch of collagen across the width of each channel. Whole blood was labeled with a Pacific Blue anti-human CD41 antibody (BioLegend) for 10 min, followed by the addition of 30 μg ml^{-1} Alexa Fluor 647 human plasma fibrinogen conjugate (Life Technologies) and either 1 μM NBD labeled investigational peptide, 1 μM annexin V (BioVision), or 15 USP ml^{-1} heparin. Immediately before the assay, the whole blood mixture was recalcified to 7.5 mM $CaCl_2$. The whole blood was then pulled through the device channels for 10 min at wall shear rate 100 s^{-1} using a PhD Ultra syringe pump (Harvard Apparatus, Holliston, MA). Platelet aggregation, fibrin formation, and peptide accumulation were captured in real time by epifluorescence microscopy using an IX81 inverted microscope with a 40x objective (Olympus Equipment, Center Valley, PA) equipped with an Orca-R2 16-bit CCD camera (Hamamatsu, Bridgewater, NJ). Fluorescence intensities and platelet surface area coverages were measured using ImageJ (NIH, Bethesda, MD).

4.5.10 Electron microscopy

Thrombi formed in the microfluidic flow assay were prepared as previously described and imaged with a JSM-7000F scanning electron microscope (JEOL, Peabody, MA) at a working distance of 6 mm and accelerating voltage of 1.5 kV.[151]

4.5.11 Intravital microscopy

This procedure was performed essentially as described previously, and approved by the Institutional Animal Care and Use Committee of the University of Pennsylvania.[127] Briefly, male mice 8-12 weeks of age were anesthetized via intraperitoneal injection of ketamine/xylazine/acepromazine (100/10/2 mg kg^{-1}). A cannula was introduced into the jugular vein for delivery of fluorescently labeled antibodies and peptides, and additional anesthetic as needed. The cremaster muscle was exteriorized, cleaned of connective tissue, opened and spread flat on the glass coverslip of a custom built chamber for viewing by intravital microscopy. The cremaster preparation was continuously superfused with bicarbonate buffer warmed to 36.5 °C and bubbled with 95% N_2 / 5% CO_2. The cremaster microcirculation was visualized using a BX61WI upright microscope with a 60X (0.9 NA) water immersion objective (Olympus Equipment), coupled to a CSU-X1 spinning disk confocal scanner (Yokogawa, Japan). Diode pumped solid state lasers (488 nm, 568 nm, 640 nm) with AOTF control (LaserStack, Intelligent Imaging Innovations, Denver, CO) were used as the fluorescence excitation light source. Confocal fluorescence images were acquired using an Evolve EM-CCD digital camera (Photometrics, Tucson, AZ). The microscope, confocal scanner, lasers and camera were all controlled and synchronized using SlideBook 6.0 image acquisition and analysis software (Intelligent Imaging Innovations). 30-40 μm diameter arterioles with unperturbed blood flow were selected for study. Vascular injury was induced with a pulsed nitrogen dye laser at 440 nm (NL100, Stanford Research Systems, Sunnyvale, CA) focused on the vessel wall by the microscope objective. The laser power was set to 55-65% and the laser fired at the

vessel wall until a small number of red blood cells exited the lumen of the vessel (1-10 laser pulses). Anti-CD41 $F(ab)_2$ fragments (0.12 μg g^{-1}; clone MWReg30, BD Biosciences), and anti-fibrin antibody (0.2 μg g^{-1}; clone 59D8) were infused intravenously via the jugular vein to label platelets and fibrin, respectively. Antibodies were labeled with Alexa Fluor 568 and 647 monoclonal antibody labeling kits according to the manufacturers instructions (Life Technologies). NBD labeled D-MARCKS ED or C2BL3-L peptide (5 mg kg^{-1}) were infused at the same time as the antibodies and imaged in the 488 nm excitation channel.

4.5.12 Statistical analysis

All plots and statistical analyses were performed with Prism 6 (GraphPad, La Jolla, CA). Results are presented as means ± s.d. unless otherwise noted. Comparisons between two groups were performed with either two tailed Student's *t*-tests or Mann-Whitney tests. Multiple comparisons between more than two normally distributed groups were performed with one-way analysis of variance (ANOVA) with Dunnett's *post hoc* test. For all cases, $P < 0.05$ were considered to be significant.

Chapter 5

Conclusions and future directions

5.1 Conclusions

In this work, I have examined the importance of the lipid membranes of extracellular vesicles and platelets. I have shown that basic properties of these membranes, such as lipid composition or membrane shape, can modulate the biophysical interactions of lipids within the membrane, between different membrane surfaces, and of proteins to the membrane surface.

I first highlighted the fundamental biology of extracellular vesicles and addressed how basic biophysical properties, e.g., size dependent diffusion coefficient or lipid packing, can be used for detection and targeting of these vesicles.

Next, I studied the relationship between membrane shape and molecular interactions of lipids within the membrane utilizing all-atom molecular dynamics simulations. In previous molecular dynamics simulations, membrane curvature has been induced through interactions of the membrane with a curvature inducing protein.[81] This results in a membrane with a single radius of curvature that cannot stably exist in the absence of the protein or a physical constraint. I demonstrated that increasing the

lateral density of a bilayer lipid membrane can induce the membrane to form a curved shape. The radius of the curvature of these membranes is proportional to the amount the area per lipid is perturbed from its equilibrium value. This method provides a means to generate membranes in molecular dynamic simulations in a range of shapes that recreate important biophysical properties of curved membranes, such as lipid packing defects in the membrane surface.

To investigate the effect of curvature on membrane-membrane interactions, I adapted theoretical models of membrane forces to examine the membrane-membrane interactions of extracellular vesicles. I used these models to address fundamental questions about how extracellular vesicles signal. My theoretical estimates suggested that smaller extracellular vesicles (exosomes), are more likely to signal via endocytosis, while larger extracellular vesicles (microvesicles), are more likely to interact via a vesicle-ligand cell-receptor interaction. Additionally, I proposed a potential mechanistic explanation for the role of polymer depletion forces in extracellular vesicle isolation and purification.

Finally, I examined experimentally how blocking platelet lipids can influence the assembly and enzymatic activity of lipid dependent coagulation protein complexes. When platelets become activated during hemostasis or thrombosis, they undergo changes in membrane shape and expose the lipid phosphatidylserine on their outer membrane leaflet. Using peptides derived from the effector domain of the protein MARCKS, I showed that a peptide can target phosphatidylserine exposed on activated platelets and thereby inhibit the platelet procoagulant response. I found that this inhibition occurs through antagonizing the binding and assembly of enzymatically active

coagulation protein complexes on platelet phosphatidylserine. Using a whole blood microfluidic flow assay that recapitulates physiologic thrombus formation conditions, I found that the MARCKS peptides could bind platelets in whole blood and inhibit the formation of fibrin, the end product of the coagulation cascade. Although I did not observe similar fibrin formation inhibition *in vivo*, I did find that the D-MARCKS ED peptide could travel through the circulatory system and bind to activated platelets in the core of a remote thrombus.

Considered together, this work further defines the membrane not just as a container to localize contents, or as a holder of transmembrane proteins, but as a significant driver of the biologic processes of extracellular vesicles and platelets through the properties of membrane shape and lipid composition.

5.2 Future directions

5.2.1 Molecular dynamics simulations of proteins with curved membrane

In Chapter 2, I demonstrated a new method for inducing membrane curvature in molecular dynamics simulations. These curved membranes should be validated by simulating the membranes with known curvature binding peptides or proteins, e.g., endophilin or MARCKS ED.[57, 81] Observation of the binding of these proteins to the membranes through previously described insertion of hydrophobic residues into lipid packing defects is a necessary step in confirming that the lipid membrane environment mimics that found in other experiments.[81,120] The membranes could then be used to design and test *in silico* new membrane curvature binding peptides or proteins using

umbrella sampling, or as a means to study the interactions of existing curvature sensing proteins and peptides with curved membranes at molecular detail.

5.2.2 Experimental studies of extracellular vesicles interacting with supported lipid bilayers

The theoretical estimates of extracellular vesicle interaction energies and bond lifetimes introduced in Chapter 3 should also be confirmed experimentally. Work is currently ongoing to measure single liposome and biologic exosome binding events to supported bilayer membranes using total internal reflection fluorescence (TIRF) microscopy. The intrinsic bond lifetimes found in these experiments could be compared to the theoretical estimates, and used to refine the current model. Variation of the lipid composition of the synthetic elements (the liposomes and supported bilayer) could also be used to further characterize the contribution of electrostatics to the interactions.

5.2.3 Further *in vivo* coagulation model studies with MARCKS ED

From a biotechnology development standpoint, the central remaining question with MARCKS ED is application. Previous work has shown the potential of MARCKS ED to label extracellular vesicles.[57] However, applications of this property to biomarker or biodelivery functions have yet to be proven. In the context of platelets and blood coagulation, I found that D-MARCKS ED was a potent inhibitor of the phosphatidylserine dependent coagulation protein complex prothrombinase *in vitro*, but did not observe similar potency *in vivo*. It remains an outstanding question whether the

lack of fibrin formation inhibition seen *in vivo* was due to insufficient localized concentration of D-MARCKS ED at the injury site, or represents a fundamental difference in the physiologic mechanism of clot formation in the intravital laser induced injury model. These questions could be clarified by future *in vivo* experiments using a higher dose of D-MARCKS ED, as well as *in vivo* models where coagulation is more likely to be induced through the contact activation pathway, rather than the tissue factor pathway, e.g., femoral artery injuries.

Additionally, conjugation of a near-infrared fluorescent dye to MARCKS ED could enable the use of *in vivo* fluorescence imaging methods to help determine if MARCKS ED localizes to other sites, most importantly the blood filtering organs (kidney, spleen, or liver). Such localization of MARCKS ED may reduce the effective concentration of the peptide at the injury site. Chemical modifications of MARCKS ED that increase the ease of synthesis, or potency of the peptide as a phosphatidylserine antagonist, should also be explored. Synthesis and studies of variations of the MARCKS ED peptide, such as truncation into smaller fragments or incorporation of an unnatural peptide backbone, are currently ongoing in the Yin lab.

Finally, the question remains if the antagonism of phosphatidylserine by full length MARCKS has a biologic function. For example, does endogenously expressed MARCKS protein in platelets find a way to the outer membrane leaflet during platelet activation and tamper the platelet procoagulant response? To obtain platelets that do not contain MARCKS, a MARCKS knockout mouse (lethal in the homozygous form) or cultured megakaryocytes with knocked down, or knocked out, MARCKS expression

would be needed.[56] Experiments similar to those presented in Chapter 4 could then be repeated with the MARCKS deficient platelets.

Bibliography

1. Rak, J. Microparticles in Cancer. *Semin. Thromb. Hemost.* **36,** 888–906 (2010).

2. Kahlert, C. & Kalluri, R. Exosomes in tumor microenvironment influence cancer progression and metastasis. *J. Mol. Med.* **91,** 431–437 (2013).

3. El-Hefnawy, T. Characterization of Amplifiable, Circulating RNA in Plasma and Its Potential as a Tool for Cancer Diagnostics. *Clin. Chem.* **50,** 564–573 (2004).

4. Camussi, G., Deregibus, M. C., Bruno, S., Cantaluppi, V. & Biancone, L. Exosomes/microvesicles as a mechanism ofcell-to-cell communication. *Kidney Int.* **78,** 838–848 (2010).

5. Lösche, W., Scholz, T., Temmler, U., Oberle, V. & Claus, R. A. Platelet-derived microvesicles transfer tissue factor to monocytes but not to neutrophils. *Platelets* **15,** 109–115 (2004).

6. EL Andaloussi, S., Mäger, I., Breakefield, X. O. & Wood, M. J. A. Extracellular vesicles: biology and emerging therapeutic opportunities. *Nat. Rev. Drug Discov.* **12,** 347–357 (2013).

7. Raposo, G. & Stoorvogel, W. Extracellular vesicles: exosomes, microvesicles, and friends. *J. Cell Biol.* **200,** 373–383 (2013).

8. Harding, C. V., Heuser, J. E. & Stahl, P. D. Exosomes: Looking back three decades and into the future. *J. Cell Biol.* **200,** 367–371 (2013).

9. Vlassov, A. V., Magdaleno, S., Setterquist, R. & Conrad, R. Exosomes: current knowledge of their composition, biological functions, and diagnostic and therapeutic potentials. *Biochim. Biophys. Acta* **1820,** 940–948 (2012).

10. György, B. *et al.* Membrane vesicles, current state-of-the-art: emerging role of extracellular vesicles. *Cell. Mol. Life Sci.* **68,** 2667–2688 (2011).

11. Tetta, C., Ghigo, E., Silengo, L., Deregibus, M.-C. & Camussi, G. Extracellular vesicles as an emerging mechanism of cell-to-cell communication. *Endocrine* **44,** 11–19 (2013).

12. Couzin, J. Cell biology: The ins and outs of exosomes. *Science* **308,** 1862–1863 (2005).

13. Lacroix, R., Dubois, C., Leroyer, A. S., Sabatier, F. & Dignat-George, F. Revisited role of microparticles in arterial and venous thrombosis. *J. Thromb. Haemost.* **11,** 24–35 (2013).

14. Geddings, J. E. & Mackman, N. Tumor-derived tissue factor-positive microparticles and venous thrombosis in cancer patients. *Blood* **122,** 1873–1880 (2013).

15. Al-Nedawi, K., Meehan, B. & Rak, J. Microvesicles: messengers and mediators of tumor progression. *Cell Cycle* **8,** 2014–2018 (2009).

16. Scott, S., Pendlebury, S. A. & Green, C. Lipid organization in erythrocyte membrane microvesicles. *Biochem. J.* **224,** 285–290 (1984).

17. Hugel, B. Membrane Microparticles: Two Sides of the Coin. *Physiology* **20,** 22–27 (2005).

18. Heijnen, H. F., Schiel, A. E., Fijnheer, R., Geuze, H. J. & Sixma, J. J. Activated platelets release two types of membrane vesicles: microvesicles by surface shedding and exosomes derived from exocytosis of multivesicular bodies and alpha-granules. *Blood* **94,** 3791–3799 (1999).

19. Harding, C., Heuser, J. & Stahl, P. Receptor-mediated endocytosis of transferrin and recycling of the transferrin receptor in rat reticulocytes. *J. Cell Biol.* **97,** 329–339 (1983).

20. Savina, A., Furlán, M., Vidal, M. & Colombo, M. I. Exosome release is regulated by a calcium-dependent mechanism in K562 cells. *J. Biol. Chem.* **278,** 20083–20090 (2003).

21. Laulagnier, K. *et al.* Mast cell-and dendritic cell-derived exosomes display a specific lipid composition and an unusual membrane organization. *Biochem. J.* **380,** 1–11 (2004).

22. Trajkovic, K. *et al.* Ceramide triggers budding of exosome vesicles into multivesicular endosomes. *Science* **319,** 1244–1247 (2008).

23. Denzer, K., Kleijmeer, M. J., Heijnen, H. F., Stoorvogel, W. & Geuze, H. J. Exosome: from internal vesicle of the multivesicular body to intercellular signaling device. *J. Cell Sci.* **113 Pt 19,** 3365–3374 (2000).

24. Théry, C., Amigorena, S., Raposo, G. & Clayton, A. Isolation and characterization of exosomes from cell culture supernatants and biological

fluids. *Curr. Protoc. Cell Biol.* **Chapter 3,** Unit 3.22 (2006).

25. Zimmerberg, J. & Kozlov, M. M. How proteins produce cellular membrane curvature. *Nat. Rev. Mol. Cell Bio.* **7,** 9–19 (2005).

26. Lyman, E., Cui, H. & Voth, G. A. Water under the BAR. *Biophys. J.* **99,** 1783–1790 (2010).

27. de Jesus, A. J., Kastelowitz, N. & Yin, H. Changes in lipid density induce membrane curvature. *RSC Adv.* **3,** 13622 (2013).

28. Hatzakis, N. S. *et al.* How curved membranes recruit amphipathic helices and protein anchoring motifs. *Nat. Chem. Biol.* **5,** 835–841 (2009).

29. Suetsugu, A. *et al.* Imaging exosome transfer from breast cancer cells to stroma at metastatic sites in orthotopic nude mouse models. *Adv. Drug Deliver. Rev.* 1–8 (2012). doi:10.1016/j.addr.2012.08.007

30. Balaj, L. *et al.* Tumour microvesicles contain retrotransposon elements and amplified oncogene sequences. *Nat. Commun.* **2,** 180–9 (2011).

31. Hood, J. L., San, R. S. & Wickline, S. A. Exosomes Released by Melanoma Cells Prepare Sentinel Lymph Nodes for Tumor Metastasis. *Cancer Res.* **71,** 3792–3801 (2011).

32. Huber, V. *et al.* Human Colorectal Cancer Cells Induce T-Cell Death Through Release of Proapoptotic Microvesicles: Role in Immune Escape. *Gastroenterology* **128,** 1796–1804 (2005).

33. Bryant, R. J. *et al.* Changes in circulating microRNA levels associated with prostate cancer. *Brit. J. Cancer* **106,** 768–774 (2012).

34. Rabinowits, G., Gerçel-Taylor, C., Day, J. M., Taylor, D. D. & Kloecker, G. H. Exosomal MicroRNA: A Diagnostic Marker for Lung Cancer. *Clin. Lung Cancer* **10,** 42–46 (2011).

35. Logozzi, M. *et al.* High Levels of Exosomes Expressing CD63 and Caveolin-1 in Plasma of Melanoma Patients. *PLoS ONE* **4,** e5219 (2009).

36. Kim, H. K. *et al.* Elevated levels of circulating platelet microparticles, VEGF, IL-6 and RANTES in patients with gastric cancer: possible role of a metastasis predictor. *Eur. J. Cancer* **39,** 184–191 (2003).

37. van der Pol, E. *et al.* Optical and non-optical methods for detection and characterization of microparticles and exosomes. *J. Thromb. Haemost.* **8,** 2596–2607 (2010).

38. Dragovic, R. A. *et al.* Sizing and phenotyping of cellular vesicles using Nanoparticle Tracking Analysis. *Nanomedicine* **7,** 780–788 (2011).

39. Perez-Pujol, S., Marker, P. H. & Key, N. S. Platelet microparticles are heterogeneous and highly dependent on the activation mechanism: Studies using a new digital flow cytometer. *Cytometry* **71A,** 38–45 (2007).

40. van der Vlist, E. J., Nolte-'t Hoen, E. N. M., Stoorvogel, W., Arkesteijn, G. J. A. & Wauben, M. H. M. Fluorescent labeling of nano-sized vesicles released by cells and subsequent quantitative and qualitative analysis by high-resolution flow cytometry. *Nat Protoc* **7,** 1311–1326 (2012).

41. Lawrie, A. S., Albanyan, A., Cardigan, R. A., Mackie, I. J. & Harrison, P. Microparticle sizing by dynamic light scattering in fresh-frozen plasma. *Vox Sang.* **96,** 206–212 (2009).

42. Oosthuyzen, W. *et al.* Quantification of human urinary exosomes by nanoparticle tracking analysis. *J. Physiol.* **591,** 5833–5842 (2013).

43. Howard, J. *Mechanics of Motor Proteins & the Cytoskeleton*. (Sinauer Associates Incorporated, 2001).

44. Cocucci, E., Racchetti, G. & Meldolesi, J. Shedding microvesicles: artefacts no more. *Trends Cell Biol.* **19,** 43–51 (2009).

45. Caby, M. P. Exosomal-like vesicles are present in human blood plasma. *Int. Immunol.* **17,** 879–887 (2005).

46. Lee, T. H. *et al.* Microvesicles as mediators of intercellular communication in cancer—the emerging science of cellular ‘debris’. *Semin. Immunopathol.* **33,** 455–467 (2011).

47. Li, Y., Zhang, Y., Qiu, F. & Qiu, Z. Proteomic identification of exosomal LRG1: A potential urinary biomarker for detecting NSCLC. *Electrophoresis* **32,** 1976–1983 (2011).

48. Jørgensen, M. *et al.* Extracellular Vesicle (EV) Array: microarray capturing of exosomes and other extracellular vesicles for multiplexed phenotyping. *J. Extracell. Vesicles* **2,** 20920 (2013).

49. Bigay, J. & Antonny, B. Curvature, Lipid Packing, and Electrostatics of Membrane Organelles: Defining Cellular Territories in Determining Specificity. *Dev. Cell* **23,** 886–895 (2012).

50. Antonny, B. Mechanisms of Membrane Curvature Sensing. *Annu. Rev.*

Biochem. **80,** 101–123 (2011).

51. Cui, Q., Zhang, L., Wu, Z. & Yethiraj, A. Generation and sensing of membrane curvature: Where materials science and biophysics meet. *Curr. Opin. Solid State Mater. Sci.* **17,** 164–174 (2013).

52. Lemmon, M. A. Membrane recognition by phospholipid-binding domains. *Nat. Rev. Mol. Cell Bio.* **9,** 99–111 (2008).

53. van Engeland, M., Nieland, L. J., Ramaekers, F. C., Schutte, B. & Reutelingsperger, C. P. Annexin V-affinity assay: a review on an apoptosis detection system based on phosphatidylserine exposure. *Cytometry* **31,** 1–9 (1998).

54. Grant, R. *et al.* A filtration-based protocol to isolate human Plasma Membrane-derived Vesicles and exosomes from blood plasma. *J. Immunol. Methods* **371,** 143–151 (2011).

55. Keller, S. *et al.* Systemic presence and tumor-growth promoting effect of ovarian carcinoma released exosomes. *Cancer Lett.* **278,** 73–81 (2009).

56. Arbuzova, A., Schmitz, A. A. P. & Vergères, G. Cross-talk unfolded: MARCKS proteins. *Biochem. J.* **362,** 1–12 (2002).

57. Morton, L. A. *et al.* MARCKS-ED peptide as a curvature and lipid sensor. *ACS Chem. Biol.* **8,** 218–225 (2013).

58. Saludes, J. P. *et al.* Detection of highly curved membrane surfaces using a cyclic peptide derived from synaptotagmin-I. *ACS Chem. Biol.* **7,** 1629–1635 (2012).

59. Saludes, J. P. *et al.* Multivalency amplifies the selection and affinity of bradykinin-derived peptides for lipid nanovesicles. *Mol. BioSyst.* **9,** 2005 (2013).

60. Madsen, K. L., Bhatia, V. K., Gether, U. & Stamou, D. BAR domains, amphipathic helices and membrane-anchored proteins use the same mechanism to sense membrane curvature. *FEBS Lett.* **584,** 1848–1855 (2010).

61. Beck, R. *et al.* Membrane curvature induced by Arf1-GTP is essential for vesicle formation. *Proc. Natl. Acad. Sci. U.S.A.* **105,** 11731–11736 (2008).

62. Drin, G. *et al.* A general amphipathic α-helical motif for sensing membrane curvature. *Nat. Struct. Mol. Biol.* **14,** 138–146 (2007).

63. Pranke, I. M. *et al.* α-Synuclein and ALPS motifs are membrane curvature sensors whose contrasting chemistry mediates selective vesicle binding. *J. Cell*

Biol. **194,** 89–103 (2011).

64. Devaux, P. F., Herrmann, A., Ohlwein, N. & Kozlov, M. M. How lipid flippases can modulate membrane structure. *BBA - Biomembranes* **1778,** 1591–1600 (2008).

65. Staykova, M., Holmes, D. P., Read, C. & Stone, H. A. Mechanics of surface area regulation in cells examined with confined lipid membranes. *Proc. Natl. Acad. Sci. U.S.A.* **108,** 9084–9088 (2011).

66. van Meer, G., Voelker, D. R. & Feigenson, G. W. Membrane lipids: where they are and how they behave. *Nat. Rev. Mol. Cell Bio.* **9,** 112–124 (2008).

67. Daleke, D. L. Phospholipid Flippases. *J. Biol. Chem.* **282,** 821–825 (2006).

68. Fuller, N. & Rand, R. P. The influence of lysolipids on the spontaneous curvature and bending elasticity of phospholipid membranes. *Biophys. J.* **81,** 243–254 (2001).

69. Markvoort, A. J., van Santen, R. A. & Hilbers, P. A. J. Vesicle Shapes from Molecular Dynamics Simulations. *J. Phys. Chem. B* **110,** 22780–22785 (2006).

70. Yin, Y., Arkhipov, A. & Schulten, K. Simulations of Membrane Tubulation by Lattices of Amphiphysin N-BAR Domains. *Structure* **17,** 882–892 (2009).

71. Arkhipov, A., Yin, Y. & Schulten, K. Four-Scale Description of Membrane Sculpting by BAR Domains. *Biophys. J.* **95,** 2806–2821 (2008).

72. Cui, H., Ayton, G. S. & Voth, G. A. Membrane Binding by the Endophilin N-BAR Domain. *Biophys. J.* **97,** 2746–2753 (2009).

73. Hsin, J. *et al.* Protein-Induced Membrane Curvature Investigated through Molecular Dynamics Flexible Fitting. *Biophys. J.* **97,** 321–329 (2009).

74. Blood, P. D. & Voth, G. A. Direct observation of Bin/amphiphysin/Rvs (BAR) domain-induced membrane curvature by means of molecular dynamics simulations. *Proc. Natl. Acad. Sci. U.S.A.* **103,** 15068–15072 (2006).

75. Meyer, G. R., Gullingsrud, J., Schulten, K. & Martinac, B. Molecular Dynamics Study of MscL Interactions with a Curved Lipid Bilayer. *Biophys. J.* **91,** 1630–1637 (2006).

76. Yoo, J. & Cui, Q. Curvature Generation and Pressure Profile Modulation in Membrane by Lysolipids: Insights from Coarse-Grained Simulations. *Biophys. J.* **97,** 2267–2276 (2009).

77. Kandt, C., Ash, W. L. & Tieleman, P. D. Setting up and running molecular dynamics simulations of membrane proteins. *Methods* **41,** 475–488 (2007).

78. Rothman, J. E. & Lenard, J. Membrane asymmetry. *Science* **195,** 743–753 (1977).

79. Jo, S., Lim, J. B., Klauda, J. B. & Im, W. CHARMM-GUI Membrane Builder for Mixed Bilayers and Its Application to Yeast Membranes. *Biophys. J.* **97,** 50–58 (2009).

80. Wang, H. *et al.* Bilayer Edge and Curvature Effects on Partitioning of Lipids by Tail Length: Atomistic Simulations. *Biophys. J.* **95,** 2647–2657 (2008).

81. Cui, H., Lyman, E. & Voth, G. A. Mechanism of Membrane Curvature Sensing by Amphipathic Helix Containing Proteins. *Biophys. J.* **100,** 1271–1279 (2011).

82. Brooks, B. R. *et al.* CHARMM: A Program for Macromolecular Energy, Minimization, and Dynamics Calculations. *J. Comput. Chem.* **4,** 187–217 (1983).

83. Klauda, J. B. *et al.* Update of the CHARMM all-atom additive force field for lipids: validation on six lipid types. *J. Phys. Chem. B* **114,** 7830–7843 (2010).

84. Jorgensen, W. L., Chandrasekhar, J., Madura, J. D., Impey, R. W. & Klein, M. L. Comparison of simple potential functions for simulating liquid water. *J. Chem. Phys.* **79,** (1983).

85. Ryckaert, J. P., Ciccotti, G. & Berendsen, H. Numerical integration of the cartesian equations of motion of a system with constraints: molecular dynamics of n-alkanes. *J. Comput. Phys.* **23,** 327–341 (1977).

86. Darden, T., York, D. & Pedersen, L. Particle mesh Ewald: An N·log (N) method for Ewald sums in large systems. *J. Chem. Phys.* **98,** 10089 (1993).

87. Nosé, S. A unified formulation of the constant temperature molecular dynamics methods. *J. Chem. Phys.* **81,** 511 (1984).

88. Hoover, W. Canonical dynamics: Equilibrium phase-space distributions. *Phys. Rev., A* **31,** 1695–1697 (1985).

89. Feller, S. E., Zhang, Y., Pastor, R. W. & Brooks, B. R. Constant pressure molecular dynamics simulation: the Langevin piston method. *J. Chem. Phys.* **103,** 4613 (1995).

90. Lee, B. & Richards, F. M. The interpretation of protein structures: estimation of static accessibility. *J. Mol. Biol.* **55,** 379–400 (1971).

91. Leckband, D. & Israelachvili, J. Intermolecular forces in biology. *Quart. Rev. Biophys.* **34,** 105 (2001).

92. Israelachvili, J. N. Strength of van der Waals attraction between lipid bilayers. *Langmuir* **10,** 3369–3370 (1994).

93. Israelachvili, J. N. & Wennerstroem, H. Hydration or steric forces between amphiphilic surfaces? *Langmuir* **6,** 873–876 (1990).

94. Helfrich, W. & Servuss, R.-M. Undulations, steric interaction and cohesion of fluid membranes. *Il Nuovo Cimento D* **3,** 137–151 (1984).

95. Michel, R. & Gradzielski, M. Experimental Aspects of Colloidal Interactions in Mixed Systems of Liposome and Inorganic Nanoparticle and Their Applications. *IJMS* **13,** 11610–11642 (2012).

96. Gao, Y. *et al.* Single reconstituted neuronal SNARE complexes zipper in three distinct stages. *Science Signaling* **337,** 1340 (2012).

97. Armen, R. S., Uitto, O. D. & Feller, S. E. Phospholipid Component Volumes: Determination and Application to Bilayer Structure Calculations. *Biophys. J.* **75,** 734–744 (1998).

98. Kharaziha, P., Ceder, S., Li, Q. & Panaretakis, T. Tumor cell-derived exosomes: A message in a bottle. *BBA - Reviews on Cancer* **1826,** 103–111 (2012).

99. Yamada, T., Inoshima, Y., Matsuda, T. & Ishiguro, N. Comparison of Methods for Isolating Exosomes from Bovine Milk. *J. Vet. Med. Sci.* **74,** 1523–1525 (2012).

100. Kawaguchi, S. *et al.* Aqueous solution properties of oligo- and poly(ethylene oxide) by static light scattering and intrinsic viscosity. *Polymer* **38,** 7–7 (1997).

101. Bevers, E. M., Comfurius, P. & Zwaal, R. F. Platelet procoagulant activity: physiological significance and mechanisms of exposure. *Blood Rev.* **5,** 146–154 (1991).

102. Jobe, S. M. *et al.* Critical role for the mitochondrial permeability transition pore and cyclophilin D in platelet activation and thrombosis. *Blood* **111,** 1257–1265 (2008).

103. Suzuki, J., Umeda, M., Sims, P. J. & Nagata, S. Calcium-dependent phospholipid scrambling by TMEM16F. *Nature* **468,** 834–838 (2010).

104. Bevers, E. M., Comfurius, P. & Zwaal, R. F. Changes in membrane phospholipid distribution during platelet activation. *Biochim. Biophys. Acta* **736,** 57–66 (1983).

105. Jones, M. E., Lentz, B. R., Dombrose, F. A. & Sandberg, H. Comparison of the abilities of synthetic and platelet-derived membranes to enhance thrombin formation. *Throm. Res.* **39,** 711–724 (1985).

106. Rosing, J., Tans, G., Govers-Riemslag, J. W. P., Zwaal, R. F. A. & Hemker, H. C. The role of phospholipids and factor Va in the prothrombinase complex. *J. Biol. Chem.* **255,** 274–283 (1980).

107. Aderem, A. The MARCKS brothers: a family of protein kinase C substrates. *Cell* **71,** 713–716 (1992).

108. Kim, J., Shishido, T., Jiang, X., Aderem, A. & McLaughlin, S. Phosphorylation, high ionic strength, and calmodulin reverse the binding of MARCKS to phospholipid vesicles. *J. Biol. Chem.* **269,** 28214–28219 (1994).

109. Rosen, A., Keenan, K. F., Thelen, M., Nairn, A. C. & Aderem, A. Activation of protein kinase C results in the displacement of its myristoylated, alanine-rich substrate from punctate structures in macrophage filopodia. *J. Exp. Med.* **172,** 1211–1215 (1990).

110. McLaughlin, S. & Aderem, A. The myristoyl-electrostatic switch: a modulator of reversible protein-membrane interactions. *Trends Biochem. Sci.* **20,** 272–276 (1995).

111. McLaughlin, S., Wang, J., Gambhir, A. & Murray, D. PIP 2and Proteins: Interactions, Organization, and Information Flow. *Annu. Rev. Biophys. Biomol. Struct.* **31,** 151–175 (2002).

112. Hartwig, J. H. *et al.* MARCKS is an actin filament crosslinking protein regulated by protein kinase C and calcium-calmodulin. *Nature* **356,** 618–622 (1992).

113. Stumpo, D. J., Bock, C. B., Tuttle, J. S. & Blackshear, P. J. MARCKS deficiency in mice leads to abnormal brain development and perinatal death. *Proc. Natl. Acad. Sci. U.S.A.* **92,** 944–948 (1995).

114. Song, J. C., Hrnjez, B. J., Farokhzad, O. C. & Matthews, J. B. PKC-epsilon regulates basolateral endocytosis in human T84 intestinal epithelia: role of F-actin and MARCKS. *Am. J. Physiol.* **277,** C1239–49 (1999).

115. Blackshear, P. J. The MARCKS family of cellular protein kinase C substrates. *J. Biol. Chem.* **268,** 1501–1504 (1993).

116. Qin, Z. & Cafiso, D. S. Membrane structure of protein kinase C and calmodulin binding domain of myristoylated alanine rich C kinase substrate determined by site-directed spin labeling. *Biochemistry* **35,** 2917–2925 (1996).

117. Morton, L. A., Tamura, R., de Jesus, A. J., Espinoza, A. & Yin, H. Biophysical investigations with MARCKS-ED: dissecting the molecular mechanism of its curvature sensing behaviors. *Biochim. Biophys. Acta* **1838,** 3137–3144 (2014).

118. Yan, L. *et al.* Curvature sensing MARCKS-ED peptides bind to membranes in a stereo-independent manner. *J. Pept. Sci.* **21,** 577–585 (2015).

119. Werle, M. & Bernkop-Schnürch, A. Strategies to improve plasma half life time of peptide and protein drugs. *Amino Acids* **30,** 351–367 (2006).

120. Rauch, M. E., Ferguson, C. G., Prestwich, G. D. & Cafiso, D. S. Myristoylated alanine-rich C kinase substrate (MARCKS) sequesters spin-labeled phosphatidylinositol 4,5-bisphosphate in lipid bilayers. *J. Biol. Chem.* **277,** 14068–14076 (2002).

121. Ellena, J. F. *et al.* Membrane position of a basic aromatic peptide that sequesters phosphatidylinositol 4,5 bisphosphate determined by site-directed spin labeling and high-resolution NMR. *Biophys. J.* **87,** 3221–3233 (2004).

122. Alberio, L., Safa, O., Clemetson, K. J., Esmon, C. T. & Dale, G. L. Surface expression and functional characterization of alpha-granule factor V in human platelets: effects of ionophore A23187, thrombin, collagen, and convulxin. *Blood* **95,** 1694–1702 (2000).

123. Dale, G. L. Coated-platelets: an emerging component of the procoagulant response. *J. Thromb. Haemost.* **3,** 2185–2192 (2005).

124. Owens, A. P. & Mackman, N. Microparticles in hemostasis and thrombosis. *Circ. Res.* **108,** 1284–1297 (2011).

125. Shi, J. *et al.* Lactadherin detects early phosphatidylserine exposure on immortalized leukemia cells undergoing programmed cell death. *Cytometry* **69A,** 1193–1201 (2006).

126. Onasoga-Jarvis, A. A. *et al.* The effect of factor VIII deficiencies and replacement and bypass therapies on thrombus formation under venous flow conditions in microfluidic and computational models. *PLoS ONE* **8,** e78732 (2013).

127. Stalker, T. J. *et al.* Hierarchical organization in the hemostatic response and its relationship to the platelet-signaling network. *Blood* **121,** 1875–1885 (2013).

128. Falati, S., Gross, P., Merrill-Skoloff, G., Furie, B. C. & Furie, B. Real-time in vivo imaging of platelets, tissue factor and fibrin during arterial thrombus formation in the mouse. *Nat. Med.* **8,** 1175–1180 (2002).

129. Jobe, S. M. *et al.* Role of FcRgamma and factor XIIIA in coated platelet formation. *Blood* **106,** 4146–4151 (2005).

130. Mazepa, M., Hoffman, M. & Monroe, D. Superactivated platelets: thrombus regulators, thrombin generators, and potential clinical targets. *Arterioscler. Thromb. Vasc. Biol.* **33,** 1747–1752 (2013).

131. Bevers, E. M., Comfurius, P., van Rijn, J. L. M. L., Hemker, H. C. & Zwaal, R. F. A. Generation of prothrombin-converting activity and the exposure of phosphatidylserine at the outer surface of platelets. *Eur. J. Biochem.* **122,** 429–436 (1982).

132. Li, Y., Martin, L. D., Spizz, G. & Adler, K. B. MARCKS protein is a key molecule regulating mucin secretion by human airway epithelial cells in vitro. *J. Biol. Chem.* **276,** 40982–40990 (2001).

133. Singer, M. *et al.* A MARCKS-related peptide blocks mucus hypersecretion in a mouse model of asthma. *Nat. Med.* **10,** 193–196 (2004).

134. Chen, C. H. *et al.* A peptide that inhibits function of Myristoylated Alanine-Rich C Kinase Substrate (MARCKS) reduces lung cancer metastasis. *Oncogene* **33,** 3696–3706 (2014).

135. Lee, S. M., Suk, K. & Lee, W. H. Myristoylated alanine-rich C kinase substrate (MARCKS) regulates the expression of proinflammatory cytokines in macrophages through activation of p38/JNK MAPK and NF-κB. *Cell. Immunol.* **296,** 115–121 (2015).

136. Elzagallaai, A., Rosé, S. D., Brandan, N. C. & Trifaró, J. M. Myristoylated alanine-rich C kinase substrate phosphorylation is involved in thrombin-induced serotonin release from platelets. *Brit. J. Haematol.* **112,** 593–602 (2001).

137. Elzagallaai, A., Rosé, S. D. & Trifaró, J. M. Platelet secretion induced by phorbol esters stimulation is mediated through phosphorylation of MARCKS: a MARCKS-derived peptide blocks MARCKS phosphorylation and serotonin release without affecting pleckstrin phosphorylation. *Blood* **95,** 894–902 (2000).

138. Chu, A. J., Lin, S. H. & Piasentin, E. Possible role of Marcks in the cellular modulation of monocytic tissue factor-initiated hypercoagulation. *Brit. J. Haematol.* **118,** 569–576 (2002).

139. Uhlén, M. *et al.* Tissue-based map of the human proteome. *Science* **347,** 1260419 (2015).

140. Scott, J. L., Musselman, C. A., Adu-Gyamfi, E., Kutateladze, T. G. & Stahelin, R.

V. Emerging methodologies to investigate lipid-protein interactions. *Integr. Biol. (Camb)* **4,** 247–258 (2012).

141. Andree, H. A. *et al.* Clustering of lipid-bound annexin V may explain its anticoagulant effect. *J. Biol. Chem.* **267,** 17907–17912 (1992).

142. Thiagarajan, P. & Benedict, C. R. Inhibition of arterial thrombosis by recombinant annexin V in a rabbit carotid artery injury model. *Circulation* **96,** 2339–2347 (1997).

143. Shi, J. & Gilbert, G. E. Lactadherin inhibits enzyme complexes of blood coagulation by competing for phospholipid-binding sites. *Blood* **101,** 2628–2636 (2003).

144. Shi, J., Pipe, S. W., Rasmussen, J. T., Heegaard, C. W. & Gilbert, G. E. Lactadherin blocks thrombosis and hemostasis in vivo: correlation with platelet phosphatidylserine exposure. *J. Thromb. Haemost.* **6,** 1167–1174 (2008).

145. Chong, P., Sia, C., Tripet, B., James, O. & Klein, M. Comparative immunological properties of enantiomeric peptides. *Lett. Pept. Sci.* **3,** 99–106 (1996).

146. Jenssen, H. & Aspmo, S. I. Serum stability of peptides. *Methods Mol. Biol.* **494,** 177–186 (2008).

147. Morton, L. A., Saludes, J. P. & Yin, H. Constant pressure-controlled extrusion method for the preparation of nano-sized lipid vesicles. *J. Vis. Exp.* **64,** e4151 (2012).

148. Stahelin, R. V. Surface plasmon resonance: a useful technique for cell biologists to characterize biomolecular interactions. *Mol. Biol. Cell* **24,** 883–886 (2013).

149. Myszka, D. G. Improving biosensor analysis. *J. Mol. Recognit.* **12,** 279–284 (1999).

150. Leo, L., Di Paola, J., Judd, B. A., Koretzky, G. A. & Lentz, S. R. Role of the adapter protein SLP-76 in GPVI-dependent platelet procoagulant responses to collagen. *Blood* **100,** 2839–2844 (2002).

151. Neeves, K. B., Illing, D. A. R. & Diamond, S. L. Thrombin flux and wall shear rate regulate fibrin fiber deposition state during polymerization under flow. *Biophys. J.* **98,** 1344–1352 (2010).

152. Sammond, D. W., Kastelowitz, N., Himmel, M. E. & Yin, H. Comparing Residue Clusters from Thermophilic and Mesophilic Enzymes Reveals Adaptive Mechanisms. *PLoS ONE* **11**, e0145848 (2016).

Appendix A

Supporting Information - Changes in lipid density induce membrane curvature

This appendix contains supporting information that has been published as de Jesus, A. J.*, Kastelowitz, N*. & Yin, H. Changes in lipid density induce membrane curvature. *RSC Adv.* **3**, 13622 (2013). * These authors contributed equally to this work.

A.1 Supplementary figures and tables

System 1			
POPS Concentration	**No. of POPS per leaflet**	**No. of waters**	**Total No. of atoms**
0% PS	0	28877	153889
5% PS	13	28842	153600
10% PS	25	28715	153051
15% PS	38	28549	152369
20% PS	50	28649	152501

System 2			
POPS Concentration	**No. of POPS per leaflet**	**No. of waters**	**Total No. of atoms**
0% PS	0	28961	154141
5% PS	13	28848	153618
10% PS	25	28651	152859
15% PS	38	28550	152372
20% PS	50	28394	151736

Supplementary Table A.1. Characteristics of the simulated membrane systems. The POPS concentration refers to the percentage of POPS molecules in each individual simulation.

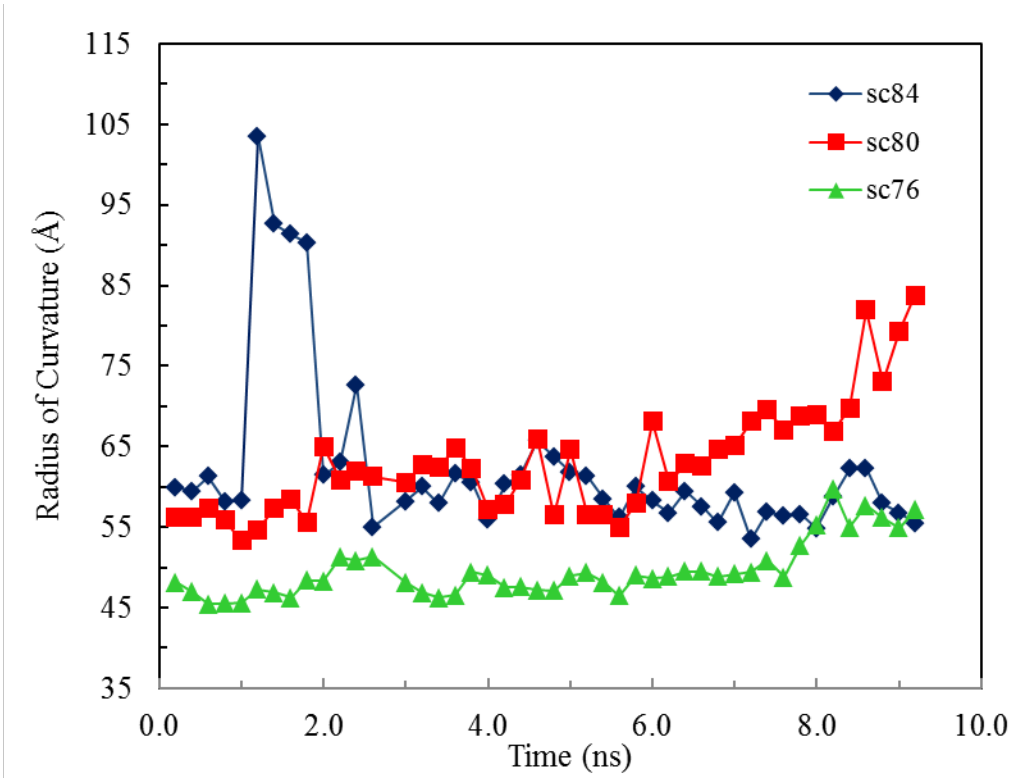

Supplementary Figure A.1. Time series of the radius of curvature for the simulation systems with 15% PS.

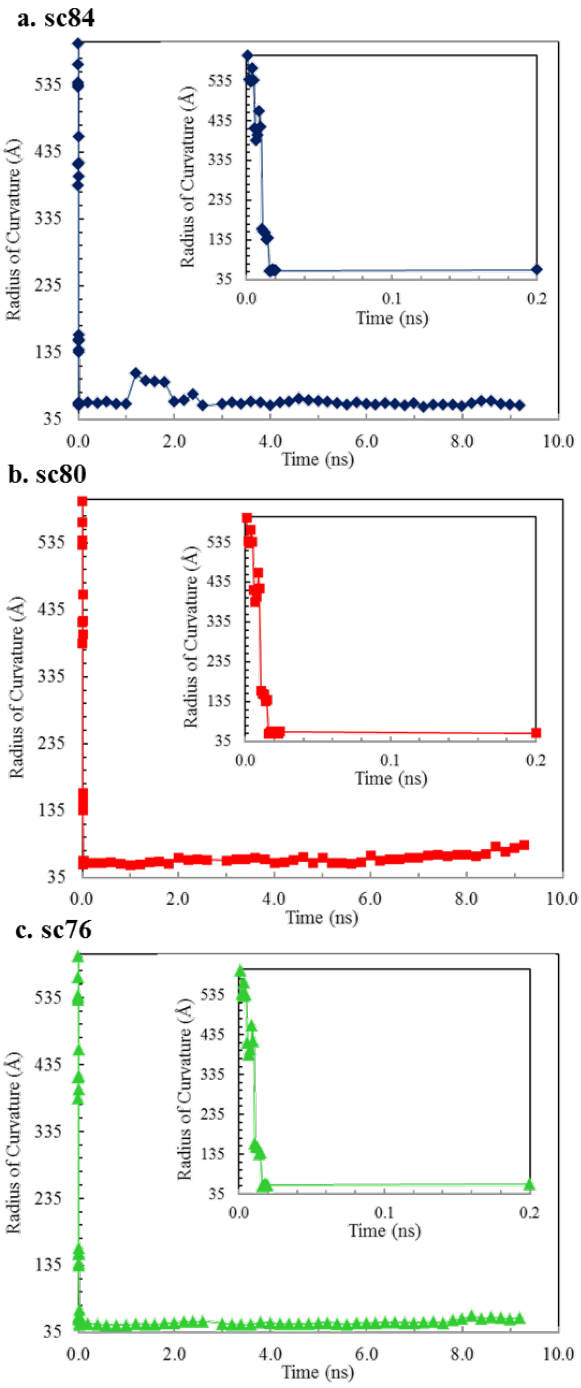

Supplementary Figure A.2. Time series of the radius of curvature from the beginning of bilayer compression for the simulation systems with 15% PS. The insets show the radius of curvature during the early stages of compression.

A.2 Supplementary video legends

A.1

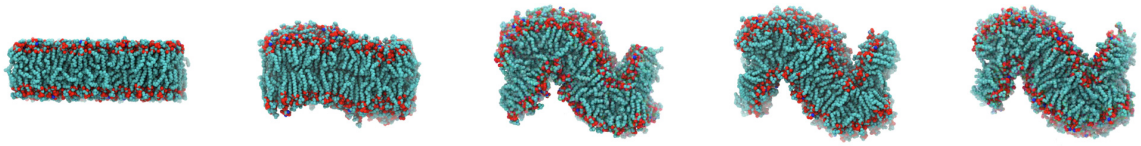

A.2

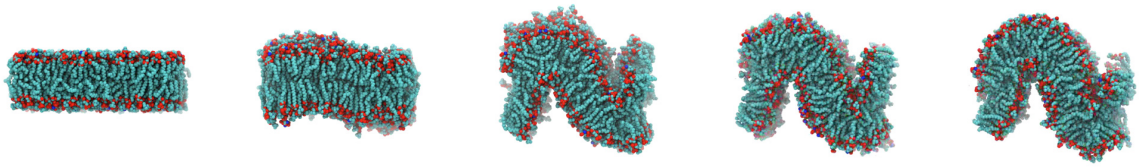

A.3

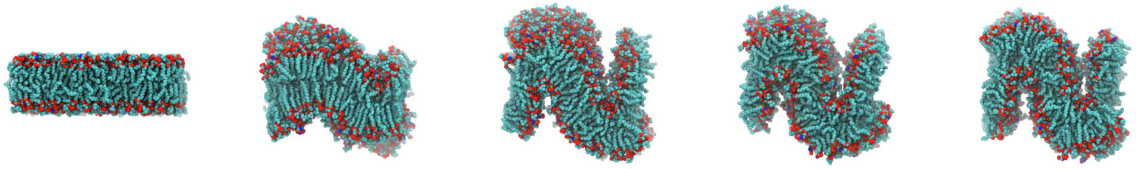

Supplementary Video Legends A.1-3. Movies showing the compression of the 15% PS bilayer systems. The movies show approximately 12 ns of simulation: 2 ns of dynamics of the flat membrane, ~45 to 65 ps of compression, and 10 ns of dynamics of the curved bilayers. In the portions showing the molecular dynamics of the flat and curved bilayers, the time gap between each movie frame is 20 times longer than that of the compression portion. Video A.1 corresponds to the sc84 system, A.2 to sc80, and A.3 to sc76.

Appendix B

Supporting Information - Peptides derived from MARCKS block coagulation protein complex assembly on phosphatidylserine and inhibit fibrin formation

B.1 Supplementary figures

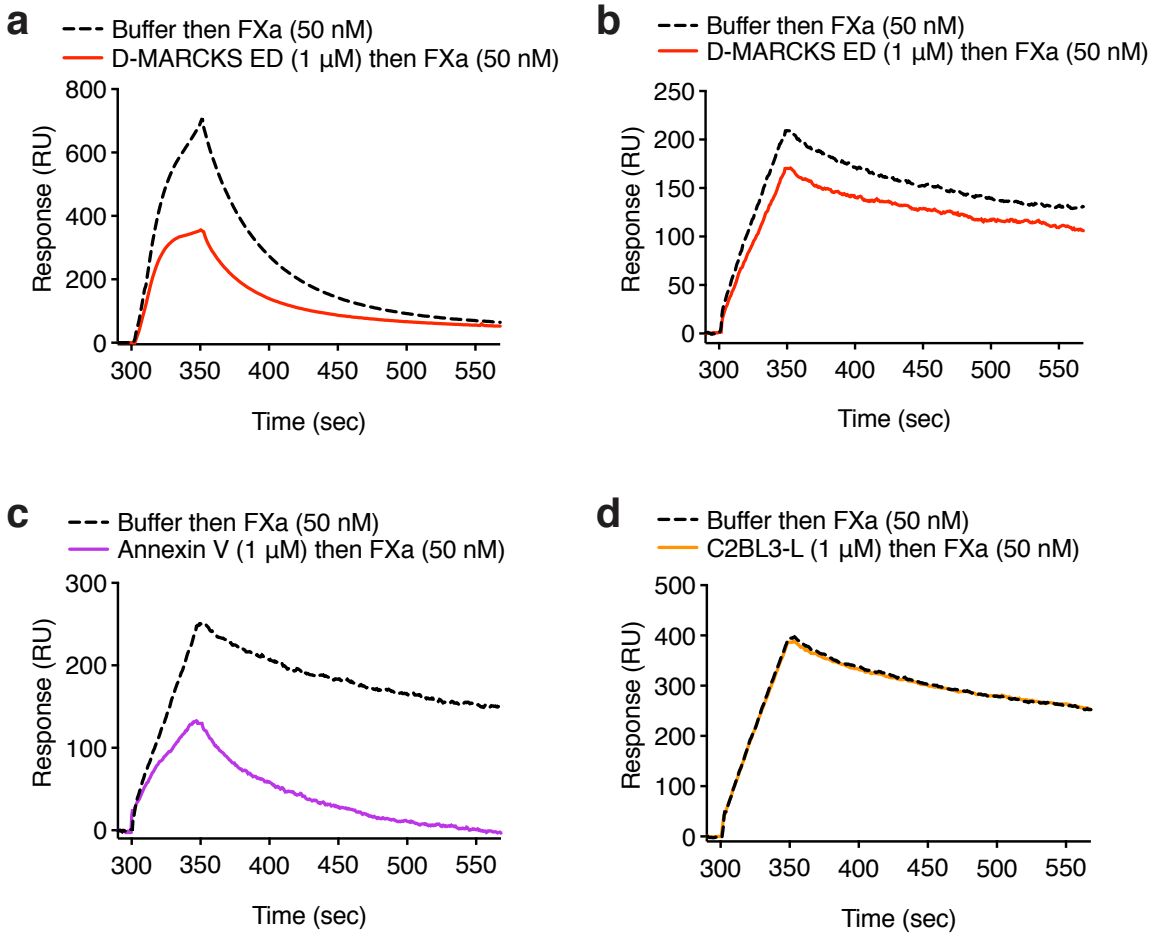

Supplementary Figure B.1. SPR sensograms of FXa binding response corrected by double referencing. In each panel, the dashed black lines show an injection of 50 nM FXa at t = 300 sec that was preceded by an injection of running buffer at t = 30 sec. Following complete dissociation of FXa from the membrane surface, the solid colored lines show an injection of 50 nM FXa at t = 300 sec that was preceded by an injection of 1 μM D-MARCKS (**a**,**b**), annexin V (**c**), or C2BL3-L (**d**) at t = 30 sec (*n* = 3). Sensogram in (**a**) was obtained with a Biacore 3000 instrument. Sensograms in (**b**-**d**) were obtained with a BiOptix 404pi instrument.

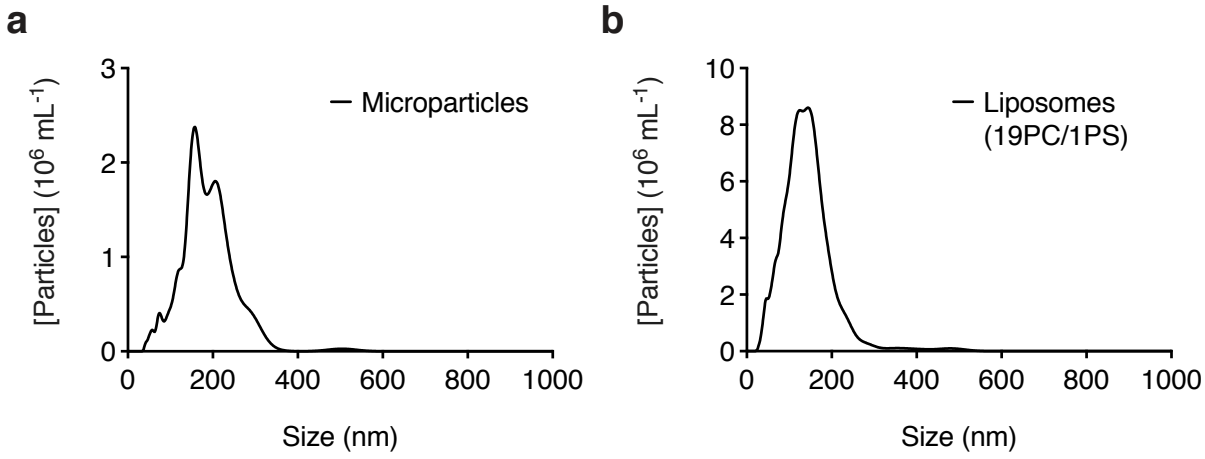

Supplementary Figure B.2. Representative size distributions of prothrombinase assay biologic microparticles and synthetic liposomes characterized by nanoparticle tracking analysis. (**a**) Microparticles isolated from MDA-MB-231 human breast cancer cells. (**b**) Liposomes composed of POPC/POPS at a 19/1 ratio extruded through 100 nm pore size polycarbonate membranes.

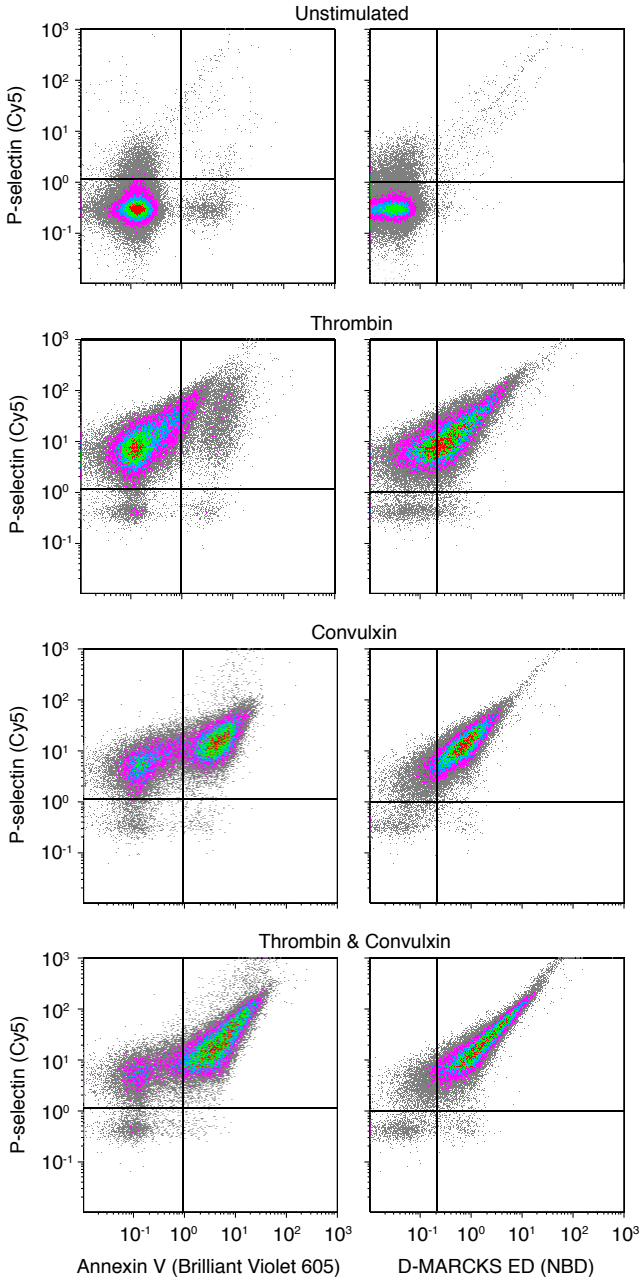

Supplementary Figure B.3. Representative flow cytometry scatter plots comparing platelet annexin V (Brilliant Violet 605) or D-MARCKS ED (NBD) fluorescence intensity to P-selection (Cy5) fluorescence intensity when the platelets were left unstimulated or stimulated with thrombin, convulxin, or thrombin and convulxin (*n* = 6).

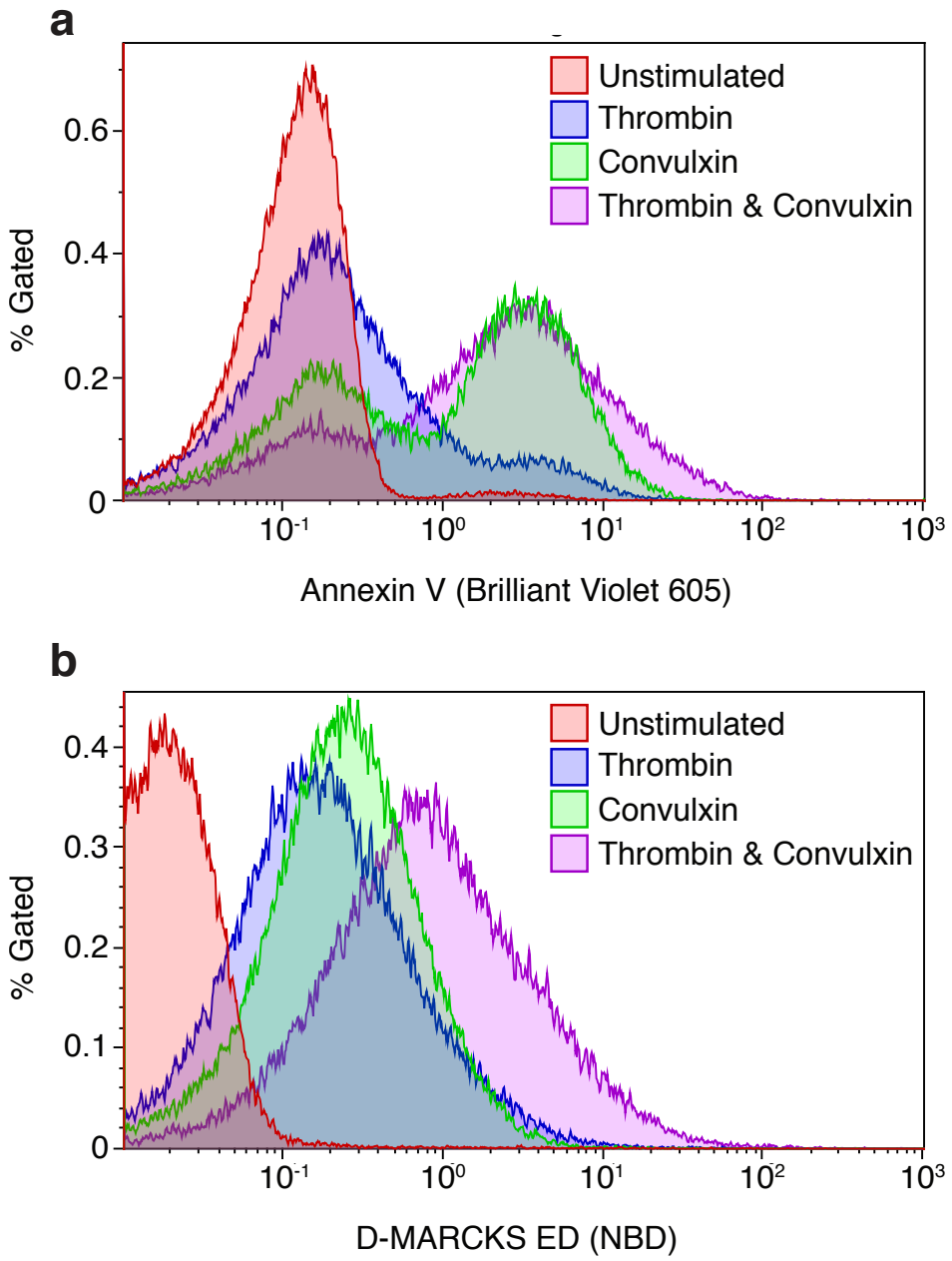

Supplementary Figure B.4. Flow cytometry histograms of platelet (**a**) annexin V (Brilliant Violet 605) and (**b**) D-MARCKS ED (NBD) fluorescence intensity when platelets were left unstimulated (red) or stimulated with thrombin (blue), convulxin (green), or thrombin and convulxin (purple) (n = 6).

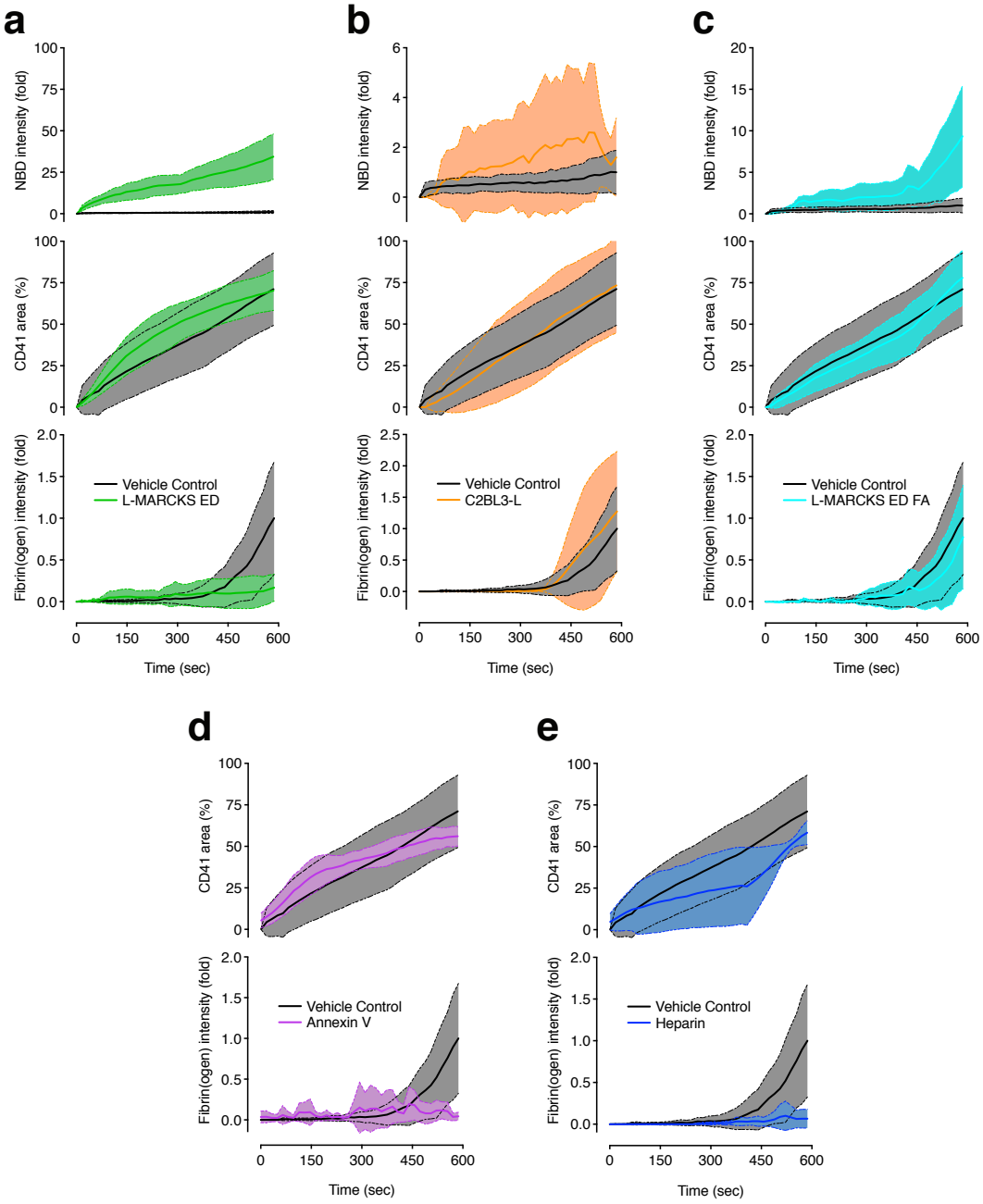

Supplementary Figure B.5. Time course comparing whole blood microfluidic flow assay peptide NBD fluorescence intensity (**a**-**c**), platelet surface area coverage, and fibrin(ogen) intensity for vehicle control to treatment with 1 μM L-MARCKS ED (**a**), C2BL3-L (**b**), L-MARCKS ED FA mutant (**c**), annexin V (**d**), or 15 USP ml^{-1} heparin (**e**) (*n* = 6, mean ± s.d.).

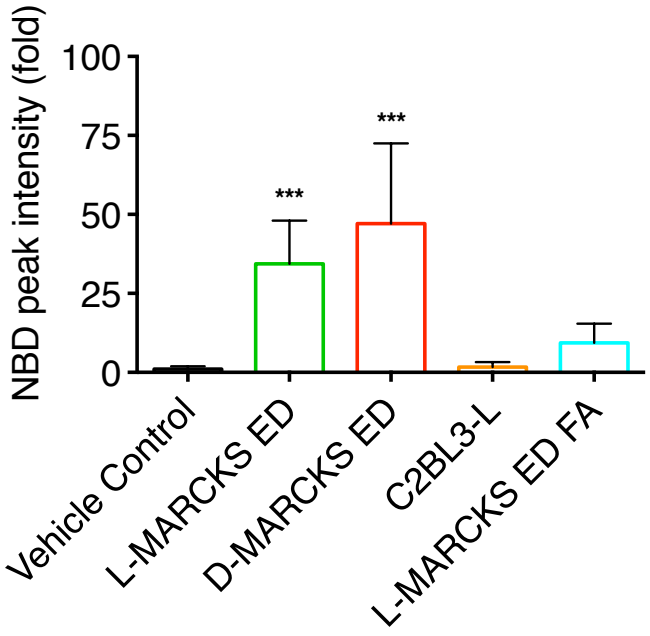

Supplementary Figure B.6. Final peptide NBD fluorescence intensity values for each treatment in the microfluidic flow assay (n = 6, mean ± s.d.). *** $P < 0.001$ compared to vehicle control by one-way analysis of variance (ANOVA) followed by Dunnet's *post hoc* test.

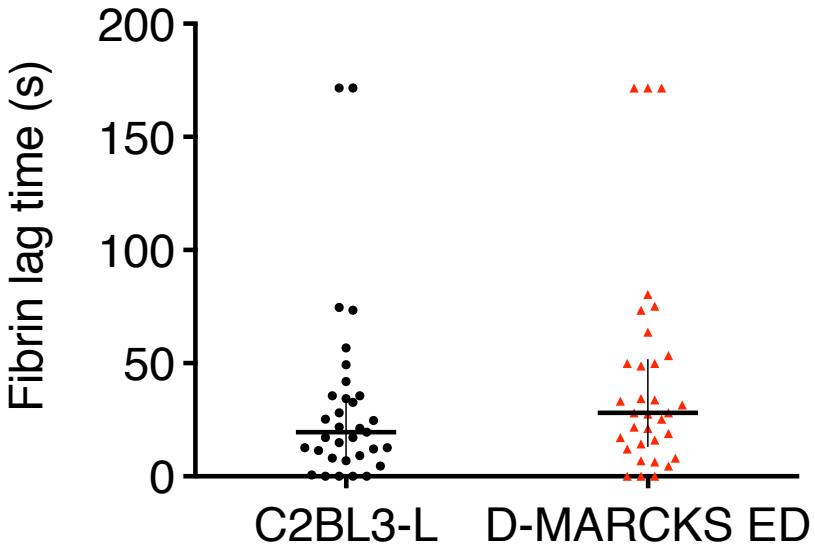

Supplementary Figure B.7. Fibrin lag time, defined as time to 20 μm^2 fibrin area, in the murine intravital laser-induced microvascular injury model when treated with 5 mg kg^{-1} negative control C2BL3-L or D-MARCKS ED (*n* = 33 thrombi from 4 mice).

B.2 Supplementary video legends

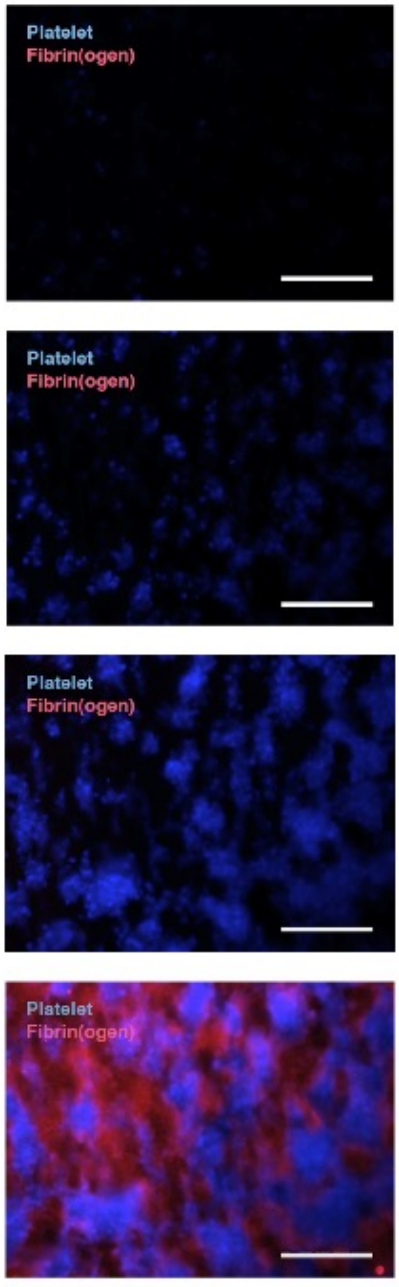

Supplementary Video Legend B.1. Representative video of platelet accumulation and fibrin formation in the whole blood microfluidic flow assay following addition of vehicle control. Platelets are labeled with a Pacific Blue anti-human CD41 antibody and shown in blue. Fibrin(ogen) is labeled with Alexa Fluor 647 and shown in red. Video shows a 10-minute time course. Scale bar, 50 μm. (See main Fig. 4.3).

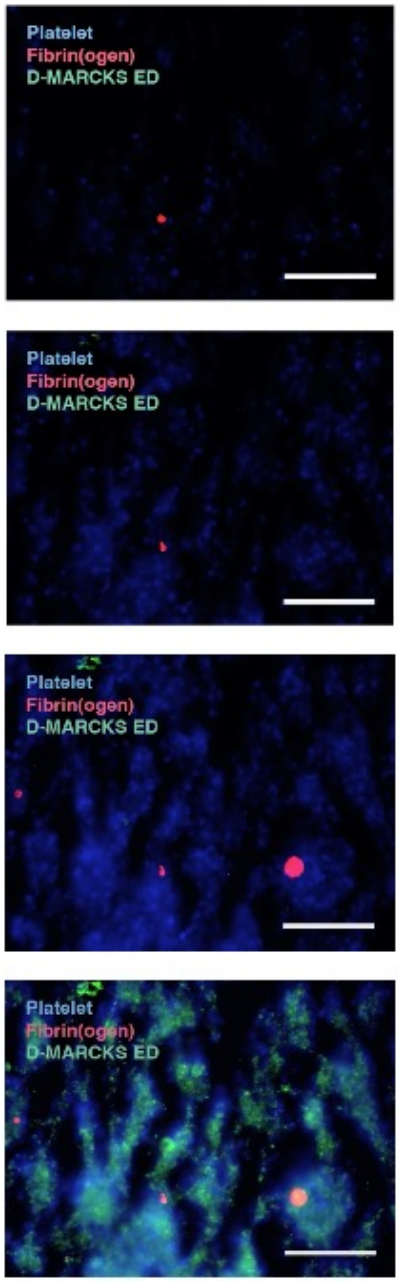

Supplementary Video Legend B.2. Representative video of platelet accumulation, fibrin formation, and peptide labeling in the whole blood microfluidic flow assay following addition of D-MARCKS ED peptide. Platelets are labeled with a Pacific Blue anti-human CD41 antibody and shown in blue. Fibrin(ogen) is labeled with Alexa Fluor 647 and shown in red. D-MARCKS ED is labeled with NBD and shown in green. Video shows a 10-minute time course. Scale bar, 50 μm. (See main Fig. 4.3).

Appendix C

Comparing residue clusters from thermophilic and mesophilic enzymes reveals adaptive mechanisms

This appendix contains text and figures that have been published as Sammond, D. W., Kastelowitz, N., Himmel, M. E. & Yin, H. Comparing Residue Clusters from Thermophilic and Mesophilic Enzymes Reveals Adaptive Mechanisms. *PLoS ONE* **11**, e0145848 (2016).

C.1 Abstract

Understanding how proteins adapt to function at high temperatures is important for deciphering the energetics that dictate protein stability and folding. While multiple principles important for thermostability have been identified, we lack a unified understanding of how internal protein structural and chemical environment determine qualitative or quantitative impact of evolutionary mutations. In this work we compare equivalent clusters of spatially neighboring residues between paired thermophilic and mesophilic homologues to evaluate adaptations under the selective pressure of high temperature. We find the residue clusters in thermophilic enzymes generally display

improved atomic packing compared to mesophilic enzymes, in agreement with previous research. Unlike residue clusters from mesophilic enzymes, however, thermophilic residue clusters do not have significant cavities. In addition, anchor residues found in many clusters are highly conserved with respect to atomic packing between both thermophilic and mesophilic enzymes. Thus the improvements in atomic packing observed in thermophilic homologues are not derived from these anchor residues but from neighboring positions, which may serve to expand optimized protein core regions.

C.2 Contributions

This research was done in collaboration with scientists at the National Renewable Energy Laboratory in Golden, Colorado. My contributions were principally identification of enzyme families, using computational structural bioinformatics methods to compare structures and residue clusters, and analysis of the results. Our results demonstrated that thermophilic proteins show improved residue packing around conserved anchor residues when compared to their mesophilic counterparts. This may explain the observed differences in stability and optimum activity temperatures of these proteins, and provide a targetable element for improving the thermostability of existing mesophilic enzymes that do not exist in thermophilic form. Pertinent figures relevant to these contributions are included below. Further results and discussion can be found in the published paper.[152]

C.3 Supplementary figures and tables

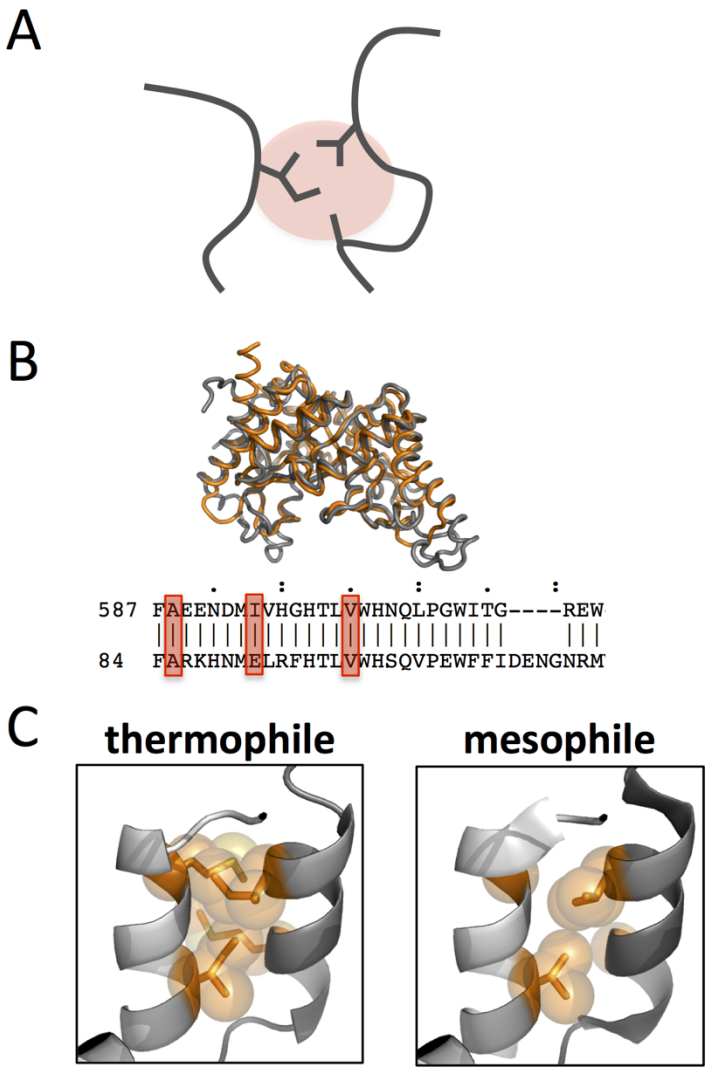

Supplementary Figure C.1. Identifying equivalent clusters in homologous proteins allows for direct comparison of local environments. (A) A cartoon depiction of cluster of adjacent residues is shown (red circle). (B) Structural alignment of paired enzymes is shown, with PDB 1vbr in orange and 2uwf in gray. The structurally aligned residues for the paired enzymes are shown beneath. (C) Differences in atomic packing are depicted with alternate sequences shown in stick and sphere representation on PDB 2wva.

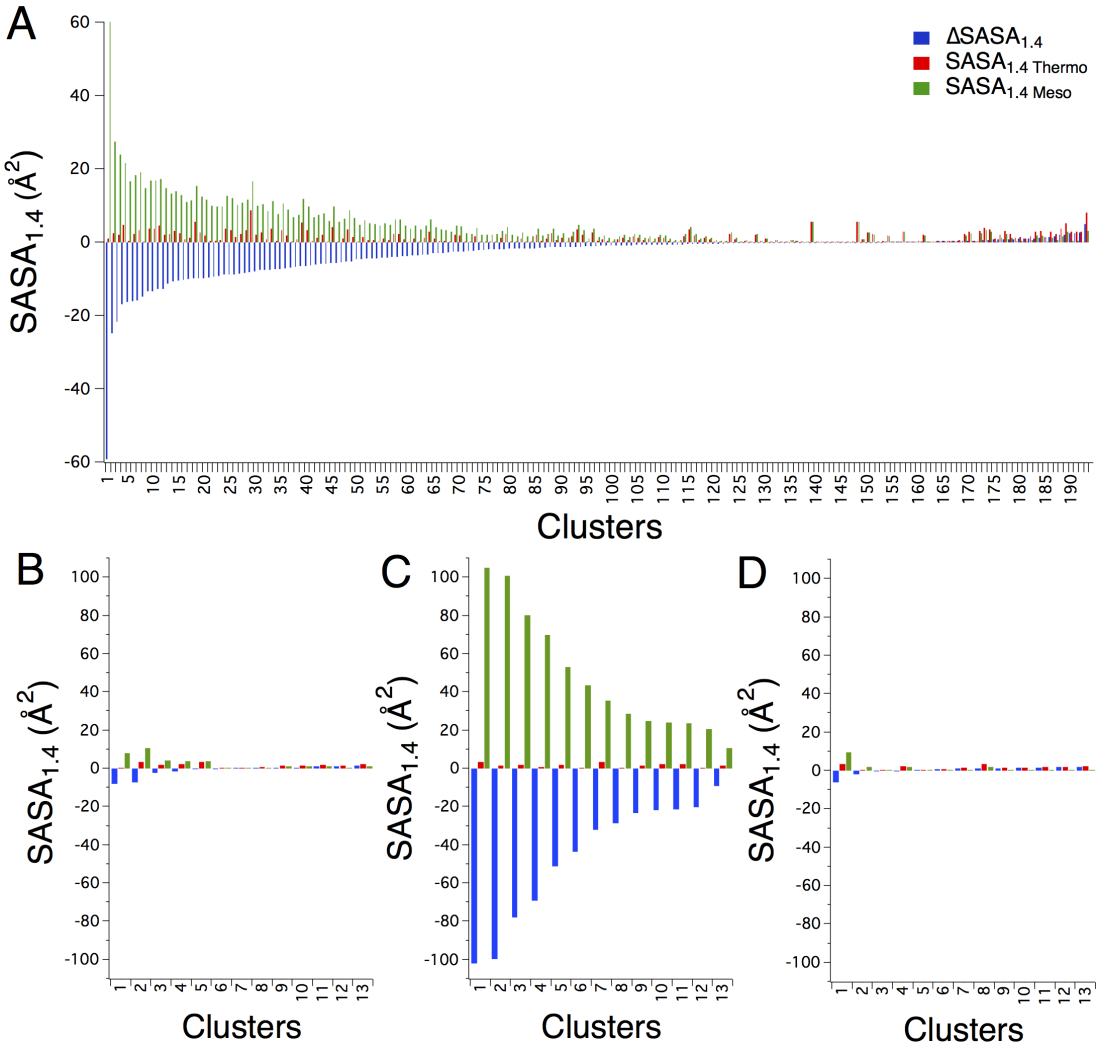

Supplementary Figure C.2. Thermophilic enzyme clusters display closer atomic packing compared to mesophilic enzyme clusters for most enzyme pairs evaluated. (A) $SASA_{1.4}$ values for clusters from the representative thermophilic-mesophilic structure pairs are shown, with thermophilic clusters shown in red, mesophilic clusters in green and the difference, $\Delta SASA_{1.4}$, in blue. Values are sorted by $\Delta SASA_{1.4}$. (B) $SASA_{1.4}$ values are shown comparing clusters from the thermophilic (PDB 1a5z) and mesophilic (PDB 6ldh) lactate dehydrogenase enzymes, which have a difference in optimum activity temperature of 30°C. (C) the thermophilic (PDB 1a5z) and mesophilic (PDB 5ldh) lactate dehydrogenase enzymes, with a difference in optimum activity temperature of 48°C, (D) and the thermophilic (PDB 1a5z) and psychrophilic (PDB 1ldh) lactate dehydrogenase enzymes, with a difference in optimum activity temperature of 70°C.

Representative Structures—193 clusters		
	Count	**Percentage**
$\Delta SASA_{1.4} < 0$	145	75%
$\Delta SASA_{1.4} < 1$	64	33%
$\Delta SASA_{1.4} < 2$	1	1%
	Max	**Average**
$SASA_{Thermo}$	8.7	1.5
$SASA_{Meso}$	60.2	4.8
All Structures—501 clusters		
	Count	**Percentage**
$\Delta SASA_{1.4} < 0$	388	77%
$\Delta SASA_{1.4} \leq -3$	227	45%
$\Delta SASA_{1.4} \geq 3$	6	1%
ΔContact Number ≤ 0	346	69%
	Max	**Average**
$SASA_{Thermo}$	8.7	1.6
$SASA_{Meso}$	100.9	8.4
% Sequence Identity		
	Median	**Average**
$\Delta SASA_{1.4} \leq -3$	50	49
$-3 < \Delta SASA1.4 < 3$	67	65
$\Delta SASA_{1.4} \geq 3$	44	51

Supplementary Table C.1. Comparing void volumes, as determined by $\Delta SASA_{1.4}$ and residue contact number, and percent sequence identity for paired clusters.